University of Sussex

Applications of Kelvin Probe Force Microscopy in the characterization of 2D materials and their composites

Giuseppe Fratta

Submitted for the degree of Doctor of Philosophy in Physics

July 2019

Declaration

I hereby declare that this thesis has not been and will not be submitted in whole or in part to another University for the award of any other degree.

Signature

Giuseppe Fratta

Acknowledgements

Firstly, I would like to thank Prof. Dalton for selecting me for this project, guiding me with his knowledge and confidence in a field that was in many cases new and challenging for me. The opportunity he gave me to work with one of the best AFM in the market was an advantage that I never took for granted and I hope I deserved it.

I also have to thank Dr. Large and Dr. Ogilvie for the invaluable contribution they gave me during the revision process of this thesis. The thoroughness shown by Matt during the review process is something that I will always be very thankful for, greatly improving both the writing and the scientific aspects of this thesis. As for Sean, I also want to give him a personal thank you for always showing me the bright side when, particularly during the first months, the challenge sometimes seemed insurmountable, I wish you the best for your next duties as a researcher/teacher and as a father.

A very big thank you must also go to Manuela, for being a very good friend and colleague. Her contribution in this thesis is not only scientific for her samples and ideas that contributes to chapter 6, but also for giving me constantly support from the moment I wrote the first line to the very end, and I hope I have gave her the same level of support.

Another important help has come from Dr. Tripathi, who has brought, from the moment he arrived, new energy and ideas for novel KPFM applications. Now the machine is in your hands and I am sure you will make good use of it.

In general, all the scientific work presented in this thesis has been influenced by the discussions and collaborations with all the remaining people in the group, so I want to thank Alice, Aline, Peter, Marcus, Annie, Frank, Abdullah.

Being a member of a European project means also that I had plenty of other colleagues with many other specializations to contact in need of help, so I would like to thank in particular Seb, Dominik, Emin, Lorenzo, Ruben, Yuman and Daniel.

A more general thank you, of course, goes to all the Professors of the network for the opportunity of participating in many useful conferences and seminars in these years.

Finally, a big thank you for all the friends and members of my family that supported me in these years that I spent far from them, in particular my father, my girlfriend and my best friend. I have been very lucky, and I will try my best to show that it was worth it.

Table of Contents

List of Abbreviations v

Abstract 1

Chapter 1 Introduction to Kelvin Probe Force Microscopy 2

1.1 Introduction and historical development of KPFM 3
1.2 Practical considerations to improve KPFM imaging and limits of the technique. 15

Chapter 2 Basics of other characterization and deposition techniques, and introduction to graphene 20

2.1 Raman spectroscopy basics 21
2.2 SEM basics 23
2.3 Deposition techniques 25
2.3.1 Drop casting 26
2.3.2 Spin-coating 26
2.3.3 Langmuir Techniques 27
2.4 Quality of deposition depending on the deposition technique 30
2.5 Introduction to Graphene 33

Chapter 3 State of the art of the use of the KPFM for characterization of 2D material . 38

3.1 Overview of the use of KPFM for the characterization of 2D materials 38
3.2 Example of a CPD/height studies of liquid exfoliated TMDs 44

Chapter 4 Laser Based Texturing of Graphene to locally tune Electrical Potential and Surface Chemistry 50

4.1 Introduction 50
4.2 Morphology and local surface potential of blisters and graphene nanobubbles ... 55
4.3 The influence of laser power density 61
4.4 The role of trapped molecules between graphene-silica interface and functionalization of graphene 64
4.5 Conclusions 69

Chapter 5 KPFM measurements of the AgNW–graphene interface for transparent electrode applications 70

5.1 Introduction 70

5.2 Nanomaterials and AgNWs use in transparent electrodes technology 72
5.3 Silver Nanowires synthesis, deposition and characterization 78
5.4 KPFM and Raman characterization of the AgNW/Graphene system 83
5.5 Conclusions 90

Chapter 6 KPFM characterization of graphene – latex composites 92

6.1 Introduction 92
6.2 Preliminary test on GO and rGO to test KPFM sensitivity 95
6.3 Composite analyses and discussion 97
6.4 KPFM characterization of the final composite 103
6.5 Conclusions 110

Summary and Conclusions 111

Bibliography 113

List of Abbreviations

1LG : 1 Layer Graphene

2LG : 2 Layer Graphene

AFM : Atomic Force Microscopy

AgNW : Silver NanoWire

CNT : Carbon NanoTube

CPD : Contact Potential Difference

CVD : Chemical Vapour Deposition

KPFM : Kelvin Probe Force Microscopy

GO : Graphene Oxide

HOPG : Highly Oriented Pyrolytic Graphene

IPA : Isopropyl Alcohol

ITO : Indium Tin Oxide

LS : Langmuir-Schaefer technique

NMP : N-Methylpyrrolidone

PL : Polymer Latex

PVP : PolyVinylPyrrolidone

rGO : reduced Graphene Oxide

SEM : Scanning Electron Microscope

TMD : Transition Metal Dichalcogenides

UHV : Ultra High Vacuum

XPS : X-Ray Photoelectron Spectroscopy

Abstract

Kelvin Probe Force Microscopy (KPFM), since its relatively recent introduction in 1991, has become a widely used technique to assess surface charge distribution and work function of metal/semiconductor interfaces in electronic devices at the nanoscale.

Today, this characterization technique is employed in many nanotechnology-related applications, with 2D layered material being a notable example due to the necessity of characterizing various electrical properties with high spatial resolution to better understand how these parameters scale or change relatively with synthesis, deposition and environment conditions.

In this thesis I will discuss the main applications of KPFM characterization that I have encountered during my three years of doctorate, showing its usefulness in various fields, its main limitations and some practical considerations about the best practices I developed to optimize sample preparation.

Regarding the study of fundamental electronic properties I will present my results on the correlation of work function of 2D materials like MoS_2 and their thickness (Chapter 3), and how laser induced 3D structures can locally tune the work function of the graphene basal plane for possible future localized functionalization (Chapter 4).

As an example of the use of KPFM characterization of 2D composites, I will present the analyses of a metal/graphene interface, more specifically the silver nanowire (AgNW)/graphene interface, selected as it represents a very promising type of hybrid for devices requiring highly conductive transparent electrodes (Chapter 5).

Finally, I will show how KPFM can be employed even in a macroscopic conductive 2D material/polymer composite to elucidate the structure or to verify the presence of the conductive elements inside the insulating polymeric matrix (Chapter 6).

At the start of this work, I will present a theory background on the origin and principles of the technique, its evolution and main limitations (Chapter 1) followed by a brief introduction of the main other characterization techniques employed and my personal consideration on the best deposition techniques (Chapter 2).

Chapter 1
Introduction to Kelvin Probe Force Microscopy

The goal of this thesis is to show how Kelvin Probe Force Microscopy (KPFM) represents a valuable tool to gain insight into the interactions between 2D nanomaterials and their environment in a variety of different conditions. To this day, most of the applications of this technique have been relegated to studies performed in highly controlled environments like clean rooms, which are very expensive and not accessible for many researchers.

This is rooted in some technical limitations of the technique, which I am going to introduce in this chapter, regarding its ability to detect quantitative data in standard conditions. While this limit still exists, I will show examples of how it is possible to gain a variety of useful qualitative information on the general phenomena affecting the target material in the desired substrate or surrounding matrix, all performed in standard room conditions.

Given the complexity of most of these studies, I would like to acknowledge from the start the contribution of colleagues that have helped me in areas I was not an expert of. In **Chapter 4**, **Dr. Tripathi**, and expert in Raman spectroscopy, was the one that discovered by accident the creation of graphene blisters under laser exposure, and while all the Raman data presented has been discussed and obtained after agreed planning, the data representation was made by him. In **Chapter 6, Dr. Meloni**, a chemist with expertise in latex synthesis, was the only responsible for the creation of all the samples that I have then analysed. All the information coming from techniques other than the AFM have been planned by her.

1.1 Introduction and historical development of KPFM

From its inception, the Atomic Force Microscopy (AFM) technique has been greatly expanded to probe an increasingly wide range of forces and tip/substrate interactions. Before the first description of the KPFM principles in 1991 by Nonnenmacher at al. [1], AFM electrical modes already existed for the detection of long range electrostatic forces, but not specifically for the direct detection of the contact potential difference (CPD). This quantity depends on generic properties of the sample like local temperature and oxide layer thickness or dopant presence when a semiconductor is probed, but, under the correct conditions it can be directly linked to the work function for conductive materials.

The work function of a metallic material is defined as the energy necessary to move one electron from the highest occupied energy level (called the Fermi energy level at Absolute Zero temperature) to the vacuum energy level, and it is directly linked to the conductivity via the carrier density properties of the material itself. The only other technique previously known for the precise measurement of work functions was the Kelvin method, requiring two macroscopic size conductors: one of known work function and the other being the one probed [2].

When they are put at a very close distance, an electric field is generated between them with a resulting electric tension value, known as the contact potential difference (CPD), following this equation:

$$V_{CPD} = \frac{1}{e}(\phi_2 - \phi_1) \tag{1.1}$$

Where ϕ_1 and ϕ_2 are the work function of the two materials, including the effect of any adsorbed layer or doping in real world applications.

To measure this voltage, a periodic oscillation of frequency ω is applied and the two plates are electrically connected, inducing an electric current of intensity:

$$i = V_{CPD}\ \omega \Delta C\ \cos \omega t \qquad (1.2)$$

With ΔC indicating the change in capacitance. Consequently an external bias is applied until the electric field is nullified and the resulting flowing electric current is zero.

In this technique, the measured value is averaged between the whole plate and it is not, therefore, able to probe local changes or effects at interfaces. While the geometries are far more complex and the field much harder to measure and isolate from atmospheric effects, the same principle is applied in KPFM between the probe material and the AFM tip, allowing the exploration of local changes at a very high lateral resolution.

In **fig. 1.1**, a schematic representation of how the energy levels change in the tip-sample interaction in a generic KPFM analysis is shown.

In **fig. 1.1 (a)** sample and tip share the same environment and they have the same vacuum energy level but different respective Fermi levels.

In **fig. 1.1 (b)** the sample and tip are grounded together and a flow of charge moves from the lower work function material to the one with the higher work function, creating an electric field of intensity V_{CPD}.

In **fig. 1.1 (c)** an external bias of opposite sign but equal intensity of V_{CPD} is applied to nullify the resulting current.

The value plotted on the potential data channel during a KPFM procedure is the inverse of the intensity of the bias applied to fulfil this condition. Of course, this is a very simplistic view of the resulting electric field between the tip and the sample, and some

practical aspect and limits of the whole procedure will be highlighted in the next section of this chapter.

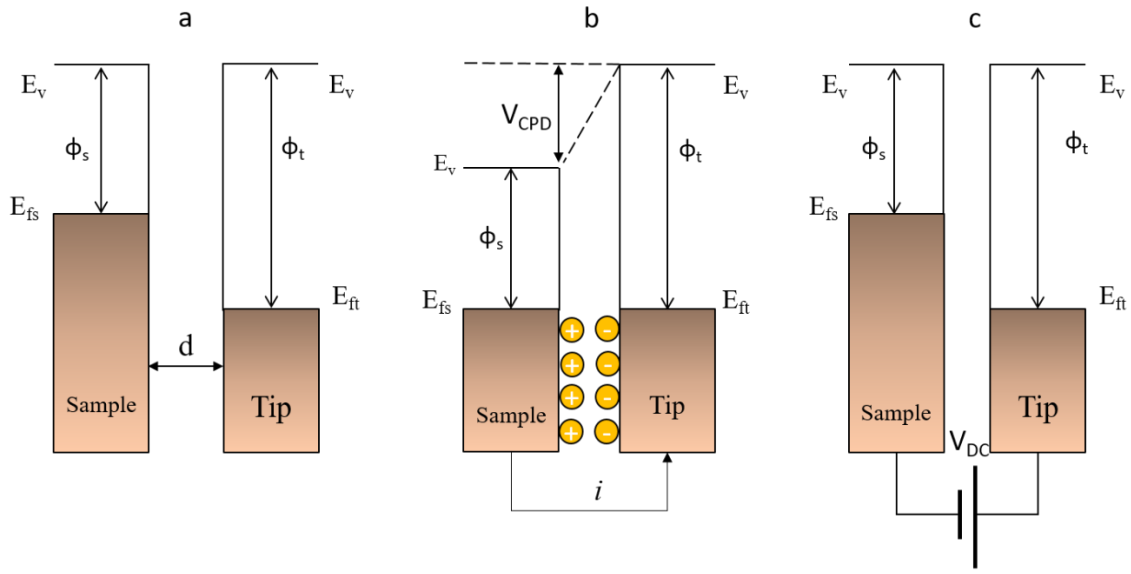

Figure 1.1 Electronic energy levels of the sample and AFM tip for three cases*: (a) tip and sample are separated by distance d with no electrical contact, (b) tip and sample are in electrical contact, and (c) external bias (Vdc) is applied between tip and sample to nullify the CPD and, therefore, the tip–sample electrical force. Ev is the vacuum energy level. Efs and Eft are Fermi energy levels of the sample and tip, respectively.*

In its first set-up, a single-pass tapping scan is employed, driving the cantilever vibration slightly above the resonance frequency to measure the topography and by applying an AC voltage at the resonance frequency to measure the effect of V_{CPD} between the tip and the sample. The intensity of the field is indirectly probed by measuring the effect on the oscillation amplitude of the cantilever, during the part of the cycle in which the tip is not in contact with the substrate. The potential field will act as a net attractive or repulsive force with intensity depending on the distance between the tip and the sample, with the average effect measured by the system to apply point by point a DC potential of opposite sign to nullify that force.

The force felt by the cantilever will be proportional to the overall difference of potential between the sample and tip, which can be divided into the constituent components in the following way:

- The AC signal used to create the vibration: $V_{AC} \sin(\omega_{elec}t)$.

- The intrinsic bias between the sample and the material due to differences of work function, defined as sample relative to the tip: V_{CPD}.

- The external DC bias applied by the system to nullify the effect of V_{CPD} : V_{DC}.

Using the above terminology, and defining the tip-sample capacitance as C(z), we can express the overall force induced on the tip as:

$$F_{elec} = \frac{1}{2}\frac{\partial C}{\partial z}V^2 = \frac{1}{2}\frac{\partial C}{\partial z}\,(V_{DC} + V_{AC}\sin\omega_{elec}t - V_{CPD})^2$$

$$= \frac{1}{2}\frac{\partial C}{\partial z}\left[(V_{DC} - V_{CPD})^2 + 2(V_{DC} - V_{CPD})(V_{AC}\sin\omega_{elec}t) + {V_{AC}}^2\sin^2\omega_{elec}t\right] \quad (1.3)$$

A common way to further expand this equation to have a simple relationship between different frequencies and which components affect each, the trigonometric identity $\sin^2(u)=[1-\cos(2u)]/2$ can be used, obtaining:

$$F_{elec} = \frac{1}{2}\frac{\partial C}{\partial z}\left\{\begin{array}{c}\left[(V_{DC} - V_{CPD})^2 + \frac{1}{2}{V_{AC}}^2\right] + \\ +[2(V_{DC} - V_{CPD})\,(V_{AC}\sin\omega_{elec}t)] - \left[\frac{1}{2}{V_{AC}}^2\cos 2\,\omega_{elec}t\right]\end{array}\right\} \quad (1.4)$$

The interesting part of this representation is that we now have the force expressed as three terms, one of which is constant and the only unknown parameter is the one we want to measure, V_{CPD}, with two periodicities at frequency ω_{elec} and $2\omega_{elec}$.

By using an independent lock-in amplifier to measure the induced amplitude at ω_{elec} and a dedicated feedback circuit to tune V_{DC}, it is possible to now measure the V_{CPD}, while at

the same time it is also still technically possible to monitor the effect at $2\omega_{elec}$ to image variations in capacitance gradient.

This first iteration of the technique, based on the detection of the influence of the potential field induced by the CPD on the oscillation amplitude, with the system point by point measuring both topography and potential in a single pass, is still present in systems as AM-KPFM (Amplitude Modulation – KPFM), **fig. 1.2 (a)**. From this first study, some limitations of the technique were observed. In particular this results in a decrease of CPD, and hence resolution, over time, most probably due to dipole realignment of water molecules on the surface or an increase of contaminant on the tip over time during the measurement [2].

This first experimental setup was soon employed to show how this technique allowed the correct identification of surface features like grain boundaries that were usually not possible to distinguish on the height channel, but that became immediately visible with KPFM. In particular, single layer differences on HOPG (highly oriented pyrolytic graphite) that were hardly visible in height channel, presented clear differences on the CPD channel. This evidence led to the realisation of the main field of application of KPFM for 2D materials like graphene, showing strong dependence of the work function to the number of electrically connected layers probed by the system [3]. Furthermore, in these first studies, KPFM was shown to be incredibly precise in characterizing how corrosion affects different metals and how positive and negative types of doping were distributed and imaged in silicon surfaces. This field of research represented for years the main field of application of KPFM, allowing the study of semiconductor devices that were becoming smaller and smaller [4], [5].

The necessity of increasing the limits of lateral resolution for CPD detection stimulated the study of which parameters were the most important to improve the measurements, in particular the effect of different tip shapes and tip-sample distance [6], which are still the main factors influencing the experimental setup in modern systems. Tips needed to become sharper, with half angles as small as possible, around 18° today for the standard probes made by Bruker® [7], and with smaller diameter, moving from around 40 – 50 nm tip diameters of twenty years ago to the nominal 5 nm used in almost all the measurements in this thesis, considered the gold standard for the technique. These considerations greatly affect the capacitance effect measured between tip and sample, since the closer you get, the bigger portion of the tip will be involved in the detection of the CPD. In addition, improving the tip dimensions allows the use of lower lift height between sample and cantilever, hence decreasing the necessary oscillation amplitude and decreasing the overall forces necessary to control the whole system.

The necessity of constantly increasing lateral resolution for semiconductor devices and the characterization of doping effects soon led to the development of a new and more advanced approach [8]. In this new set-up, that is now referred to as FM-KPFM (Frequency Modulation - KPFM), the system directly measures the effect of the CPD induced force on the cantilever by measuring the induced resonance shift at the second resonance frequency while keeping the amplitude constant, **fig. 1.2 (b)**.

The resonance frequency varies as a function of the force gradient according to:

$$\omega_0{}' = \sqrt{\frac{k - \partial F/\partial Z}{m}} \approx \omega_0 \left(1 - \frac{1\partial F}{2k\partial Z}\right) \tag{1.5}$$

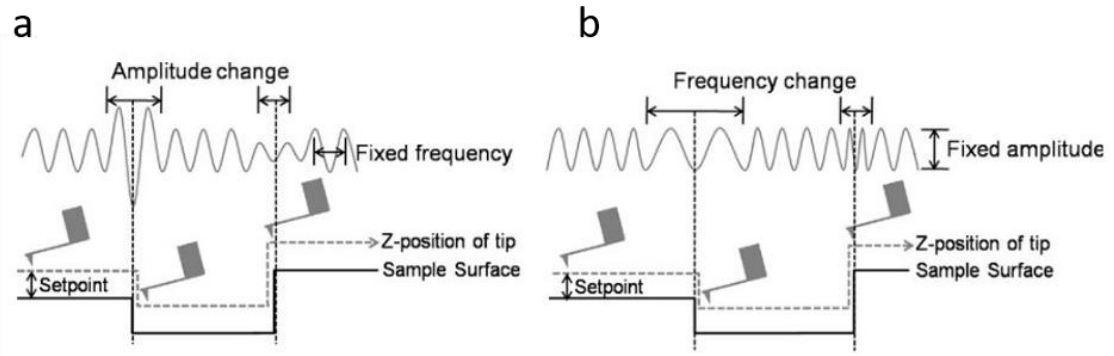

Figure 1.2 Schematic representation of driving principles for AM and FM AFM Tapping modes*. (a) In an amplitude modulated tapping procedures, the measured quantity is the change in amplitude and the constant quantity is the frequency. (b) In a frequency modulated tapping procedure, the measured quantity is the change in frequency and the constant quantity is the amplitude. In KPFM, the procedure is the same, but the measured values are used to tune the applied AC bias to keep the constant quantity at the set value, instead of controlling the vertical position of the tip. Adapted from* [9].

The proper measurement of this shift is achieved by completely separating the two frequencies that drive the system: the cantilever is oscillated at the first resonance frequency, which is used for the height detection, while the AC bias applied to the cantilever is now driven at the second resonance frequency, with reduced artefacts coming from the crosstalk between the two channels [10]. This second frequency is generally many times higher than the first one, and the induced effect in each feedback channel is well defined and differentiated with the proper control system capable of frequency modulation, FM, that would give in future the name to the technique.

Previously, high quality factor (Q) cantilevers were difficult to control with amplitude modulation because of their vibration energy decline, and thus the rate at which the amplitude is damped over time, is very slow. This greatly limited the rate at which the system could correctly detect the amplitude modifications and feedback this value for force detection. This effect is even worsened in vacuum, where there is not the damping effect of the air increasing the rate of the amplitude decline, hence further increasing the effective Q factor of the cantilever. FM-KPFM systems instead overcome this limitation,

and even though AM-KPFM in UHV was later proven to be possible using the amplitude variations at the second resonance [11], it remained the preferable choice, with studies pushing the limits of the technique in UHV conditions at low temperatures to achieve single adatoms resolution in semiconductors [12]. In FM-KPFM, the cantilever is seen as a mechanical resonator within an oscillator, with the highest output signal corresponding to the output of the system at the resonance frequency, which is then measured using a frequency demodulator. In this configuration, a higher *Q* factor means that the cantilever behaves in a way that approximates a perfect resonator, with a smaller frequency fluctuation, which would be seen as noise at the demodulator [13].

Due to the lower sensitivity at the second resonance, normally higher AC voltages need to be applied, which in some cases induces crosstalk with the height data or induces band bending in semiconducting samples due to the tip accentuating the local effect of the applied voltage [14]. Nonetheless, FM-KPFM quickly became the standard methodology for high resolution studies, with applications in distinguishing component distribution in metal nanoalloys [15], high resolution studies of *pn* silicon junctions [16] and surface defects [17], charge transfer on transistor gates [18] , to map potential distributions [19] and decipher individual dopant localisation [20] in polarised devices as well as more generally corrosion science [21]. While as described, FM-KPFM presents the highest lateral resolution [22], it is also highly sensitive to the *Q* factor of the tip or more broadly the ability to properly detect the exact value of the resonance frequency of the cantilever. Despite modern systems having algorithms that automatically simplify all the necessary procedures for this purpose, AM modulation may potentially be the better procedure for substrates that present particular difficulties like adsorbed layers of contaminants or soft substrates that may contaminate or change the tip and cantilever properties, particularly when working in humid conditions or if the lateral resolution is not the main concern.

As a final summary of these two main detection techniques:

- AM-KPFM: The changes of amplitude induced by the applied AC voltage close to resonance frequency are monitored and the opposite DC bias necessary to nullify the vibration is the CPD between tip and sample. Low spring constant cantilevers are necessary to obtain sufficiently large mechanical deflections. However, close to the first resonance, tips have long settling time and detection of the amplitude variations takes longer, limiting the scanning speed. AM-KPFM is sensitive to the total intensity of the force field, with a resulting measured CPD value affected also by the area surrounding the point probed.
- FM-KPFM: The resonance frequency shift induced by the applied AC bias is measured at the second resonance frequency and the parabolic dependence between frequency shift and applied bias is used to evaluate the CPD. Stiff cantilever with high Q factor are allowed and better topography at lower lift heights is obtainable to improve correlation between height and potential. FM-KPFM is sensitive to the force gradient, which depends more on the interaction with the tip than the effect on the whole cantilever structure, allowing better lateral resolution.

Both techniques can be operated in contact or non-contact mode, with only FM-KPFM presenting clear preference for non-contact mode to avoid mechanical cross-talk between channels during tapping procedures [23]. During non-contact procedures, a second pass of each line, called interleave, is added to the scan following two possible configurations:

- $Z_{interleave} = Z_{(0)} + Z_{offset}$ in the linear mode, in which noise coming from the movement of the tip up and down to follow the first pass topography is nullified, at the risk of having artefact coming the difference in height in rough surfaces.

- $Z_{interleave} = Z_{(x)} + Z_{offset}$ in "lift line" mode, where instead the tip during the interleave will follow exactly the previously measured profile, allowing a more reliable measurement in rough samples but introducing some mechanical noise if steep changes need to be replicated.

A schematic representation of how the two modes are practically implemented in an AFM system is reported in **fig. 1.3**.

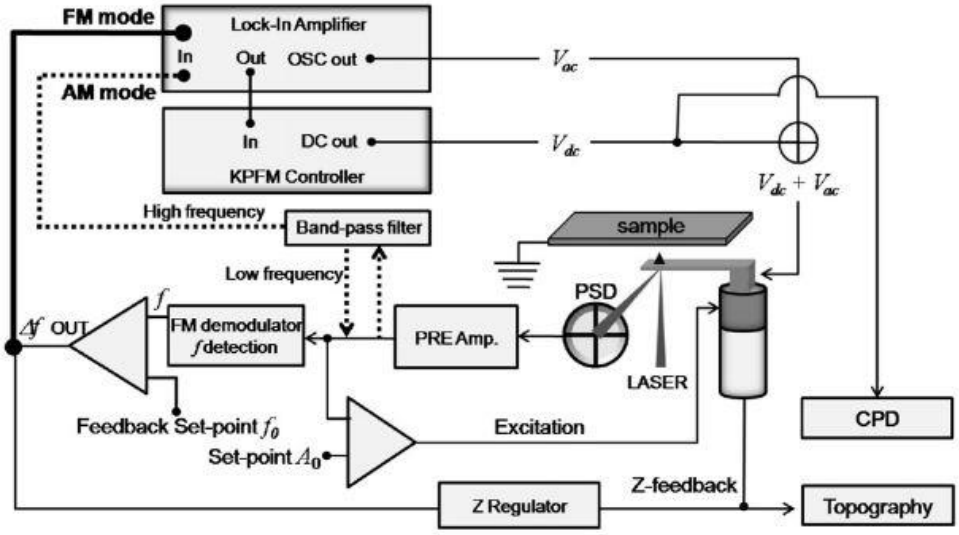

***Figure 1.3. Schematic diagram of KPFM system showing AM and FM mode**. The height control pictured is an FM tapping mode. Taken from* [9].

PeakForce®-KPFM is the most recent development in the evolution of the technique: a double pass procedure using proprietary algorithms from Bruker®. In this technique, the whole cantilever and its holder are vibrated up and down at 1-2 kHz and during each cycle, a force curve is obtained by observing the tip deflection. The approach allows the measurement, instant by instant, of the true force felt by the tip, guaranteeing that the force felt by the system throughout the interval in which tip and sample are engaged is kept at the peak force set point chosen by the user. This allows for each point the

possibility of obtaining complete force-distance curves of the forces felt by the tip during the approach and the disengagement with the sample, and while in lift mode, a better detection of the force gradient, which as stated previously is the main property measured by the cantilever in a FM configuration. In the first pass, topography and nanomechanical properties are measured, and then, at a set lift height, the cantilever may follow the just obtained height profile, while homogeneously oscillating up and down to detect the frequency shifts induced by the CPD force gradient.

This technique expands on standard FM-KPFM possibilities by allowing a better control of the oscillation behaviour under the electrical force field even when the second resonance, which is normally around seven times less sensitive [13], is employed. The main drawback is the complexity of the whole set-up, which adds new elements to the electronic feedback loop system that may amplify the noise, particularly due to imprecise calibration. Still, due the simplicity of use for the end user and the amount of data that is obtainable on a single session, PeakForce KPFM has been the most widely used technique throughout this work for CPD characterization of our samples. In **fig. 1.4** an example of the data that is simultaneously obtainable in a single pass while operating in PeakForce KPFM mode is shown, In this picture of a graphene monolayer, with few islands of two layer graphene, the topography is represented in the top left, while nanomechanical data like adhesion and Young modulus (using DMT model for small indentation for the case of graphene) are represented in the top right and bottom left. Finally, KPFM data is represented in the bottom right, showing the expected high contrast between the basal plane baseline and the in-plane features.

In its future, the KPFM technique is already starting to expand to allow the ramping of a range of voltages for each single scanned point to increase the amount of data that can be reliably obtained in a single scan. This set of data, called Datacube®, will reduce the time

necessary to obtain results and to prepare and optimize the parameters between each scan. In this way, robustness and reliability of data will also be improves as there will be no factors affecting the measurements or the sample between each scan, making it easier to further optimize future scans of the same material.

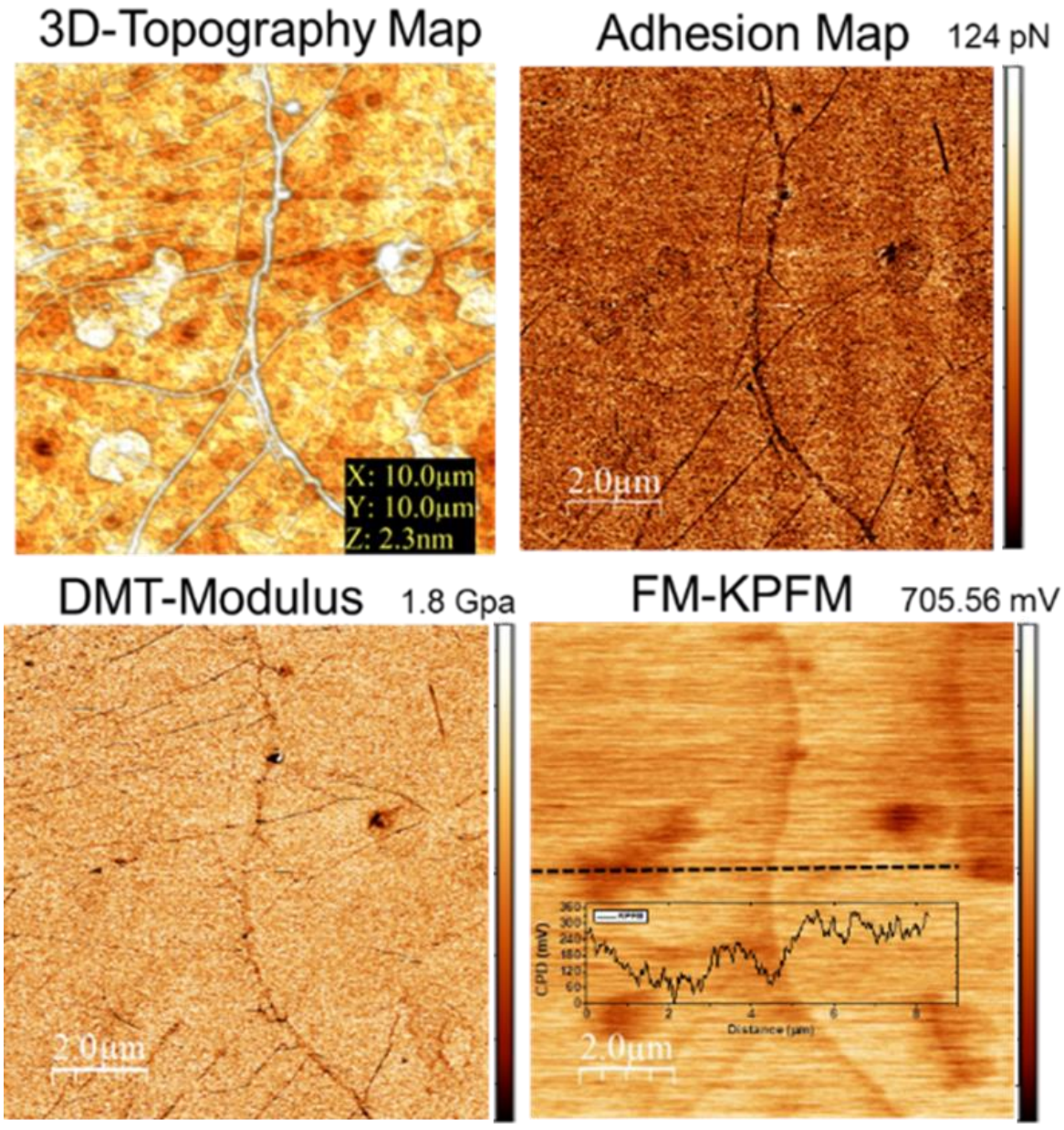

Figure 1.4. Example of data obtainable from a PeakForce-KPFM mode scan. *This set of images represents the amount of information obtainable from a single scan of a CVD graphene monolayer presenting interesting features like small islands of bilayer graphene and well pronounced wrinkles, as visible in the topography, presented in the top left. The PeakForce algorithm is employed to obtain nanomechanical data like adhesion and Young modulus (using DMT model for small indentation for the case of graphene), represented in the top right and bottom left respectively. Finally, KPFM data is represented in the bottom right, showing the expected high contrast between the basal plane baseline and the in-plane features*

1.2 Practical considerations to improve KPFM imaging and limits of the technique

Establishing a direct pixel-by-pixel correlation between the KPFM data channel and the height data channel is a necessity for the characterization of nanoscale materials and devices, but has been proven to be limited by physical constraints even in optimal conditions. Great effort was put into trying to properly model the tip sample interactions [24]–[26], establishing practical advice that still today influence the treatment of KPFM results and the design of the tips.

First, the CPD signal is not only dependent on the capacitance between the tip and the sample, but also on the derivative of the capacitances between surrounding regions on the surface, which is a direct consequence of the long range nature of electrostatic forces acting on the tip in a KPFM scan. A direct consequence of this is that areas with widely different work function difference will not appear to have a sharp and well distinct interface in the KPFM channel, but the supposed step will always appear as a gradual increase or decrease. This consideration is very important when selecting the substrate for the deposition of the materials to analyse, so as to limit as much as possible this convolution effect between the two capacitances affecting the data. Another practical consequence from this consideration is the necessity of bringing the tip as close as possible to the sample, as proven by electric field simulation in later years [27] and comparative studies exploring the effect of tip sample distance in the two main configurations, AM and FM [28]. Of course, it is not always possible to minimize tip-sample distance without drawbacks during the characterization of rough or not perfectly clean samples. Furthermore, bringing the tip as close as possible to the substrate has also the drawback of increasing the effect of the force felt by the cantilever surface [28]. It

was established that a tip designed specifically for KPFM applications should have a minimal cantilever surface area and width, coupled with long and slender tips.

The tips used in this thesis were mainly of two types, both following these design prescriptions:

- PFQNE-AL tips that excel on the minimal surface area and width of the triangular cantilever, specifically designed for KPFM [29], **fig. 1.5 (a)**.
- SCM-PIT tips that instead have a broader use in electrical modes, including conducting AFM [30], and so present the traditional extended rectangular cantilever which is not ideal due to its increased surface area, **fig. 1.5 (b),** compensated in part by a very tall tip, double the height of the PFQNE-AL tip (~12 µm vs ~5 µm).

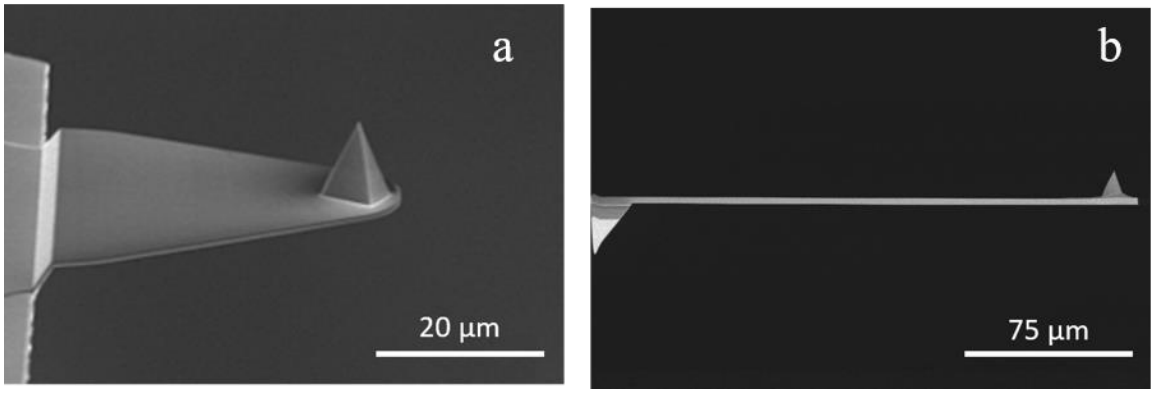

Figure 1.5 SEM pictures of the two main tips used in this thesis. *(a) a PFQNE-AL tip, a triangular silicon tip considered gold standard for KPFM measurements, having very high Q factor and relatively high spring constant for FM and PeakForce KPFM modes. The small dimension minimize the effect on the vibration from electric field interaction with the cantilever structure. (b) SCM-PIT tip, which can immediately be recognised by its standard rectangular shape and long dimension. It is a platinum iridium softer tip that has versatile uses in various electrical modes, with the drawback of the big dimension affecting AM measurements and low spring constant affecting FM modes. Both SEM pictures were taken from the official Bruker® webstore for AFM probes, https://www.brukerafmprobes.com/*

Another factor that influences the tip choice is the tip material and/or coating: during the first years of use, KPFM was employed using only standard AFM tips coated with 10 nm of either Au or Pt, since they were already used in other electrical AFM modes and cheap and widely available. SCM-PIT tips, for example, belong to this family of tips, which primarily are Platinum Iridium coated. The problem with these tips, particularly when imaging rough substrates pertinent to the materials discussed in chapter 5 of this thesis, is that the conductive coating may unsystematically degrade or sustain damage during the scan due to laterally impacting taller structures or even just by losing the coating over long times on the tip apex due to wear during normal scanning. To have more robust tips that would not permanently change their properties due to wear, semiconductor tips without any type of coating were developed [31], quickly becoming the gold standard for KPFM thanks to the possibility of more reliably comparing data coming from different scanning sessions without the necessity of SEM characterization to verify the state of the coating, if quantitative data was extrapolated from the images. PFQNE-AL tips belong to this family, and the only real drawback is the cost, normally up to two times that of metal-coated tips.

Another key aspect to consider when using KPFM in ambient condition is the effect of the usually unavoidable potential shielding by the adsorbed water on top of the sample. Increase and decrease in CPD contrast was proven to happen in samples that otherwise, when analysed in ultra-dry conditions, presented no differences at all [32]. For all of the samples studied in this thesis, generally a previous thermal treatment in a vacuum was employed to reduce as much as possible the thickness and presence of this effect. However, without clean room conditions a small layer is almost impossible to avoid. This is particularly important with application using thermally sensitive organic materials [33]. While as a technique KPFM was born and found its widest use for metallic or semi-

conductor materials, its use during the years has been expanded also to organic or even insulating materials. This will be discussed in detail in chapter 6 of this thesis where we qualitatively analyse latex-graphene composites. In this application, the interpretation of the data does not give information on the work function *per se*, but on the localization of charges under the applied potential [34], which may give insights on the localization and the preferable charge movement in composites with conductive components, or how this component reacts under different external electrical or photovoltaic stimulations [35].

A further limitation that needs to be discussed is completely independent from physical properties of the tip and ambient conditions. The discrepancy of expected CPD values from models, even for simple metal-to-metal or metal-to-semiconductor measurements, may arise from a variety of unexpected bias-dependent interactions between tip and sample. This may be very difficult to compensate for, as it is not always immediately possible to predict the effect of contamination or damage of the tip [36], as it is also dependent on the type of tip and area of the sample probed, which may present component with widely different mechanical and electrical properties [37].

Finally, as mentioned in the introduction, FM-KPFM is particularly sensitive to the calibration of the cantilever resonance frequency, requiring proper characterization of both the first and second resonance to properly work out the frequency shift induced by the CPD field. To summarise, for the most widely used tip, PFQNE-AL, the following calibration steps should be followed:

- Contact calibration on a hard substrate: to properly characterize spring constant, resonance frequency and Q factor.
- Tip shape characterization: if the material mechanical properties are of interest observing indentation on a soft substrate is necessary. In the experiments for this

thesis, the tip was specifically chosen to be used primarily for electrical characterization, and so this step was generally skipped to avoid tip damage.

- Characterization of the work function: on the reference substrate from Bruker®, to check that the proper step structure can be resolved by the tip, for chapter 3, chapter 4 and chapter 6. Freshly mechanically cleaved HOPG for chapter 5 when a better approximation of work function was necessary, avoiding the effect of dirt present in the reference sample.

The Bruker® standard sample used for this type of calibration is a lithographically fabricated 50 nm thick film of Au and Al, on top of a silicon chip with reduced layer of silicon oxide to optimize grounding. More advanced calibration of the tip work function have been developed in literature [38], but they are generally employed for simple and more homogeneous systems where it is possible to properly model the sample properties to achieve correct and precise work function measurements [39], which is not as easy or even possible for the nanomaterials characterized in this thesis. Once appropriately calibrated the tip was then kept in a probe holder specifically used for KPFM characterization and it was never used for any other purpose, to avoid degradation of the properties. Periodically during long scanning sessions, or anytime the probe holder was mounted, quick thermal tune calibration was performed to verify consistency of the expected resonance frequency value.

Chapter 2
Basics of other characterization and deposition techniques, and introduction to graphene

As presented in the previous chapter, KPFM is a powerful characterization tool to obtain topological and electrical properties of the analysed sample in a single step. An advanced mode like PeakForce-KPFM allows also to add mechanical information to the set of data available with a single pass. Still, to gain a better understanding of the chemical and structural properties of the material investigated and its surrounding, other complimentary characterization techniques are necessary.

Raman spectroscopy represents an invaluable tool in the study of 2D materials as it allows the characterization of properties like functionalization of the plane and edges and the identification of monolayer areas. In the case of graphene, Raman data has been used to model mechanical properties like the amount of strain in the basal plane, which can then be compared with the set of data coming from electrical and mechanical characterization operated by AFM [40].

Scanning Electron Microscopy (SEM) can instead be used to quickly image large areas of the sample surface that would not be possible to characterize with the AFM, whose resolution is limited to a square of around 90 μm by 90 μm, or that would require a lot of time to be properly imaged by AFM, which is limited to 2 Hz raster scan movements. Another powerful use of the SEM is the possibility of using the electrons penetration in the sample to visualize underlying features or overcome contaminant on the surface that would instead not be possible to be imaged by the AFM.

The following sections of this chapter will introduce the basics of these complimentary characterization tools employed in the experimental sections of this thesis, followed then by an analysis of the different deposition techniques used to prepare the samples and how they affect the quality of the AFM scan. At the end, a brief introduction to the main 2D material used in this thesis, graphene, is presented.

2.1 Raman spectroscopy basics

When a sample is irradiated with a laser source, the interaction between the molecules or atoms and the incident laser distorts (polarises) the cloud of electrons around the nuclei to form a short-lived "virtual state". From the decay of this state when the source is removed, three types of scattering may be detected: Rayleigh scattering, Stokes scattering and anti-Stokes scattering, with the last two forming what it is usually referred to as Raman scattering [41].

Rayleigh scattering is the result of elastic collisions between photons and matter, producing re-emission of radiation with the same frequency and phase as the impinging electromagnetic field. Inelastic scattering of photons occurs by excitation of the system into short-lived virtual state, followed by relaxation to a phonon-mediated vibrational level about the ground state, resulting in emission of a photon at an energy lower than that of the incident photon. In a phonon emission event the molecule loses energy, incident photons are up-shifted in frequency, thus generating anti-Stokes line [41], with the resulting interaction cross-section significantly reduced compared to Rayleigh scattering. **Figure 2.1** shows a schematic diagram of all three possible scattering events. An important characteristic of Raman scattered photons is that they can only differ from the excitation energy by multiples of the phonon energy.

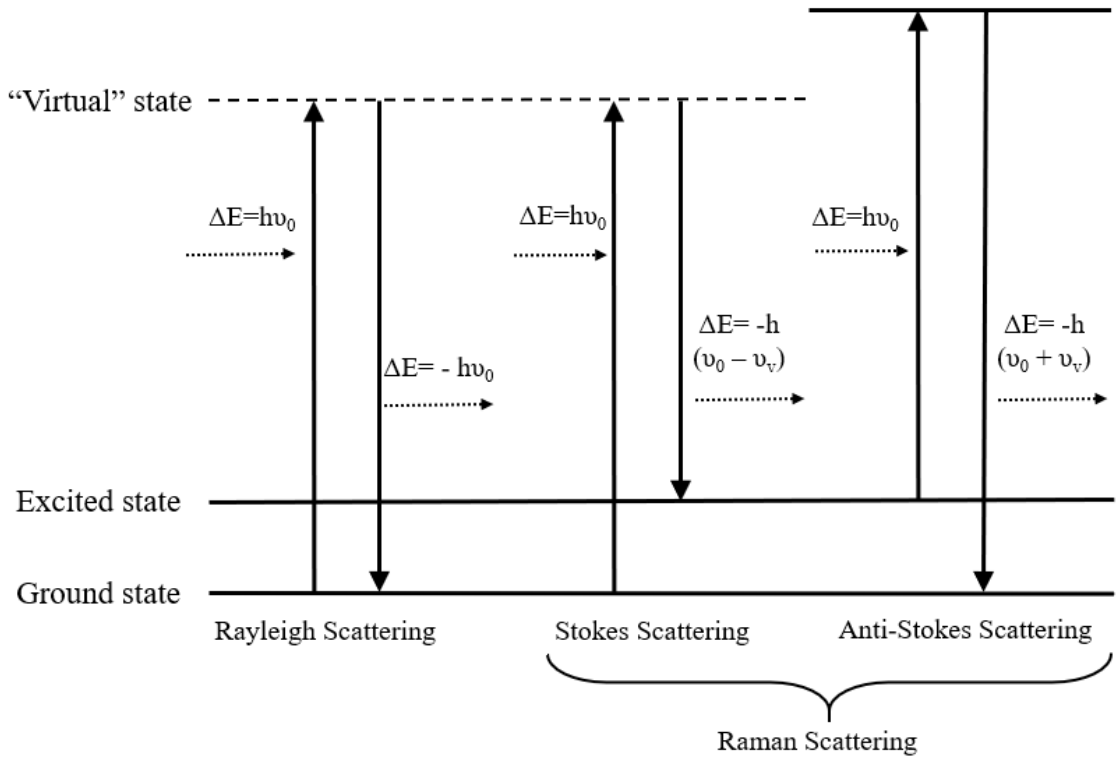

Figure 2.1. Representation of the three scattering processes. *Given the same amount of excitation energy in the system ($\Delta E=h\upsilon_0$), three main scattering processes may happen. If the excited electrons move from their ground state to the virtual state under the radiation source and then they go back to that state in a perfectly elastic scattering, we have Rayleigh scattering. If the system absorb some energy and hence release a lower amount of energy, we have Stokes scattering. On the opposite, if the system absorb part of the radiation energy, we will have anti-Stokes scattering. These last two type of inelastic scattering form what is called Raman scattering.*

A Raman spectrometer consists of a laser as a photon source, which is transferred through a number of mirrors and filters that adjusts the diameter and collimates the laser beam. The laser beam is directed onto a rejection band filter (notch filter), after which it passes through a microscope lens to be focused on the sample mounted to the sample stage. The beam reflected from the sample passes back through the microscope optics and through a monochromator. Raman shifted radiation is detected and analysed with a charge-coupled device (CCD camera), followed by data acquisition and curve fitting using the proprietary computer software.

Raman spectroscopy is a very attractive and non-destructive technique for studying the phonon and electronic structure of carbon materials, such as carbon nanotubes [42] and graphene [43]. Raman spectroscopy has been used in Chapter 4 and Chapter 5 as a powerful tool to verify the quality and the state of the graphene flakes. In particular, in Chapter 4 to verify the monolayer nature of the analysed flakes and to gain some insight on the strain that the blister structures impart during laser irradiation, based on previous results found in literature [40]. In that study, the Raman spectrometer system was also used as the source of the high intensity laser used to modify the monolayer structure, by operating the system at 100% laser power emission and for longer time than usually necessary for the characterization. In Chapter 5, it was again used to test the amount of strain applied to graphene flake wrapping around the silver nanowires.

2.2 SEM basics

Scanning electron microscopy (SEM) employs a focused primary-electron beam to scan the sample surface in a raster fashion over a user defined rectangular area. Primary electrons penetrate the sample surface, interacting with atoms within a 3D volume in the analysed specimen known as the interaction volume, as shown in **fig. 2.2**. Scattered electrons travelling through the interaction volume can be divided into two general classes based on their measured energy compared to the primary source. In inelastic scattering, electrons scatter through the target material while losing energy and randomly changing direction in a series of atomic collisions, producing in each of these events secondary electrons, backscattered electrons, X-rays, heat and light.

The spot size of the beam on the sample surface determines the resolution limit as SEM cannot resolve any features smaller than the spot size, which can be as small as five

nanometres, with the drawback of higher energy densities and risk of affecting the sample at those resolutions. Other parameters affecting resolution include beam penetration and the sample atomic number. Analytical information of a specimen can be gained by detecting two main signals, secondary electrons and backscattered electrons: secondary electrons provide high-resolution imaging of surface morphology and they can be generated by primary electrons entering the thin surface layer but also by backscattered electrons on their way back through a larger region of the surface [44]. They possess low energy (<50eV) and originate within a few nanometres of the surface.

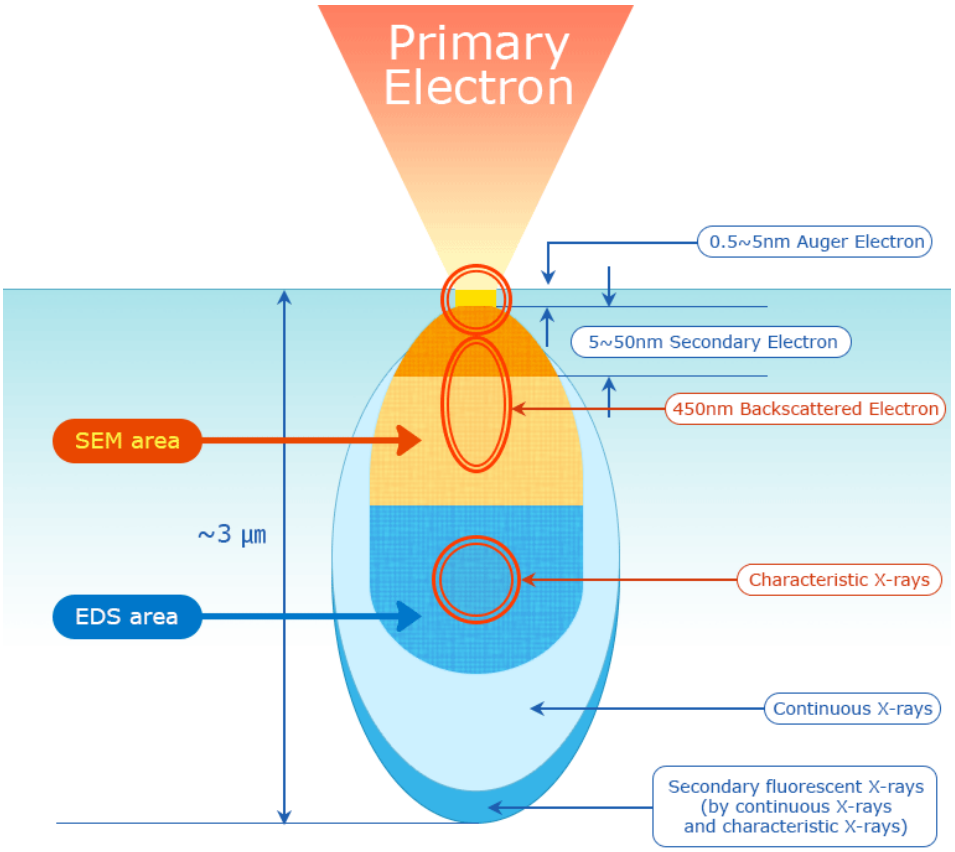

Figure 2.2. Schematic representation of the type difference areas of interaction between primary electrons and interaction volume. *When the primary source of electrons interacts with the substrate, the energy determines the dimension of an interaction volume affected by the process. Secondary electrons will carry the best information about the morphology of the sample, while electrons coming from deeper parts of the sample may be analysed to gather information on the elemental composition of the sample with a technique called Energy Dispersive X-Ray Spectroscopy (EDS or EDX). Extracted from https://www.nanoimages.com/sem-technology-overview/*

Elastically backscattered electrons are characterized by high energy which varies directly with the specimen's atomic number and provides elemental composition information, as well as surface topography imaging [45]. This can also be employed to map the atomic composition in the specimen with a technique called EDX (Energy-Dispersive X-ray analyses). EDX works by detecting the X-rays emitted by the analysed surface, which are originated by electrons moving from high energy levels to holes created in the inner shells, where the incident beam has excited and removed electrons. By analysing the energies of the emitted X-rays, it is possible to correlate them to specific discrete energy differences between two specific shells of specific atomic structures.

The accelerating voltage defines the amount of energy carried by the primary electrons. Electrons with higher energy produce a larger interaction volume and generate higher energy signals, while low accelerating voltages provide information from the surface of the sample. Sample composition strongly affects the depth and shape of the interaction volume, for example the beam penetration for carbon is about 1 μm at 10 kV, and decreases with increasing atomic number [46].

2.3 Deposition techniques

The analyses of 2D materials presents particular challenges due to their nanoscale thickness, which of course requires ultra-smooth and clean substrates, and the necessity of preserving the monolayer structuring by avoiding re-stacking during the deposition process. A homogeneous distribution throughout the sample is also necessary, to guarantee that the characterization operated in certain areas of the sample is representative of the properties of the deposited material in all of it. Every deposition analysed in this work for the characterization of the dispersion quality, such as average thickness and

lateral dimension, has been deposited on polished silicon obtained from a sealed silicon wafer cleaned with IPA. When KPFM was required, either the silicon chip was grounded to the metallic base with silver paint, or a microscope slide was covered by 10 or 50 nm of sputtered gold to improve the electrical connection between the sample and the base. Still, even the best substrate cannot improve the experimental conditions without a proper deposition technique optimizing the creation of a homogeneous distribution of the 2D material on the surface, minimizing restacking of the 2D material layers and the amount of residue remaining on the substrate during the drying process of the solution. The 3 main techniques used in the nanomaterial sector are here introduced, followed by a summary of the conclusion on which one represented the best approach for the type of samples characterized in this thesis, with the resulting data presented in Chapter 3.

2.3.1 Drop casting

The simplest deposition technique is represented by the act of directly drop casting from a calibrated micropipette for deposition of small and controlled quantity. The solvent is then allowed to evaporate at room temperature or at specified temperatures on a hotplate depending on the solvent boiling point. The advantage is the simplicity of use and the possibility of depositing large quantities, but there is no control on the density and homogeneity of the film thickness.

2.3.2 Spin-coating

This technique works by utilising the centrifugal force to remove the excess liquid from a rotating substrate surface, hence significantly increasing the evaporation rate of volatile solvents [47]. It has been widely used by researchers for many years due to its relative simplicity, low cost, and ability to produce films with accurate thickness down to the nanometre scale. Thickness can be controlled by varying parameters such as the rotation

speed, rotation time, and the concentration of the solution, with of course increasing time and speed decreasing the film thickness. Drawbacks associated with this technique are that it is normally not suitable for uniform deposition on large substrates and in general the process is highly inefficient with just a small quantity of the material applied actually remaining on the substrate, around 2-5% depending on parameters and dimension [47].

2.3.3 Langmuir Techniques

Langmuir-Blodgett (LB) and Langmuir-Schaefer (LS) are extremely promising deposition techniques when the smallest possible thickness of films or uniformity of the deposited material needs to be achieved, while at the same time allowing coverage of large surfaces, with the added benefit of being repeatable to increase the number of layer in a controlled way. In this technique, individual molecule or particles are deposited at the water-air interface in a small bath, enclosed by two moving barriers that can compress the amount of material floating at the surface to compact it and control density. The Langmuir-Blodgett technique has a very long history, with the first observation of the principle going back as far as 1774 when Benjamin Franklin described in a letter to the British Royal Society [48] how a very small quantity of oil could spread over large areas of a pond that was wavy under strong wind, making the covered part “as smooth as a looking glass”. Irving Langmuir, followed by his assistant Katherine Blodgett, were the first to systematically investigate the nature of these floating monolayers at the liquid-gas interface, both receiving a Nobel Prize for their results. However, only relatively recently the technique has found widespread use in the nanomaterial field.

To be properly deposited using this technique, a molecular material must have amphiphilic properties, hence having both a hydrophilic and hydrophobic part. This property leads to a specific organization of their molecular structure at the water/air

interface, with the hydrophilic end orienting toward the war and the hydrophobic one instead oriented toward the air. For solid materials, like the 2D nanomaterials that are the subject of this study, the main condition necessary to achieve the formation of a film is that they are not dispersible in the liquid subphase, hence remaining trapped at the air-water interface. Originally made of wax, today troughs are made of Teflon to improve the containment of the water and normally the process can be fully automated by a software connected to a sensor to constantly monitor the surface tension and the barriers to control their movement. The process can be monitored by measuring the surface tension of the water surface [48]. Addition of surface-active materials will modify the surface tension of the subphase, with the deviation from that of the pristine liquid (water) being referred to as the surface pressure (analogous to the pressure of an ideal gas in a 3D system). These measurements are made using the Wilhelmy plate technique [49], which employs a thin metal plate such as platinum (Pt) being pulled by the water bath with a force (F) measured by the system, with the surface tension (Π) calculated using the following:

$$\Pi = \frac{\mathrm{F}}{2(W + t)} \tag{2.1}$$

Where W is the width of the wetted part of the plate, and t is the thickness, hence forming at the denominator the perimeter of the wetted plate. This simple approximation relies on the assumption that the contact angle of the subphase with the plate is negligibly small. This is achieved by the use of Pt plates due to their very high surface energy [50].

The trough containing the water, which has to be strongly hydrophobic to induce the tallest possible meniscus, evolved in the 1970s with the use of a moving barrier, allowing more control of the distribution of the film on the surface while at the same time allowing new studies of the film behaviour after compression and de-compression cycles thanks to the use of automated barriers, as seen in **fig. 2.3 (A)** using our own system.

The inlet pictures represent microscope images of deposited Molybdenum Disulphide (MoS_2) on silicon after the material is picked up for further characterization at different parts of the cycle, resulting in different densities. In **fig. 2.3 (B)** it has been plotted the different area coverage that can be selectively obtained just by picking up the substrate in different part of the cycle. Deposition of different masses of materials, in combination with control of the barrier separation, allows the user to produce films from highly sparse to nearly full density, in principle.

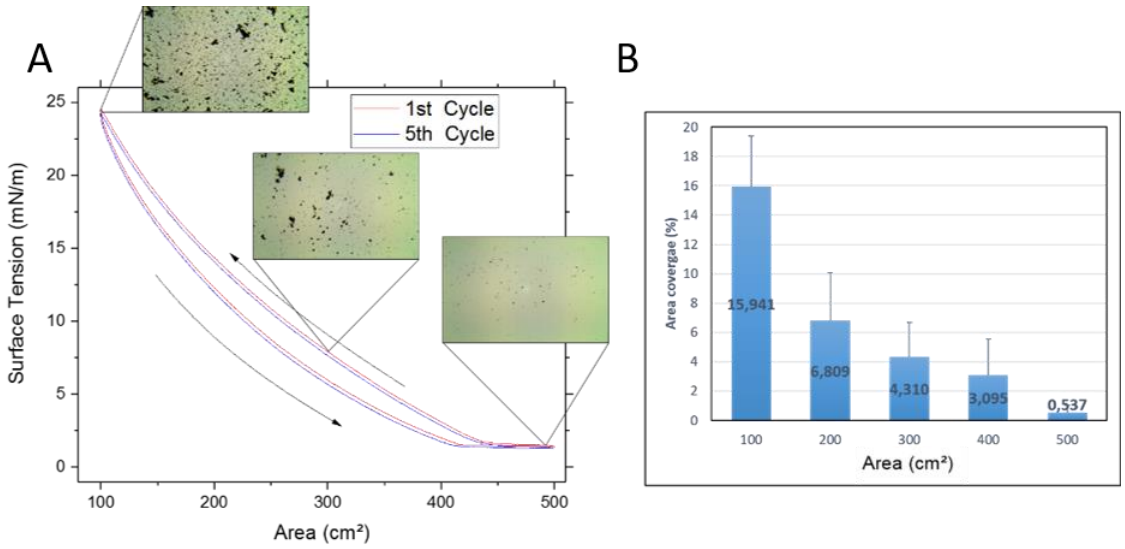

Figure 2.3. Experimental results of the control of the density of flakes with Langmuir-Schaefer. *(A) shows an example of surface tension/area plot coming from the sensor after a full barrier cycle and after 5 cycles after the deposited MoS_2 solution is fully evaporated leaving only the nanomaterial flakes. The microscope images show how it is immediately visible the difference of the density on deposited flakes on the substrate at different level of closure of the barrier. In (B) the same results are presented by plotting the resulting area coverage depending of the total remaining area in the trough for five different points, with 500 cm^2 representing the starting point.*

Based on the process of transferring the film onto the substrate, two methods of Langmuir deposition can be defined. The first one to be developed, and the one most commonly used, was introduced by Blodgett and involves a substrate that is immersed prior to the deposition and compression of the surfactant, and involves a vertical extraction in which the barrier compresses the film to maintain homogeneity while the substrate is raised from

the water. In the alternative technique, called Schaefer's method [51], the substrate is put into contact with the water surface horizontally and hence parallel. The advantage is that the surfactant feels less disruptive forces during the process. Furthermore, the two techniques differ also on the preferable wettability properties of the target substrate. The Langmuir-Blodgett approach favours hydrophilic substrates, while Langmuir-Schaefer favours hydrophobic ones to minimize the wicking of water between the film and the substrates, but also hydrophilic substrates may be employed if the floating film is sufficiently dense and rigid.

Since flakes of 2D nanomaterials tend to create rigid films, the LS technique is the most suitable one. A drawback of this technique is that generally solvents used for the liquid exfoliation process have low vapor pressure, hence taking more time to evaporate and being removed from the bath, which is a non-ideal condition for this technique. A previous work of our group extensively analyzed the spreading properties of the most common solvents using experimental parameters like the Hansen parameter to predict the best choice for the creation of stable LS film at the air-water interface [52].

2.4 Quality of deposition depending on the deposition technique

In general, for the purpose of single flake or few flake characterization, spin coating is the technique that has the best trade-off between advantages and disadvantage. The deposited solution, as shown in **fig. 2.4 (A)**, tends to present homogenously distributed and well-isolated flakes, which for the purpose of the KPFM analyses presented in Chapter 3 is the best condition. Spin coating, as previously mentioned, is a very wasteful

technique, with only a small percentage of the material actually depositing on the substrate while the rest is expelled by the centrifugal force. This aspect, normally considered a drawback, for AFM purposes could represent an advantage, with lower concentration and restacking of flakes and most of the residue in suspensions getting expelled with the solvent. In **fig. 2.4 (B)** an example of these residue, the circular element in the top half, is shown in a sample obtained with drop casting. These contaminating elements hinder the proper detection of the morphological properties of the flakes trapped inside them, and present very low work function that make KPFM data unobtainable.

In **fig. 2.4 (C)** a very bad example of some of the problems arising from LS deposition is represented, with huge part of the sample covered by residuals of solvent that stay permanently attached to the substrate, making proper AFM and KPFM characterization very hard. In this case, the main obstacle is represented by the amount of time necessary for the solvents and surfactants to be completely removed from the air-water interface. While it is possible to overcome this problem by properly selecting the solvent and leaving the necessary amount of time to the bath to remove as much of it as possible through evaporation, this problem makes LS an inconvenient technique when a homogeneous and continuous film is not required. This aspect is also particularly evident while trying to image materials like MoS_2 that tend to present reactive edges, which may strongly bind to the surfactant particularly for flakes of small dimensions like the ones produced by liquid exfoliation, like the ones used in this chapter and in chapter 3. Liquid exfoliation tends to produce small flakes, as visible from the previous AFM images, hence making edge effects more noticeable, and particularly in an environment that undergoes strong mechanical and chemical stress like during the sonication step. Bigger flakes tend to form aggregates that are normally too dense for proper AFM and KPFM characterization.

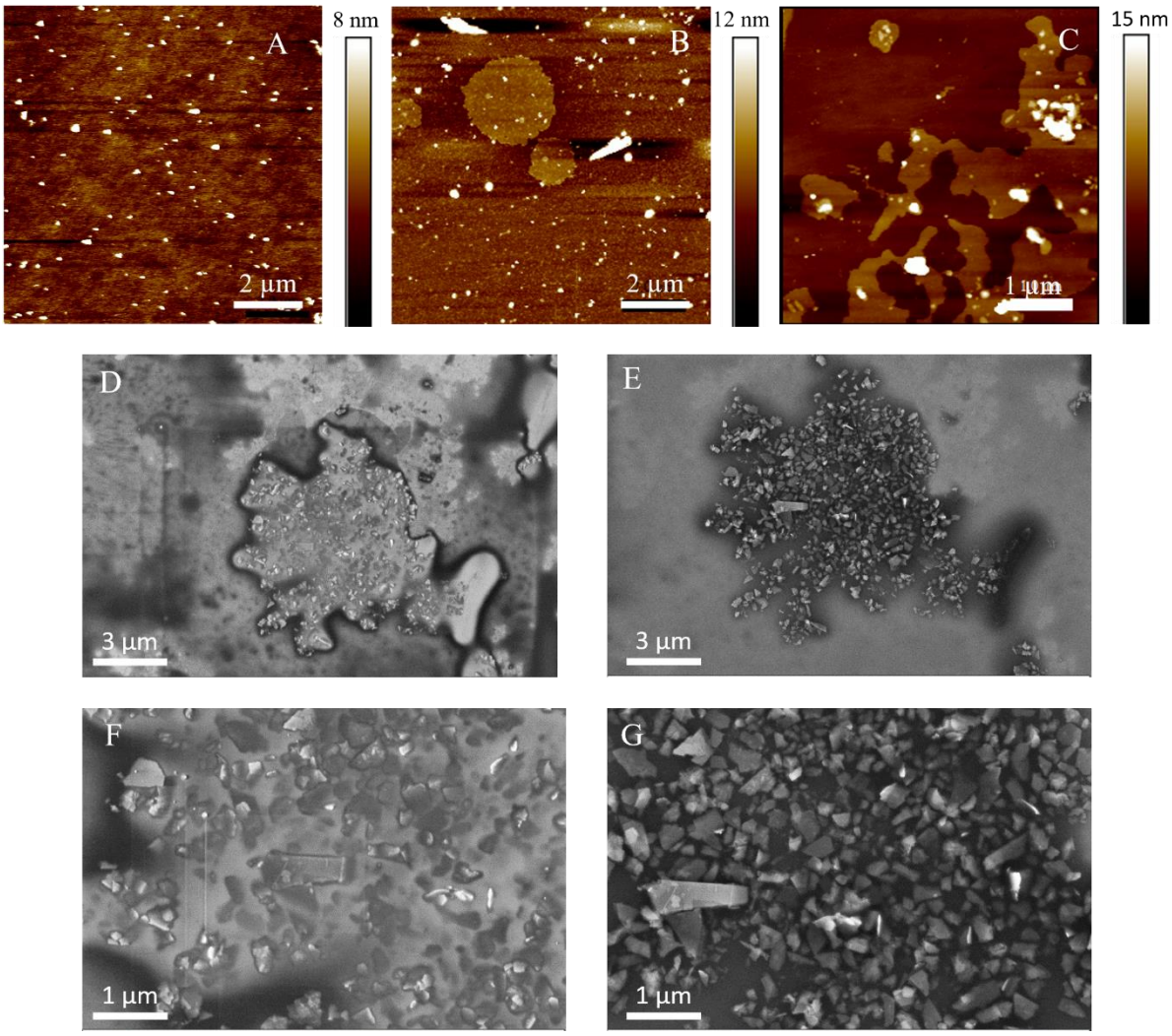

Figure 2.4 Example of AFM characterization for different types of deposition and SEM images of contaminating residuals obstructing the proper AFM characterization of MoS_2 when deposited with the LS process*. (A) Spin-coated sample, (B) example of residual in a drop casted sample, (C) extreme case of solvent contamination of the substrate of an LS deposited sample, (D) and (F) SEM images of a sample under a primary electron beam accelerated at 1 kV, showing how the contaminating layer present in the AFM images is clearly visible also here, (F) and (G) SEM of the same areas when the beam is accelerated at 5 kV, showing the expected shape of the flake.*

In **fig. 2.4 (E-D)** and **fig. 2.4 (G-F)**, SEM was used to analyse this type of big clusters. The effect of the residues in completely covering and surrounding the MoS_2 flakes as suggested by the AFM characterization becomes even more visible, with the electron beam at low voltage (1 kV on the left), not being able to properly penetrate and resolve the morphology of the flakes. Instead, at higher voltages (5 kV on the right), the electrons

are able to penetrate the contaminating layer and properly resolve the flakes, which instead would not be possible with the AFM without picking up large quantity of contamination with the tip, a process that would also modify the apparent work function of the tip for the KPFM characterization.

As a summary, after experimenting with all these techniques, I have employed spin coating as the main deposition technique thanks to its ability of greatly reducing the amount of contaminant remaining on the substrate and properly disperse the flakes for better KPFM characterization. Instead, when a homogeneous ultra-thin film is required for the functionalisation of specific substrates, spin coating is not able to achieve sufficient control of parameters like total coverage and thickness, making Langmuir-Schaefer the preferable options.

2.5 Introduction to Graphene

Graphene was the first properly isolated and characterized 2D material, consisting of an atomic monolayer of carbon atoms that are bonded together in a hexagonal lattice, and it can be described as an individual atomic plane extracted from graphite, or an unrolled carbon nanotube [53]. Nonetheless, in literature it is also generally accepted that graphene may also refer also to a few layer material consisting of multiple layers of monoatomic graphene, with 10 layers generally accepted as the limit before it is considered again graphite or nanoparticulate graphite [54]. The exceptional theoretical properties of graphene have created an entire new field of nanomaterials research, with the hope of finding other 2D material presenting emerging properties at the single or few layer scale.

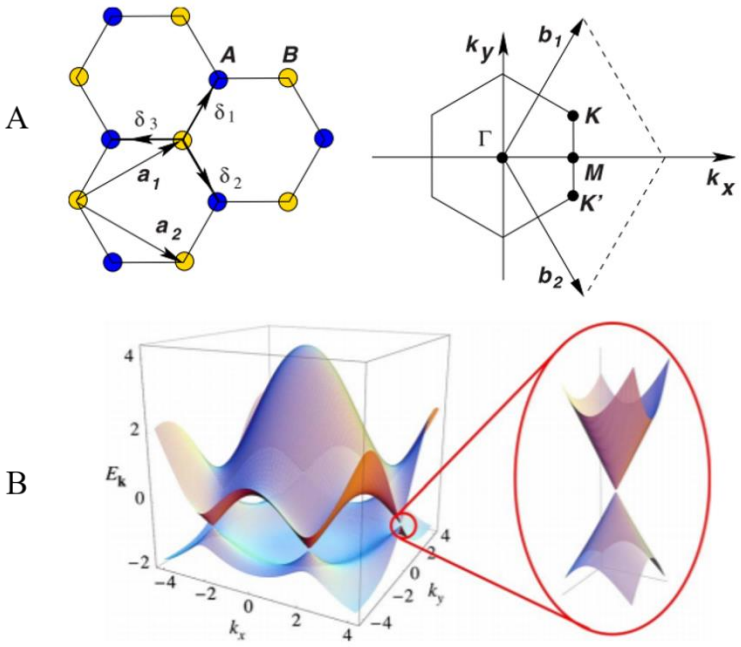

Figure 2.5 Structure of graphene and the peculiar energy spectrum in the honeycomb structure. *In (A) the honeycomb lattice structure of graphene is represented, with the corresponding Brillouin zone on the right, while in (B) the electronic dispersion in the honeycomb lattice is represented, showing the point of contact between the two bands in the honeycomb structure, with a zoom in the point of contact, called Dirac points, showing the typical conical shape of the valence and conduction band of an energy dispersion following the relativistic Dirac equation, associated to charge carrier behaving as massless fermions, leading to ultra-high carrier mobility. (A) and (B) extracted and modified from* [55]

Graphene in particular presents very fast electron transport, one of the highest mechanical strengths and thermal conductivities of known materials, comparable to diamond which of course present the same carbon composition just in a different hybridisation state (sp^2 for graphene, sp^3 for diamond) [56]. The extraordinary electronic properties are a direct consequence of the peculiar band structure of graphene, which has been also defined as a zero band gap semiconductor [57]. In particular, the band structure of graphene shows point of contact between the valence band and the conduction band normally defined as the Dirac point, with charge carriers described as massless fermions following the Dirac equation, with the expected conical shape of the band structure in both bands, called Dirac Cones, **fig 2.5 (B)**. A direct consequence of this configuration is that, in principle, the monolayers have ultra-high carrier mobility and ballistic transport.

After the experimental discovery of the first isolated graphene sheet, led by Andre Geim and Kostya Novosolev [58], several techniques have been used to produce a relatively high quantity of graphene sheets, with three major pathways commonly found in literature:

- Mechanical exfoliation.
- CVD.
- Liquid exfoliation of graphite

In mechanical exfoliation, which is also known as the “Scotch tape” or peel-off method, a graphite or HOPG source is put in contact with adhesive tape which delaminates a certain amount of layers from the source. Successive folding of the adhesive tape decreases the amount of layers remaining on the target part of the tape, till the expected average will be a combination of few layers and monolayer graphene. This technique is the easiest methodology to produce good quality graphene flakes, but of course has great limitations on the control of the actual amount of monolayers produced and the possibility of transferring them to other substrates. Still, this technique has been routinely used in this work to obtain samples from a HOPG reference sample, often referred in literature as freshly cleaved HOPG, to calibrate or check the quality of KPFM tips. Mechanical exfoliation was also used in Chapter 4 to obtain the mono and bilayer distributions of graphene flakes analysed and functionalized with the Raman spectrometer.

In the CVD growth process, carbon atoms are orderly grown on specific metal substrates such as nickel (Ni) and copper (Cu) under high temperatures. The driving mechanism revolves around the affinity of carbon atoms to organize themselves in specific point of the metallic structure, constraining the other atoms trying to occupy the same space to other locations on the metal substrate and forming a perfect monolayer structure [59].

Different initial crystallization areas of the metal substrate will initiate the creation of the monolayer, and each nucleation site will have a specific effect on the orientation of the lattice growing from it. This process will create expanding areas with different lattice orientation that, when getting in contact with each other, create grain boundaries. When all these regions are surrounded by other regions originating from different nucleation sites, the process stops and the regions are referred as domains. This technique produces the largest single sheet areas obtainable, routinely reaching more than 1 cm^2 [60], and much larger dimensions from specific groups and companies. In the work described in Chapter 5, one of such companies, Graphenea®, was employed to successfully deposit a graphene monolayer on top of our sprayed silver nanowires (AgNWs) on glass substrate, which was around 5 cm^2. A professional company was employed due to the difficulty of the transfer procedure, which normally requires clean room condition and specific protocols to be successful in transferring the graphene monolayer with minimal degradation of the monolayer. This aspect represents one of the main limitations of the process, together with all the defects coming from the presence of grain boundaries and the need of very high temperatures for processing which limits its employability in not specifically built facilities.

Finally, in the liquid exfoliation technique, low power sonication of a solution containing graphite and specific solvents like NMP (*N*-methylpyrrolidone) is employed to separate each layer from the other resulting in a solution containing few layers or monolayer graphene as a large population of nanosheets. This type of solvent, of which NMP is normally considered the optimal one [61], works by infiltrating in-between the graphene layers thanks to its high interaction energy, equal or greater than the graphene-graphene interaction energy and by intercalating in the interlayer space, it decrease the intensity of the van der Waals forces between sheets, hence decreasing the amount of energy

necessary to isolate them. Unfortunately, the solvent that allows the process represents also the main drawback of the technique, being a contaminating element for the final dispersion, which due to its high interaction energy may be hard to eliminate without aggressive procedures that may introduce defects on the final material. Still, it represents the easier technique for large-scale production of solutions of 2D nanomaterials, and since the final product is in a liquid solution state, it is easy to use in a variety of deposition techniques. The high quantity easily obtainable makes it also a convenient technique when significant amounts are necessary such as in composites or paints .

Chapter 3
State of the art of the use of the KPFM for characterization of 2D materials

3.1 Overview of the use of KPFM for the characterization of 2D materials

Studies of the effect of different substrates on the electrical behaviour of nanomaterials has been a field of application even before the advent of 2D materials. Studies trying to gather information on the expected behaviour of 1D materials like CNTs based on their work function on different substrates can be found from almost 20 years ago [62], employing solutions that still apply in recent studies. For example, HOPG was already commonly used as a reference sample as it is known that oxygen weakly physisorbs with minimal charge transfer on freshly cleaved, structurally perfect HOPG. This allows the use of HOPG as the perfect reference material as its work function value, 4.65 eV, is well known, but as a substrate it presents some obstacle for the study of 2D and carbon materials as it has been shown to induce hybridization of the π states on adsorbed molecules, altering electronic properties [63]. On the other hand, gold surface is sensitive to gold contaminant and small variation from tabulated results in UHV must be expected. Generally, its work function value tends to decrease over time due to oxygen physisorption, but its high conductivity and well known energy levels made it a primary substrate to study charge transfer between metallic substrates to nanomaterials [64]

The first KPFM study of the properties of graphene was by Filleter et al. in 2008 [65]. In this pivotal study, epitaxially grown graphene was characterized to observe how the work

function was dependent on the number of layers. Respectively to the monolayer work function, the bilayer showed an increase in work function measured at 135±9 meV, showing how the electronic properties of the two types of graphene are measurably different, to the point that in general conditions KPFM can be used as a the best technique to identify areas presenting different thickness of graphene compared to just the topography data in rough samples with very small height differences. This superior detection of the proper height of the step size between the layers in the KPFM method is intrinsic to the working principle of the technique, removing the effect of long distance electrostatic forces affecting the tip while scanning the substrate, which are a source of errors in normal topography measurements. This approach requires accurate modelling of the tip shape and the local field effect, but it has been employed to achieve atomic scale resolution in literature [66].

The work function difference between the monolayer (1LG) and the bilayer (2LG) of graphene is particularly important value to properly measure as it is independent from all the other sources of error coming from tip shape, structure and charge. The absolute values measured on the basal plane of a 1LG or 2LG may vary based on experimental conditions and they are not normally reliable if a direct comparison to other areas of interest of the sample is not available. Another aspect of great importance is that while the absolute value of the difference in work function between 1LG and 2LG is constant, it may appear as a decrease or an increase in the CPD map depending on the type of substrate the graphene is deposited on. In epitaxial grown graphene used for this first study, the starting SiC substrate act as an n-doping source, hence the second layer will be less affected and the work function will increase moving away from the substrate.

Conversely to this, for exfoliated graphene deposited on SiO_2, doping from the substrate is positive and the second layer will appear to have a decrease of work function. Specific

works in the literature demonstrated, using KPFM analyses of the substrate alone, how the SiO_2 is prone to create isolated areas of strong electronegativity that also explains why in defect free graphene the work function map may not appear homogeneous [67]. Further studies showed how this screening effect of the layers is proportional to the number of layers, but not in a linear way [68]. As the number of layer increases, the work function increase or decrease follows an exponential decay that reaches its limit at around 20 layers. Beyond, there is effectively no difference between bulk graphite and few-layer graphene. KPFM has been also used to further characterize the type of electronic interaction that graphene has with a large variety of substrates, to identify the most suitable for electronic applications and to determine what doping effects were more or less effective in changing the band structure of graphene mono and multilayers [69]. The understanding of these properties allowed the exploration of possible ways to functionalize graphene to control its electronic state in FET (field effect transistor) applications. For example with organic molecules [70], KPFM was the technique of choice to check the successful electronic coupling of the dopants with the graphene sheet. Another aspect of FET technology that can only be investigated by KPFM is the study of how functional groups and lattice defects influence the electronic properties in the device itself based on how they are distributed in the connected flake [71]. This study confirmed the potential of high-quality graphene in behaving as a gate material without introducing a noticeable voltage drop between source and drain, as confirmed by KPFM. It also showed how lattice defects like wrinkles, while showing distinctive work function, do not seem to obstruct electron flow significantly even in higher densities.

In ambient conditions, interlayer work function differences tend to be smaller, in the range of the tens of meV per layer [72], with the rate of decrease quickly decaying after 5-6 layers of graphene or up to 10 in insulated conditions with a high resolution tip. The full

range of work function values from the monolayer to the bulk graphite should be around 250 meV [73]. Polar species in the air will be attracted to doped regions in different ways depending on the absolute value of the p- or n-doping of the flakes, effectively acting as a shield to the proper measurement of the CPD. As highlighted in chapter 1, KPFM techniques are mainly divided in two categories, amplitude modulation KPFM (AM-KPFM), where the signal intensity is proportional to the actual force felt by the cantilever, and frequency modulation KPFM (FM-KPFM), where the signal intensity is proportional to the gradient of the force [74]. Graphene samples, particular when analysed in FET applications, may have some advantages in the use of AM-KPFM, which employs lower applied voltage guaranteeing less interaction with the band gap properties of the sample, but is generally analysed with FM-KPFM in recent years due to the major advantage of the superior lateral resolution.

As further expanded in chapter 6, another field of application of KPFM is the analyses of work function changes in the reduction process of GO (graphene oxide) flakes. In this case, KPFM should show a marked increase of the difference from the substrate value when the flake is properly reduced as the electron mobility is increased and the doping effect of the substrate should become accentuated. Compared to the quick re-stacking of graphene flakes in a solution in absence of specific surfactants, monolayers of GO can be stored in large quantities in liquid solvents, thanks to their hydrophilic nature. When necessary, they can be converted back to graphene monolayers with a variety of processes. Still, GO is a harder material to characterize with KPFM as physisorption of water molecules caused by its hydrophilic nature shield the effect of the applied potential [75]. On the opposite of this process, KPFM can also be employed to verify the creation of radical hydroxyl and carbonyl groups and estimate their relative density on the graphene flakes. The expected results would be an increase of work function due to the

electronegativity of these radical groups, with the possibility of locally tuning the work function under specific ion beam irradiation, for example a He^{2+} source [76].

The absence of a well-defined band gap in graphene limits its application in a variety of fields where some ON/OFF conditions between a conductive and a not conductive state are required. In the search for novel 2D materials with semiconducting properties, transition metal dichalcogenides (TMD) have been identify as a promising new family of materials, with Molybdenum disulphide (MoS_2), with a 1.8 eV bandgap, as a notable example that has been widely researched due to its relatively lower reactivity and availability compared to other TMDs [77]. These materials present a characteristic structure formed by a transition metal monoatomic layer from the IV, V or VI group surrounded on top and the bottom from another monoatomic layer of a chalcogen element, as represented in **fig 3.1**.

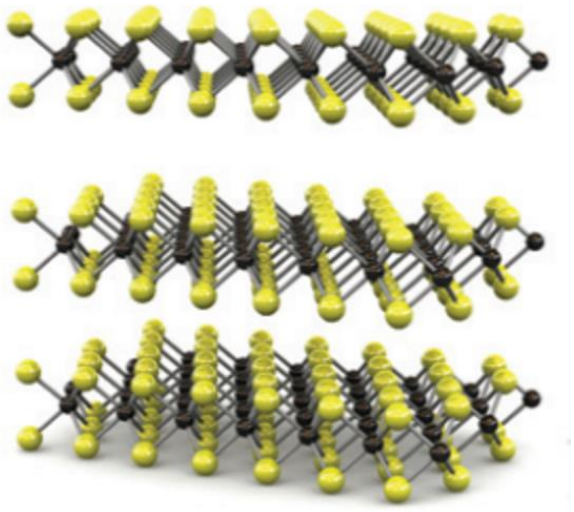

Figure 3.1 Characteristic structure of a TMD*. In black it is represented the transition metal, while the chalcogen is represented in yellow. Taken from* [78]

For this family of materials, KPFM maintains its role of being the best technique to establish the dependence of electronic properties upon morphological features and

number of layers, and similar works to the ones referenced about graphene can be found in the literature. Here I will present some notable example to understand the more peculiar properties of these materials. One of the main limits of KPFM applied to the TMDs is that they tend to be hydrophilic and so the sample tends to quickly adsorb a layer of water molecules which at low temperature will shield the sensing of the electron movements under the applied voltage [75]. The result of this is that the interlayer work function reported in the literature vary depending on substrate, temperature, vacuum conditions and applied potential. Despite this, MoS_2, for example, presents similar behaviour to graphene with the work function changing depending on the number of layers up to a certain height [75], then reaching a plateau that represents the bulk work function after around 8 layers in UHV conditions. Interlayer work function difference has been established as remarkably similar to graphene, in the order of more than 100 meV moving from the first to the second layer.

KPFM proved also an important limitation of MoS_2, the effect of the active sites on the edges and in the lattice defects, grain boundaries or local folding [79]. All of these imperfections behave as sites for the preferential adsorption of other molecules, which will further decrease electron mobility and reduce the performance of the nanomaterial in real life applications. The reactive nature of the MoS_2 edges was further characterized by KPFM in a subsequent study [80]. The results showed that after heat treatment the basal plane work function properly follows the expected monotonic trend from the monolayer value to the bulk value, while the edges instead tend to be relatively unaffected. This aspect is particularly important as also the scale of the layer-to-layer work function is affected, being screened by the molecules attached to edges, hence presenting lower than expected value.

This represents the main obstacle in the use of liquid-exfoliated 2D materials for this type of characterization. As their aspect ratio is significantly smaller than the CVD or mechanically cleaved material, the effect of the edges on the overall measured properties is more pronounced, while at the same having the disadvantage of being processed in a liquid phase which almost surely guarantees the presence of adsorbed molecules at the edges. In CVD studies, the influence of water is reduced thanks to the possibility of averaging the value between a greater number of points in the basal plane, even though the effect still needs to be accounted for [81], as it is more prominent than in other 2D materials like graphene.

3.2 Example of a CPD/height study of liquid exfoliated TMDs

As previously mentioned, one of the most basic applications of KPFM for the characterization of 2D materials is the study of the relationship between the morphological properties of the flakes and their work function.

While this type of characterization represents an important indication of how the electrical properties of all the conductive 2D materials scale based on height and lateral size, it becomes particularly relevant for semi-conducting ones like the TMDs to gain some general insight on the electronic properties of the material in real life application after processing and deposition. While the theoretical and ideal properties of these materials are well established in the literature, during the synthesis, storing and deposition process there is a decrease in the probability of obtaining perfect monolayer materials with the absence of defects or functional groups attaching to the structure. Furthermore, the type of substrate onto which the material is deposited influences these properties, making a

proper characterization at least necessary to confirm that the effect of all these phenomena is within the range of the expected properties observed in other studies.

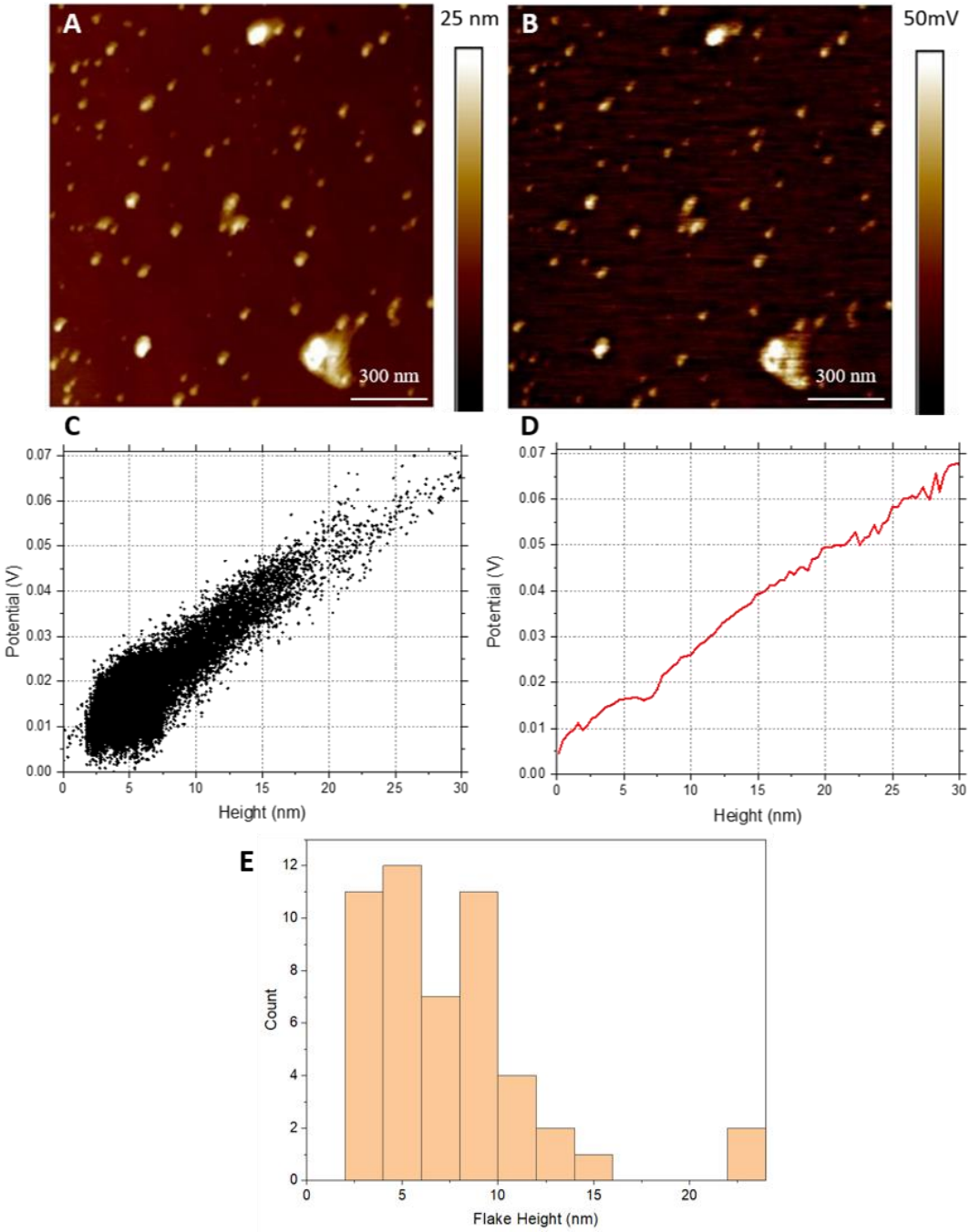

***Figure 3.2 MoS_2 deposition and KPFM characterization for the study of thickness to work function relationship**. In (A) is shown the AFM height data of the deposited material, with (B) representing the respective potential data. In (C) the extracted data is plotted showing immediately the expected upward trend, with (D) showing the averaged trend as a continuous line. In (E) the average flake height distribution is plotted.*

Liquid exfoliation, while making it easy to obtain large quantities of 2D materials in a ready to use dispersion for further deposition or inclusion in composites, may induce changes of properties due to residual surfactant and mechanical stress on the structure during the sonication process.

In this work, a MoS_2 dispersion was deposited on top of a smooth silicon wafer with 10 nm of gold sputtered on top to make it conductive for KPFM characterization and to minimize electrical interaction between substrate and sample. The deposition was by spin coating followed by 1 h in a vacuum oven at a mild 70°C to remove liquid residue; the sample was then left in a desiccator in a closed petri dish for storage. Following this, it was characterized by KPFM, with the resulting height data presented in **fig. 3.2 (A)** and the corresponding CPD data shown in **fig. 3.2 (B)**.

The first thing to notice is that the average flake lateral dimension is very small, which, while being a nuisance for the KPFM by reducing the total number of pixels available for the averaging of the CPD, allows for a better average thickness, with the majority of flakes less than 10 nm tall, as shown in **fig. 3.2 (E)**. The pixel-by-pixel data was then extracted from the image, operating some standard flattening procedure to the height data while the CPD data was just offset by the average value of the background, which represents the average CPD between tip and gold substrate. In a flattening procedure, an area of the substrate without flakes is selected, the average plane angle is calculated and then subtracted from the complete data to obtain a background as flat as possible.

The data was then plotted first as a scatter plot to observe the general distribution of points, **fig. 3.2 (C)**- Subsequently, the data was divided in smaller height intevals and for each of them the average voltage was calculated, hence obtaining the CPD/height relationship, **fig 3.2 (D)**. The rate of increase observed is much lower than one would

expect from the literature [82], but considering the small size and the effect of averaging due to the effect of surrounding substrate, it can still be justified.

Also, as explained in the previous section, smaller flakes of TMDs have been reported to have lower contrast with their surrounding as the edges presents molybdenum or sulphur atoms that tend to interact with water molecules strongly, obstructing the detection of the proper work function [79]. This is particularly interesting because it shows that by averaging a large amount of points, instead of relying on standard line section observation, it is possible to establish general properties from liquid-exfoliated material from processes that are not operated in a clean room or in a vacuum system. Of course a limit of the technique is that the averaging compromise reliability at a greater height due to the reduced number of pixels used and because KPFM, as a technique, is susceptible to artefacts coming from sudden increase or decrease of height, due to the tip sensing not only the effect of the point immediately underneath it but also the effect of the lateral edges of the higher elements.

This analysis was repeated with a different TMD, $MoSe_2$, which presented a more difficult morphology to characterize due to higher features than MoS_2, as visible in the AFM height picture in **fig. 3.3 (A)**, but also larger flakes with well distributed height which allowed a reduction of averaging artefacts. The deposition process, thermal treatment in the vacuum oven and storage followed the same procedure used for MoS_2.

The potential map showed a very strong signature from the higher features, **fig. 3.3 (B)**, but interestingly, once plotted with the same procedure described before, the CPD/height data for the first few nanometres was remarkably constant, as shown in **fig. 3.3 (C)**. This time, values were closer to the ones expected for this layered material, with full range from monolayer to almost bulk like in the range of hundreds of meV.

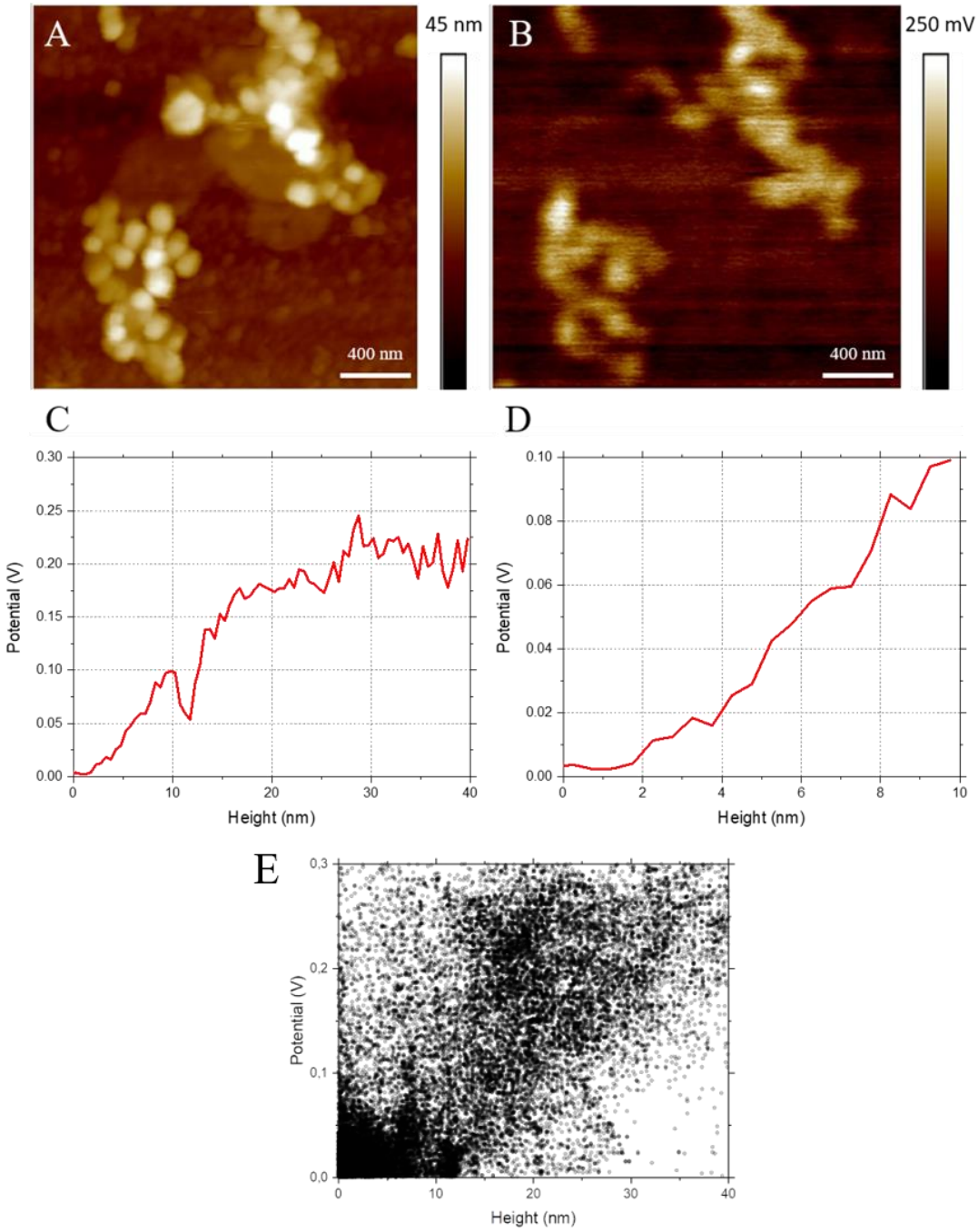

Figure 3.3 $MoSe_2$ deposition and KPFM characterization for the study of thickness to work function relationship*. In (A) is shown the AFM height data of the deposited material, with (B) representing the respective potential data. Compared to the MoS_2 dispersion, this material shows higher aggregation and strength of the overall signal. In (C) the extracted data is plotted showing a clear baseline for the substrate and the upward trend, confirmed at different averaging window showed here in different colours, with (D) showing an enhanced visualization of the first 10 nm. In (E) the starting raw data has been plotted as a scatter plot.*

In **fig. 3.3 (D)**, we can observe a zoom-in on the first 10 nm, showing an average of 10 mV/nm, which is an order of magnitude higher than that observed with the same approach for MoS_2. Considering that $MoSe_2$ has been known to have higher intrinsic conductivity with lower conduction band minimum than MoS_2 [83], electrical contact with the substrate was probably better and overall, considering the bigger dimensions of the aggregated flakes, the number of points in plane was larger, allowing for better averaging, as shown by the high density of point in the original scatter plot in **fig. 3.3 (E)**.

In conclusion, this work, while being just the starting point of my work with KPFM related analyses, represented an interesting first in showing how we can obtain good quality data for TMDs even while working with liquid-exfoliated materials in air conditions. The expected problems of liquid-exfoliated depositions, in this case in particular small flake size and high amount of strongly bonded residue, were immediately visible on the KPFM data for the MoS_2 sample. Still, the data showed the expected increase in workfunction associated with the increased number of layers, with a remarkably constant increase rate. The same approach used for a similar but electrically different TMD, $MoSe_2$, showed a much higher increase rate thanks to bigger dimension of the flakes and possibly better electrical contact with the substrate, with a well-defined linear trend in the first 10 layers and the expected plateau associated with the nanomaterial reaching the bulk properties for higher thickness.

Chapter 4
Laser Based Texturing of Graphene to locally tune Electrical Potential and Surface Chemistry

4.1 Introduction

The possibility of exploiting the extraordinary properties of graphene in the field of mechanics [84], electronics [85], [86], photonics [87] and in general in almost all the disciplines of science and technology [56], [58], [88] has generated extensive interest in recent years. One of the key challenges is the necessity of tuning the relevant properties of graphene by controlling the shape, dimensions [87], [89] and substrate interactions [86] while at the same time developing way to obtain controlled functionalisation [90], [91]. In particular, inducing controlled and optimised strain in graphene to module electric properties has become a field of its own called “straintronics” [92]. The application of tensile force by bending [93] and stretching [87], [94], [95] the graphene layered structure or the mounting over textured surfaces [96] are some of the common practices used to introduce localized strain in 2D materials. These types of procedures have produced emerging properties such as: pseudo-magnetic fields as high as 300 T and the opening of a band gap in the electronic band structure when non-uniform strain is applied [97], [98] or the enhancement of the electron-phonon coupling when biaxial strain is applied [99], theoretically turning graphene into a superconductor.

One of the techniques employed for patterning and texturing graphene is through laser irradiation, which represents maybe the most efficient way to strain and alter electrical and mechanical properties [100]–[102]. In particular, a controlled laser treatment can

induce subtle chemical and structural changes in graphene, which results in the tailoring of the bandgap, lattice expansion, functionalization and patterning of the surface for electronics applications [101]. Laser treatments employed in previous studies include continuous wave [103], nanosecond [104]–[106] and femtosecond lasers [107]. In more recent studies, complex and stable 3D structures of CVD graphene have been produced by tuning the irradiation dose to modify electrical and optical properties [107], [108], but the employed lasers are high energy and not in the range of visible light [102], which would be the desirable option to minimize the destructive effects of the irradiation and at the same time to decrease the lateral dimension of the modified areas thanks to the lower density of energy involved. Raman spectroscopy has been widely employed as a sensitive and non-destructive laboratory tool to characterize the chemical, mechanical and electronic properties of graphene through the analysis of carbon-carbon bonds vibrations [43], [109], [110].

Raman spectroscopy is based on the vibrational transition of molecules occurring in the ground electronic state; and in particular, employing the visible range of light to induce variations in the phonon frequencies [111]. Compared to the high emission lasers employed to modify the graphene surface in the studies cited previously, Raman requires very low power and has not been usually employed as a possible solution for localised modifications of the structure, even though longer exposure can produce similar effects. Finding the optimal trade-off between the most resonant frequency and the minimization of energy delivered to the sample is necessary to preserve the sample, since prolonged exposure to laser excitation energy of 2.33 eV (532nm wavelength) and 1.87 eV (660 nm wavelength) when the focal area is a few μm^2 can result in unwanted modification of the sample [112]. As an example, low molecular weight polymers may change drastically their structure and photochemical/photophysical properties long before reaching their

glass transition temperature. Also, it is possible to induce local adsorption of species from the environment through a catalysis process [112], [113]. While these processes may appear to be problematic for the purpose of characterization, they may be exploited to modulate desirable electrical properties in conjugated polymers by establishing planar conformations and higher conjugation length [114].

In a recent paper, a blister was induced in graphene when irradiated by a 532 nm wavelength laser, due to local gaseous pressure generated by the sublimation of weakly chemisorbed chlorine trifluoride (ClF_3) intercalated between substrate and graphene, with the resulting pressure on graphene estimated as high as 22.9 MPa and the consequent creation of the 3D structure, which apparently was reversible when irradiation was switched off [115]. Other examples of 3D structure creation induced by Raman excitation have been described in literature in graphene/silica systems when irradiated with 40 mW for up to 2000 seconds, with a specific pattern obtained with desired mechanical and chemical changes [102]. Still, even though widely employed for characterization of graphene quality, rarely this type of modification have been reported and characterized.

In this study, Raman lasers at different wavelength (532 nm and 660 nm) and different fluence ($mJ/\mu m^2$) have been used on mechanically exfoliated graphene on silica, with AFM characterization used to verify the specific surface area affected under laser irradiation. A lower dose of laser energy (2.5-3.7 $mJ/\mu m^2$), routinely used for Raman characterization, has been used to identify areas of monolayer graphene, while the modifications occur at higher doses (511-753 $mJ/\mu m^2$). Irradiation of different regions of single and bi-layer graphene in air has been performed in order to observe, characterise and understand the structures formed using this approach. The 3D structure produced shows distinctive morphology, adhesion force and local surface potential compared to un-treated graphene crystal under AFM and KPFM analysis.

The theorized origin of this structure is a combination of expansion of carbon-carbon bonds and presence of trapped molecules. Also, observed is a degree of partial oxidation of the graphene blisters verified by Raman spectroscopy and FTIR data, presented in section 4.5 of this chapter. The areas affected by the laser irradiation were analysed with Raman mapping as a function of displacement to obtain sufficient amount of data points to calculate defect density (n_d). In summary, power tuning of the radiation source to obtain different features and the possibility of obtaining pre-programmed patterns of altered electrical and mechanical graphene spots are established as possible with the Raman spectrometer.

Single and bi-layer graphene was produced by mechanical exfoliation of graphite (HOPG), deposited on a silica substrate (300 nm oxide thickness), then cleaned in an ultrasonic bath with isopropanol and deionized water each for 30 minutes followed by heating in vacuum oven for 3 hours at 200^{o}C.

Raman spectroscopy (spectral resolution 0.3 cm^{-1}) has been carried out at 100X objective lens using two lasers, first with 532 nm (type: solid state, model: RL53250), and second with 660 nm (type solid state, model: RL660C100), at different powers (mW). The maximum power used from the laser source for 532 nm is 50 mW and for 660 nm is 100 mW, switched through the use of ND filters, with the higher power density of the laser achieved by increasing the time duration (10 s, 15s and 20s) of the irradiation while keeping the output power consistent. The laser irradiation was repeated over four different single layer graphene flakes of reproducible textured amplitudes.

AFM characterisation was performed with a Bruker ® Dimension Icon, positioned in an insulated box over an anti-vibrant stage to minimize environmental noise and building vibrations. Contact potential difference (CPD, volts) and mechanical data was measured

from advanced operation mode of PF-KPFM (PeakForce-Kelvin Probe Force Microscopy) and PF-QNM (Peak Force-Quantitative nanomechanical) respectively. Peak Force is a Bruker's proprietary mode which allows the collection of both types of information on a single acquisition: amid the PF-KPFM operation, the standard PeakForce procedure is operated in the first pass of each line scanning, with the tip softly (<1nN) tapping on top of the sample, gathering topography and mechanical properties of the sample. In the second pass over the same scanning line, the cantilever is lifted from the surface up to 10 nm distance to collect CPD data. The proprietary Scanasyst® algorithms simplify engaging and parameters setting procedures, optimizing in real time Scan Rate, PeakForce set point and Feedback Gain settings, but was in general turned off during capture once the optimal parameters were achieved to avoid inconsistency in the final picture. This type of characterization has been performed using every time the same mounted tip to guarantee as much consistency as possible in the Kelvin Probe data. A PFQNE-AL tip was chosen for these reasons, being the gold standard of Bruker's tip for KPFM characterization: it is a soft silicon-nitride tip with 5nm nominal tip diameter, 300 ±100 kHz resonant frequency and 0.8±0.2 N/m spring constant, optimized for electrical modes and with a proprietary reflective coating on the backside.

Thermal Tune calibration was performed before each imaging session to verify consistency of resonance frequency and stiffness of the cantilever. High-resolution mechanical information was acquired by PeakForce-QNM (Quantitative Nanomechanical Mapping). This mode works with the same procedure described in the first pass of the PF-KPFM, but a silicon nitride tip (Model: Scanasyst-air) was chosen in these cases, having a nominal ultra-sharp tip of 2-3 nm that allows maximum resolution while minimizing contact area of contact, ensuring better consistency and resolution of mechanical information, in particular adhesion force map. The resonance frequency and

the stiffness of the cantilever were measured as 70±25 kHz and 0.2 N/m to 0.8 N/m (nominal 0.4 N/m) respectively. The adhesion force measurement carried out in PF-QNM approach was operated in a true contact mode at relative humidity (30-35%) at room temperature, modest pressing was applied to avoid collapse of the membrane due to large contact deformation [116].

The FT-IR measurements were performed using PerkinElmer Spotlight 400 FT-IR Microscope System, used in dual mode single point and MCT array (mercury cadmium telluride) detector standard with InGaAs array option for optimised NIR imaging, and all the measurements were done using the mid-IR (4000-500 cm^{-1}).

4.2 Morphology and local surface potential of blisters and graphene nanobubbles

As previously stated, a Raman laser has been used for characterization (number of layers, oxidation, strain) and fabrication of 3D graphene blisters by changing the laser fluence. The lowest power range, 2.55 $mJ/\mu m^2$, was employed from the very start to identify monolayer areas, while two higher energy levels, 511 $mJ/\mu m^2$ and 753 $mJ/\mu m^2$, were used for the creation of the structures, which were then compared to study the effect of the intensity of irradiation in the resulting blister. Mechanically exfoliated graphene was the main test sample, comprised of both single layers (1LG) and bi-layers (2LG) deposited on a silicon substrate with 300 nm of thermal oxide on top, as shown in **fig. 4.1 (a)**. The selected region is crucial to investigate the significance of sub-surfaces, i.e. a single layer of graphene beneath 2LG and silica substrate under 1LG, and under irradiation of the lower power density (511 $mJ/\mu m^2$), arrays of (12 x10) of 3D blisters of graphene are produced on 1LG only, while the area of 2LG was unaffected, **fig. 4.1 (b)**.

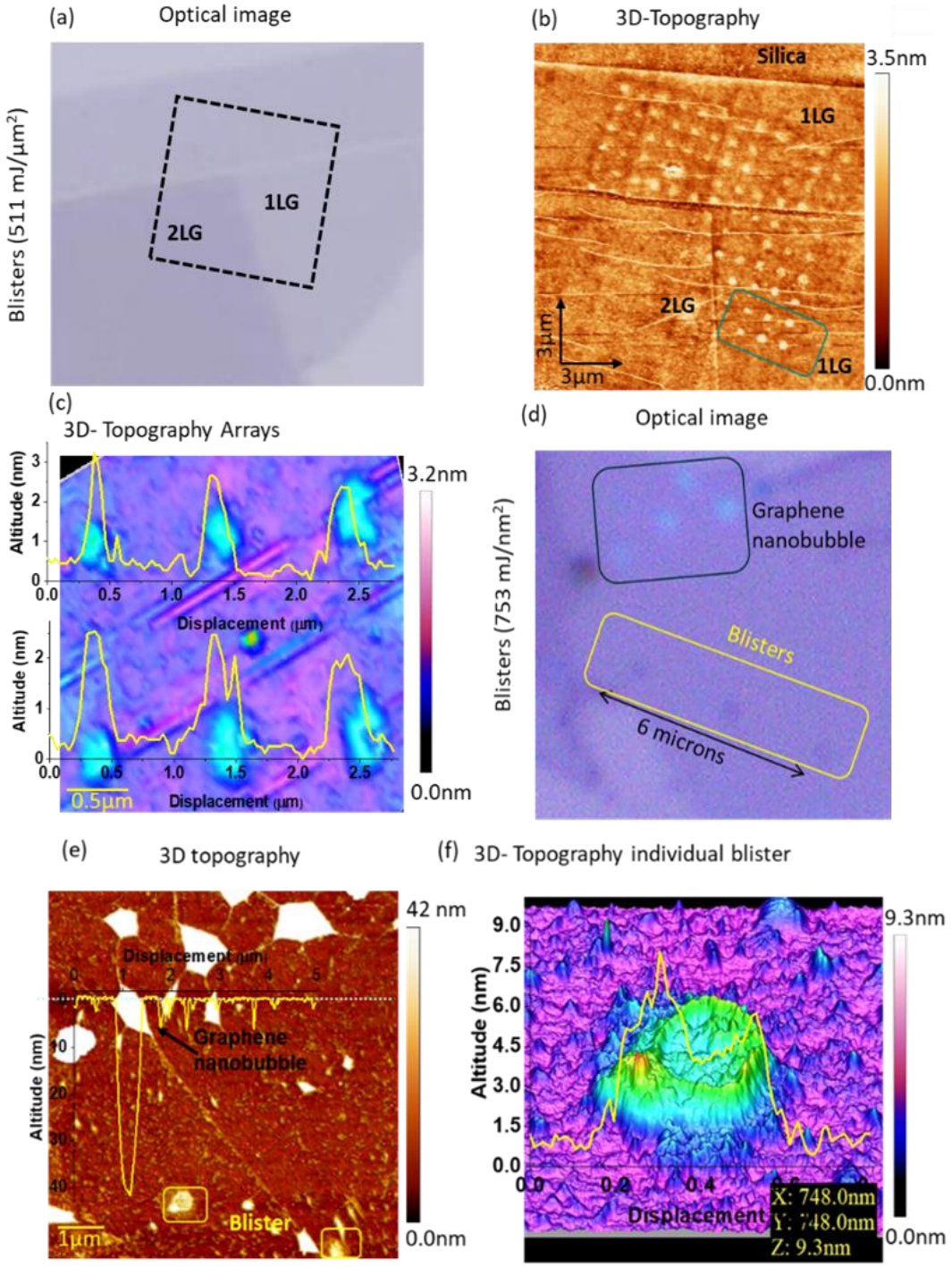

Figure 4.1 Area Selection and Blister formation. *(a) Optical microscope image (100X) of mechanically exfoliated graphene on silica before laser irradiation, with 1LG and 2LG graphene of area 20x20 μm². The dotted square identifies the area of interest to characterise further the laser-induced 3-D structure. (b) AFM topography is showing an array of graphene blisters only on 1LG at power density of 511 mJ/μm². (c) High-resolution topography image of the blisters altitude up to 2.5 ± 0.5 nm, inset line profile shows consistency in the altitude of produced blisters. (d) Optical image of the 1LG (different from panel (a)) after Raman laser treatment (753 mJ/μm²) produced three blisters separated by 2 microns as marked by a yellow color rectangle. There are randomly generated graphene nanobubbles (referred as "Nb") near the edge of the 1LG marked by a black rectangle. (e, f) 3-D topography of graphene nanobubble 40 ± 2 nm and laser-induced blisters of altitude 6±1.5 nm respectively.*

This exemplifies the vital role of interlayer coupling in 2LG in distributing the laser-induced thermal energy by introducing new vibrational modes in the structure that help the dispersion of the energy [117], avoiding the local heat density necessary for the generation of the structure. Another factor is the higher resilience of 1LG on silica due to higher shear strength [118], hence being less capable of efficiently distributing the heat energy. The amorphous nature and lower thermal conductivity of the silica layer on top of the silicon substrate (1 W/mK) also effectively shields the graphene from substrate induced heating in standard short-term irradiation, but in long exposure conditions like the one present in this study instead further heating is introduced, leading to short-range distortions and buckling of the graphene layer [102], [119]. The surface chemistry and properties of such obtained blisters are different from the ones from natural 3D formations that are present in the monolayer graphene, caused by imperfections inherent of the production process.

For example, in **fig. 4.2 (a)** we can distinguish in the adhesion force map the blisters induced by Raman from some nanobubbles in the top left, generally caused by trapped molecules between the substrate and the graphene during the deposition process. We can also observe other characteristic features of the basal plane like wrinkles and ripples, which appear as linear structures organized along strain lines residual from the synthesis and deposition processes. These structures are unavoidable when producing graphene, but are also of great importance as a reference point for comparison of different characteristics and functionalization of the basal plane.

The adhesion force map was chosen because it is correlated to the interaction of the AFM silicon tip apex with the substrate, probing the elastic penetration at a defined force set point and measured while the tip is moving away from the substrate during the tapping process. Hence, the adhesion force is linked to the extension of the contact area and the

structures on top of the graphene layer. For both nanobubbles and blisters we observe that the tip adhesion is higher in the central area compared to the edges. This is well established in literature and it happens because the central area behaves like a membrane with nothing rigid underneath, then being susceptible to deformation under the tip apex as force is applied, increasing the effective area of the interface between tip apex and substrate. As a consequence, the adhesion force measured as the tip pulls away from the surface is increased [118]. While this approach has been employed in the past to make consideration on the membrane mechanics as a function of the volume, in this work it has just been employed to justify the data from the blisters, as the structures have very different dimensions and hence probably also different mechanical behaviour.

Examples of the mechanical data that is obtained during the first pass of a KPFM analysis is present in **fig 4.2 (e)**. A higher resolution image (inset **fig. 4.2 (a)**) of the adhesion force map of the blister shows that also the shape of the area is different, the blisters having a very clear spherical shape, while nanobubbles are more polygonal, interlinked by wrinkle structures. This spherical structure would indicate that this blisters stem not from pre-existing features in the graphene basal plane, but that they arise just from the laser excitation. The surface potential mapping produced by KPFM shows the same ring structure with a very distinct CPD signal coming from the blister, **fig. 4.2 (b)**, with a 25-30% decrease in the observed value at the centre of the blister compared to the basal plane. This decrease is similar to what can be seen in the wrinkles, where the basal plane has increased distance from the substrate, removing the standard p-doping induced by silica on graphene, as extensively established in literature [108], [120]. A possible explanation also of the inner and outer ring CPD difference may also suggest local oxidation of graphene [102], since nanobubbles for example appear with a more evenly distributed value as can be observed in **fig. 4.2 (c)**.

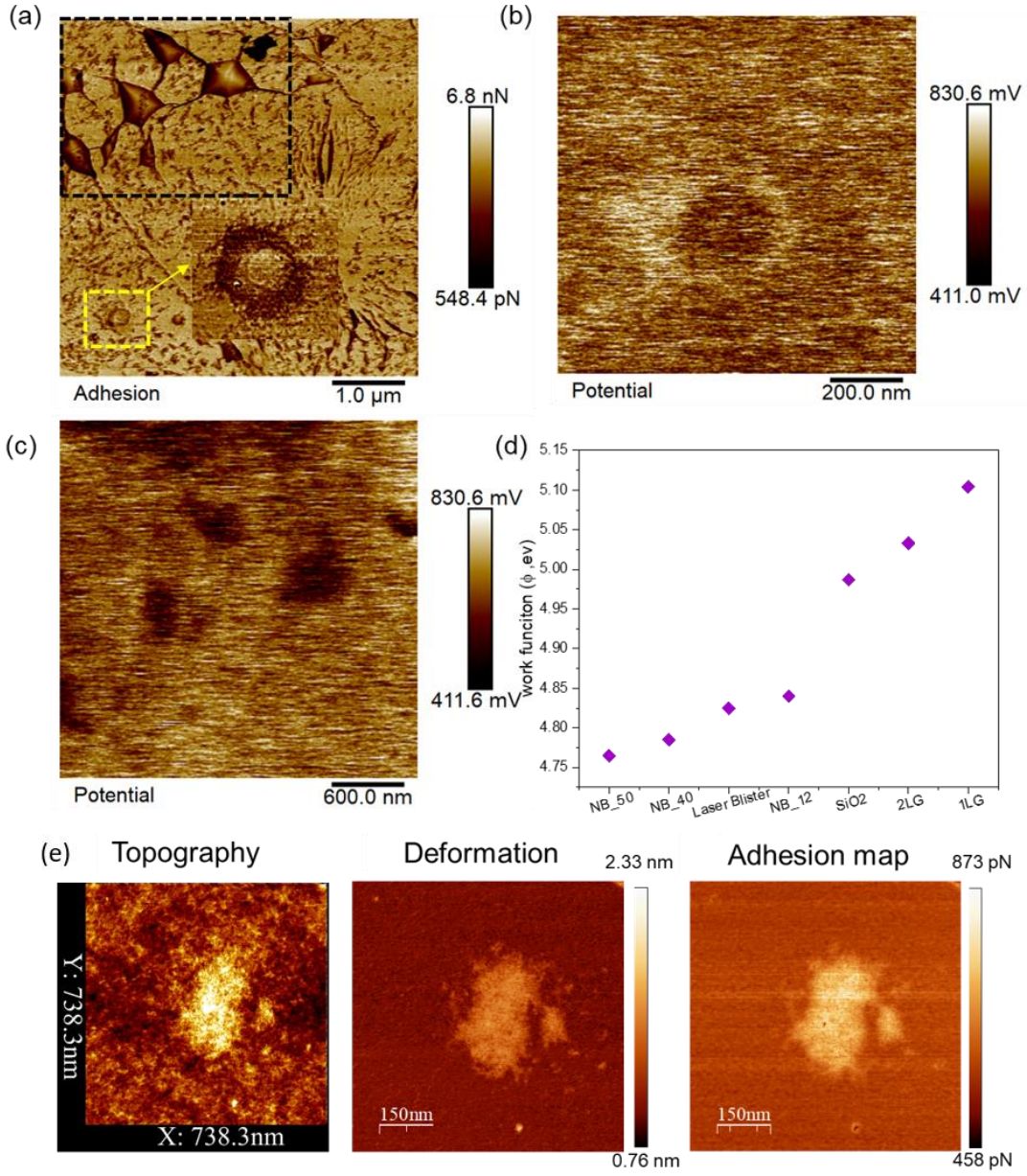

Figure 4.2 Adhesion force map and local surface potential characterization for graphene blisters. *(a) Adhesion force map (measured by pull-out force) contrast distinguishes 1LG graphene into graphene nanobubble, blisters, ripple and wrinkles. (b)The CPD (contact potential difference, mV) value of an individual blister showing peculiar local surface potential with respect to 1LG and the nanobubbles (from panel c) by introducing a ring around inflated graphene with distinct CPD values (c) The CPD map of the graphene nanobubble varying with their altitude i.e. gap from the SiO_2 substrate. The CPD values is highest for the basal plain graphene supported silica. (d) The work function (eV) measured from the CPD for different regions shows highest value for 1LG graphene and lowest for the graphene nanobubble of altitude 50nm. The trend is showing the substrate gap distance plays an important role in influencing local surface potential (e) high resolution images of the height and mechanical data that can be obtained in the first pass.*

A summary of the work function values for different regions is given in **fig. 4.2 (d)**, consolidating previous observation about the influence of the distance between the probed graphene surface and the silica substrate. The reported work function values for the 1LG, measured at 5 eV, and for 2LG, measured at 4.8 eV, in standard condition at 33% relative humidity are coherent with previous literature findings [68], [121]. Whatever the substrate, the lowering of work function in 2LG is generally explained by the screening of the charges, holes in this case, originated by the first layer in contact with the underlying SiO_2 substrate [121]. For the blisters, the work function values were averaged by using just the central area of the ring structure.

In **fig. 4.3**, an example of this controlled patterning is shown, with the mapping tool of the Raman software used to obtain an ordered sequence of well-defined blister spelling US (University of Sussex).

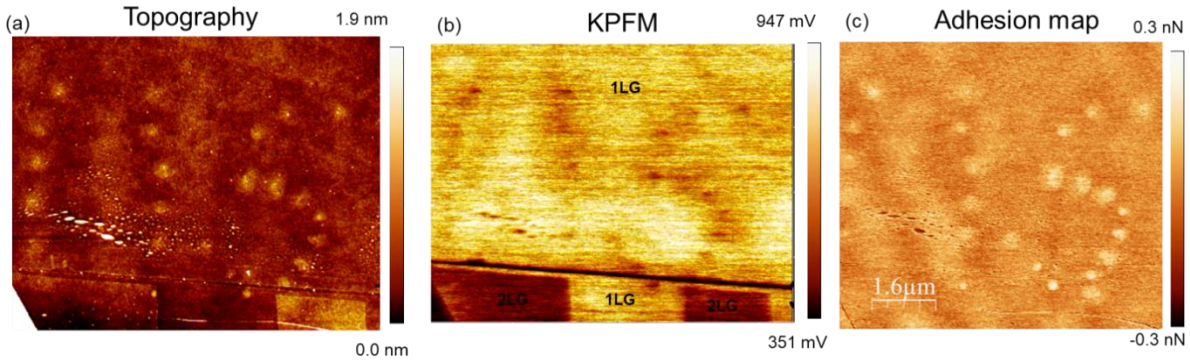

Figure 4.3 Laser writing induced Tuning of graphene *3D blister patterned to spell US (University of Sussex), showing the versatility of the process*

4.3 The influence of laser power density

The three main factors controlling the fabrication of the graphene blisters are:

- Carbon lattice expansion of 1LG [107], [122].
- Presence of trapped molecules at the 1LG – hydrophilic silica interface [115].
- Oxidation of the irradiated carbon atoms in air conditions [108].

The first aspect is monitored by investigating the G and 2D peaks at the two different laser sources chosen (λ =532 nm and λ = 660 nm) as shown in **fig. 4.4 (a, b)**. There is an observed broadening of the G and 2D peaks when power density, and hence local temperature [123], is increased, indicating an increase in overall structural disorder and the introduction of oxygen functional group in air condition, or the creation of a localised area of hole doping by oxygen molecules due to the thermal perturbation of the entire sample, as previously similarly observed in literature [91]. The central frequency of the G and 2D peaks depends on the change of charge density either by electrical, chemical or thermal treatments due to the effect on bond lengths and non-adiabatic electron-phonon coupling [111], [124].

The G band (around 1589 cm^{-1}) relates to the doubly generated phonon mode (E_{2g} symmetry) at the Brillouin zone centre, due to first order Raman scattering process in graphene [43], and it is extremely sensitive to changes in the oscillation strength of electron-phonon interaction near the Fermi level [125]. Normally, the phonon frequency in the G-band range is not affected by the energy densities associated with a Raman spectroscopy measurement [126], nevertheless prolonged exposure at high laser power might still cause structural changes simply due to heating that may alter the Raman spectra suggesting the higher level of disorder in the carbon lattice. The dispersion rate

(ΔG_{pos}/change in excitation laser) increases with disorder [127], which for the structure means generation of local sp^2 and sp^3 domains in graphene [128].

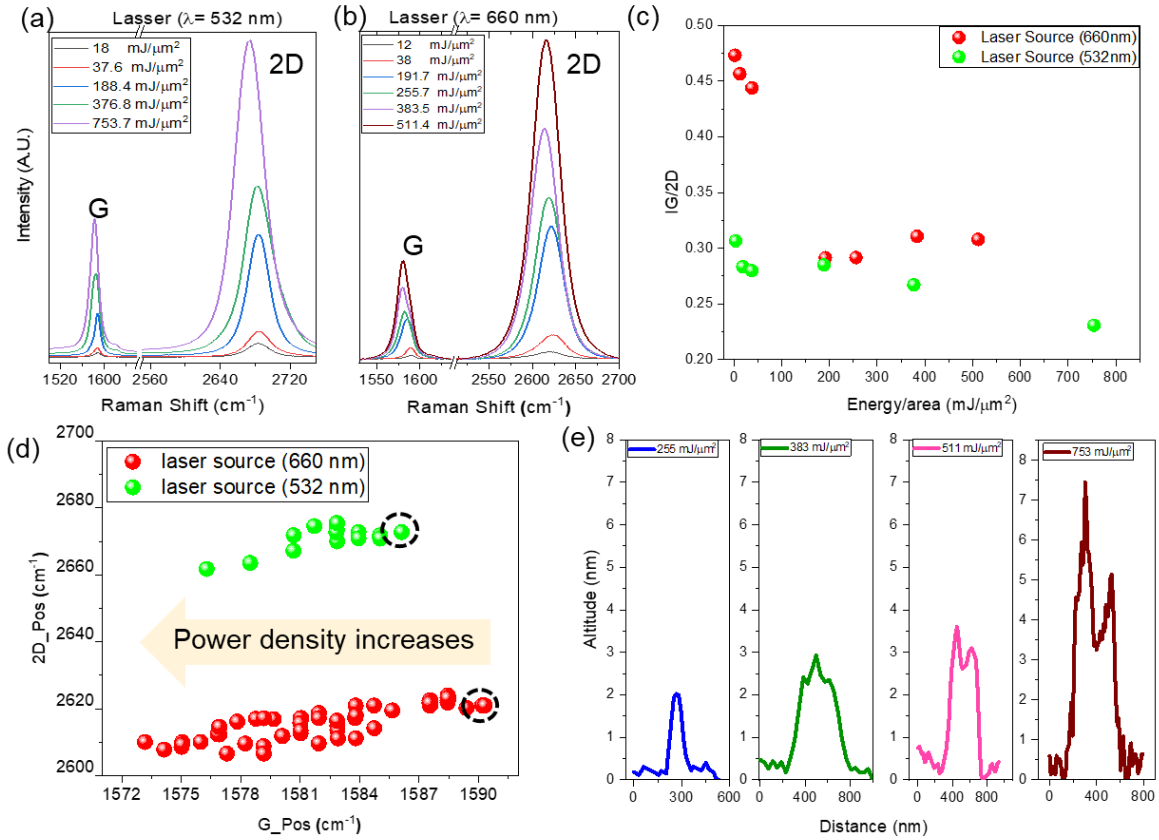

Figure 4.4 Stretching of graphene during irradiation. *(a) Raman spectrum of 1LG for lasers λ = 532 nm and (b) λ = 660 nm at different power densities are showing broadening of peaks (G and 2D) and a red-shift with increasing power density. (c) The sp^2 domain of the graphene is systematically reduced for higher power density for both laser source as illustrated by decreasing intensity ratio IG/I2D. (d) Red shift in G and 2D peak positions, the slope produced by linear fit are S_g= 1.9 and S_r = 1.1 for different laser sources. Inset arrow is showing the direction of increasing power density. (e) AFM topographic profile of the blisters at different power densities showing an increase in volume.*

The excitation energy (E_L) increases the band gap (E_g) energy in graphene, thus enhancing the Raman scattering signal thanks to increased resonance range in the optical absorption [43], [128]. Other reports in the past have also already established the possible effect of laser irradiation in decreasing sp^2 C=C bonds while at the same time increasing the C-C bonds in the deformed graphene plane to accommodate the stretching necessary for the

creation of 3D structures [107], [108]. A decrease in the IG/I2D ratio was observed at higher power density, **fig 4.4 (c)**, suggesting an alteration in the hybrid state of sp^2 carbon atoms up to 50% at the highest power density as compared to un-irradiated graphene. In **fig 4.4 (d),** we can observe also the upshift of the 2D peak position from the excitation at 532 nm compared to the excitation at 660 nm. The 2D peak originates by a second order process involving two iTO phonons at the Dirac point (K), which are affected by the increase in energy during the Raman process, since phonons farther from the K point are required for momentum conservation which causes significant dispersion [126], [129].

The slope (S) we can measure from these distribution, obtained with a linear fit, are S_g = 1.9 for 532 nm and S_r = 1.1 for 660 nm, indicating higher and notable biaxial strain for 532 nm [130]. In the literature much higher values have been observed for the value of S, like 2.45 [95], 2.63 [94] and a theoretical value of 2.25 [40] for biaxially strained graphene over hollow silica substrate in pressurized conditions. In particular, for this last case the expansion of the carbon lattice caused by our laser process is much lower compared to pressurized condition which is verified also by observing the height of our blister structures, **fig. 4.4 (e)**, which have a max height achieved at 6±1.5 nm at the highest energy density (753mJ/μm^2), an order of magnitude lower than what has been experimentally reported in pressurized blisters [131].

4.4 The role of trapped molecules between graphene-silica interface and functionalization of graphene

Specific studies in the past have demonstrated that graphene is impermeable to most gases [132], thus trapped gas molecules at the substrate-monolayer interface can locally produce enough pressure to induce the creation of 3D structures [131]. The role of trapped molecules to generate pressure and inflate graphene blister under laser irradiation was estimated by a geometrical approximation using topographical information (height (*h*) and width (*w = 2r*) , where *r* is its radius) to evaluate internal pressure *P* of the graphene nanobubbles and blisters by assuming spherical or cuboidal geometry. In particular, the force equilibrium imposes:

$$P\pi r^2 = 2\pi r t\sigma \text{ (spherical)} \tag{4.1}$$

Or

$$Pw^2 = 4wt\sigma \text{ (cuboidal)} \tag{4.2}$$

Where *t* is the graphene thickness (*t*=0.35 nm) and σ is its normal stress, and considering *E* Young's modulus of graphene (*E* around 1TPa) and that

$$\varepsilon = \frac{\Delta r}{r} = \frac{2h}{w} \tag{4.3}$$

We derive:

$$P = \frac{4Et\varepsilon}{w} \tag{4.4}$$

The geometry, stress, strain and pressure inside the blisters or nanobubbles are reported in table 4.1; the pressure is significantly lower in graphene blisters with respect to nanobubbles.

width (w)	Height (h)	strain (ε)	Pressure (P)
Nm	nm		MPa
Graphene Blister			
156	1.87	0.024	215.15
498	2.75	0.011	31.08
484	3.40	0.014	40.64
506	6.54	0.026	71.52
Graphene nano bubble (reference)			
175	15	0.171	1371.43
202	16	0.158	1097.93
431	23	0.107	346.68
542	46	0.170	438.45
620	50	0.161	364.20
646	40	0.124	268.38
700	38	0.109	217.14

Table 4.1: Geometry, strain and pressure evaluations of the graphene blisters and graphene nanobubbles (E=1 TPa; the stress could be estimated as $\sigma = E\varepsilon$).

To further test the mechanical properties, the blisters were evaluated by pressing with the AFM tip in a range of normal forces ranging from 0.250 nN to 10 nN, successfully reducing the altitude from the few nanometres previously declared to less than 1 nm after the 10 nN step. Still, the original height compared to the silica substrate is supposed to be around 0.5 nm, showing that residual molecules underneath the blister have accumulated, contributing, together with permanent lattice changes, to the irreversibility of the process, **fig. 4.5 (a-c)**. Extreme irradiation can also lead to ablation of graphene carbon atoms and the underlying substrate [133], with a threshold damage limit established at > 300GW/cm^2 of power density [134], with disruption of the sp^2 carbon bonds initiating at 14-66 mJ/cm^2 [135].

In this work, power density was too low to induce ablation but interestingly a wide area, up to 1.8 μm, of distorted graphene is observed around the blister, **fig 4.5 (d)**, with R_i

defined as the total radius of the perturbed area can be as much as three times larger than R_h defined as the radius of the blister, **fig 4.5 (e)**.

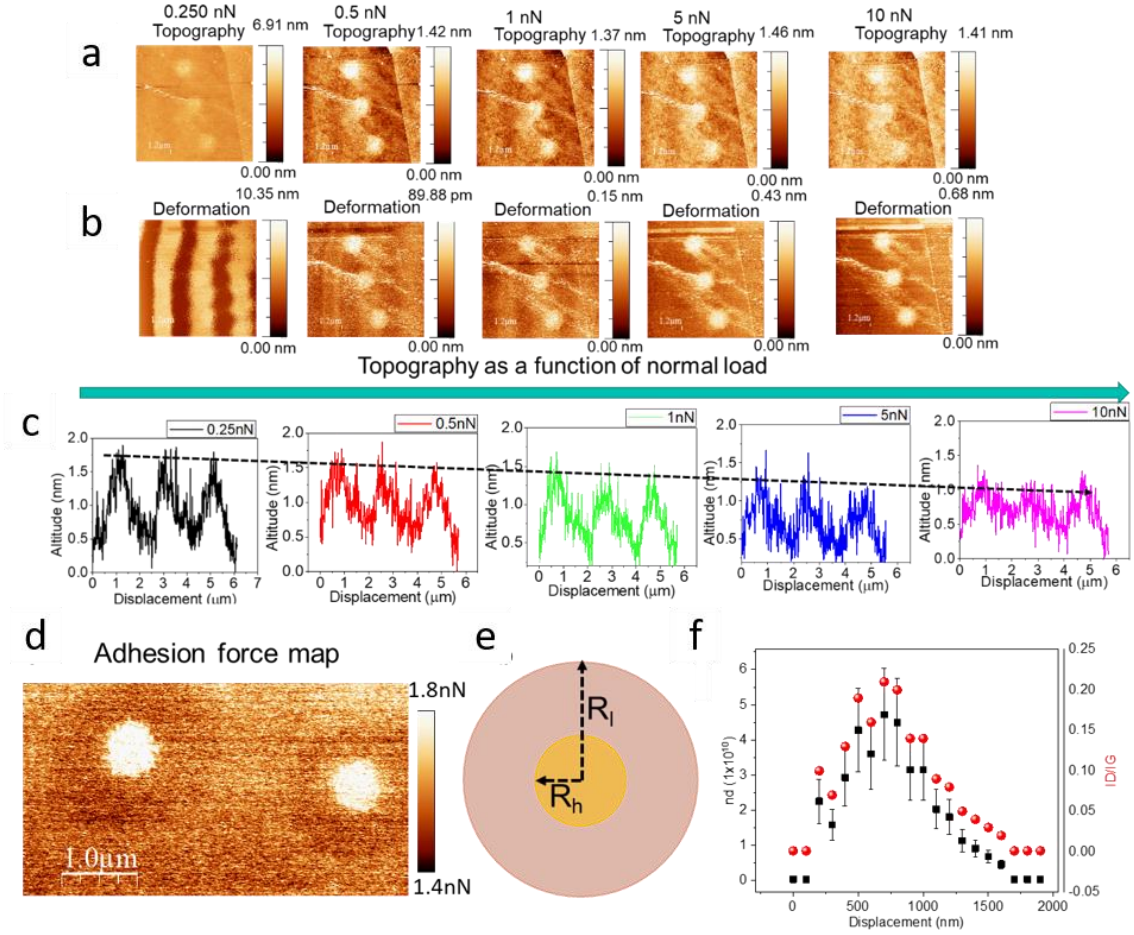

Figure 4.5 Affected area of the blister*. (a) Topography of the same series of blister while increase normal force (b) and corresponding tip deformation on top of the structure (c) linear trend of the decrease in height. Area affected by laser power density (0.511 mJ/μm^2) shown by (d) adhesion force map. The bright regions represent the higher values of adhesion force between the tip apex and the surface. (e) Schematic image of the disordered region at two different radii R_h and R_i represent inner and outer circles respectively. (f) The density of defects (n_d, 1/cm^2) and I_D/I_G ratio as a function of displacement.*

This modification resembles previous theorized models of activated D-band scattering in the Raman spectrum of the graphene sheet by point-like defects [136], that describes the generation of circular areas under ions implantation, where lattice structure is preserved even though D-band is activated. This was monitored by Raman spectra over the region of interest at very low intensity, with I_D/I_G values with higher values at the centre of the

structure, **fig 4.5 (f)**, indicating the increase of point like defects on the structure or symmetry breaking.

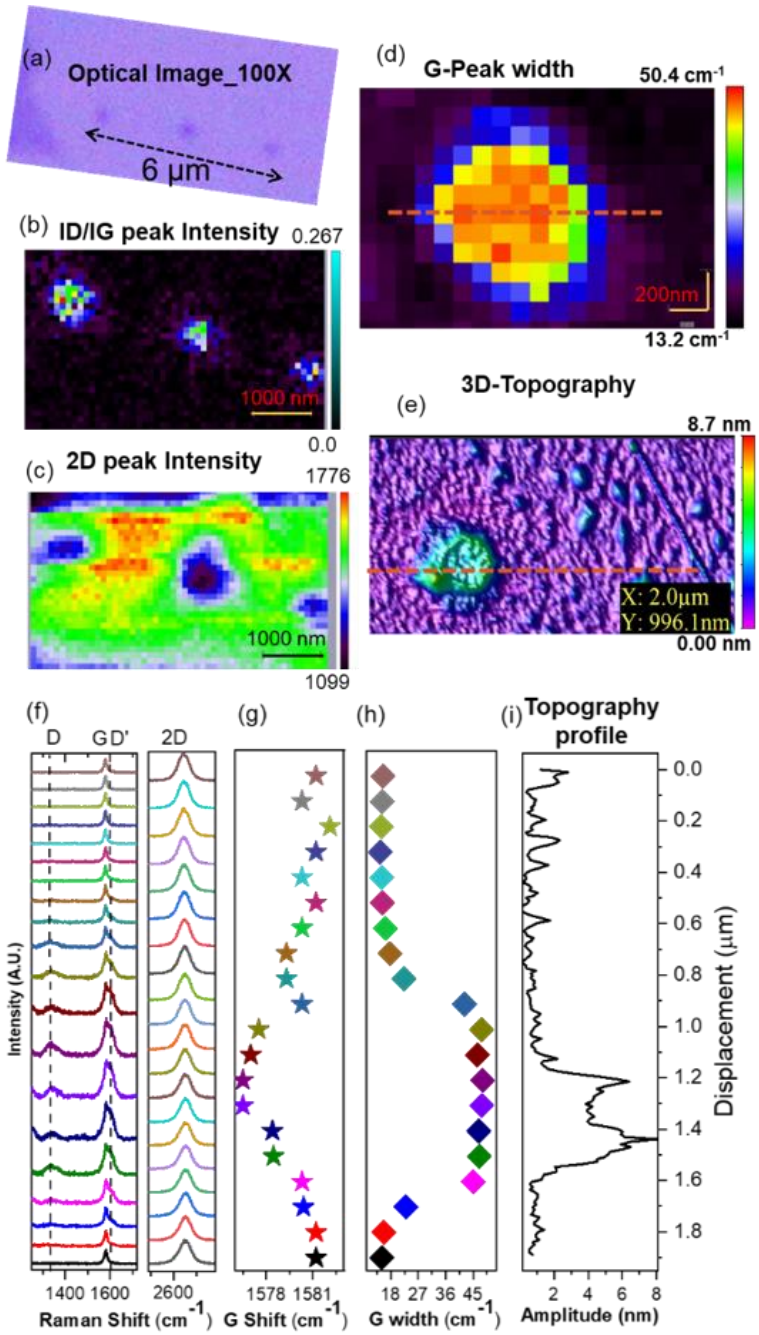

Figure 4.6 Correlation between topography and functionalization of graphene blister. *(a) The optical microscopy of produced blisters (i.e. post-treated) at 100X optical lens. The separation between each blister is 2 microns. (b, c, d). Raman map (resolution 100 nm, sampling data 1581) for ID/IG ratio, 2D peak intensity and G-peak width in contrast to untreated graphene showing distinct signature from untreated single-layer graphene, scale bar is 200 nm. (e) AFM 3-D morphology of individual blister along with untreated surface. (f) Raman spectra of D and G peaks as a function of displacement showing a broadening of D and G peaks at the blistered region. (g, h) There is broadening and redshift in G peak as a function of displacement. (i) The equivalent topography of the same blister shows maximum altitude of 6 ± 1.5 nm.*

The effect of the laser irradiation in locally functionalizing the 1LG is investigated by studying the graphene blisters, optically distinguished by microscope imaging in **fig 4.6 (a)**, with high resolution AFM and Raman mapping with increased resolution. As established previously, in **fig 4.6 (b)** we can observe again how the I_D/I_G ratio shows increase values in the central area of the blister, where there is the introduction of a Raman active disordered region. In addition, a decrease in the intensity of the 2D peak, **fig 4.6 (c)**, and broadening of the G peak width, **fig 4.6 (d)**, is confirmed in the central area. Having the possibility of analysing the same exact blister, correlation was obtained between the AFM data and the Raman line mapping, with G peak width, **fig 4.6 (d)**, correlated with height in **fig 4.6 (e)**. The Raman line data is comprised of 20 spectra spaced 100 nm between each point, all represented in **fig. 4.6 (f)**, showing the systematic increment of the D peak intensity at 1335 cm^{-1}.Also a softening of the G peak becomes apparent around the 3D features of the blister, **fig 4.6 (g)**, coupled with the broadening, **fig 4.6 (h)**, all factors suggesting partial oxidation with structural disorder [127], [137], confirmed by the presence of the carboxylic group in the FT-IR spectra **fig. 4.7**.

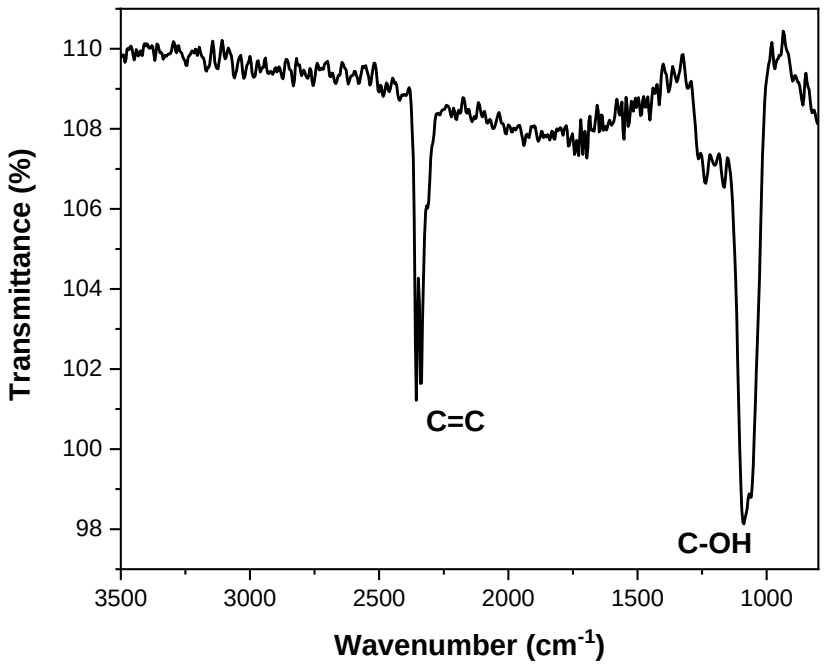

***Figure 4.7 FT-IR spectra** of 1LG after laser treatment shows the presence of oxygenic functional groups.*

4.5 Conclusions

This work demonstrated how the use of a simple high energy Raman spectrometer can be employed for the creation of 3D structures in 1LG graphene. The resulting creation is dependent on laser intensity, with higher intensity producing higher features, due to lattice expansion and the creation of oxygenic functional group, which alter the local electric properties as shown by KPFM. In particular, a decrease of work function was established, similarly to other 3D features like wrinkle and nanobubbles, due to increased distance from the substrate prohibiting p-doping from silica.

A reduction in the domain size of the sp^2 breathing mode was demonstrate with the analyses of the I_G/I_{2D} ratio along the blister, with phonon softening towards the central part of the blistered region showing lattice expansion of the carbon atoms. The defect density measured from I_D/I_G decreases as it goes away from the laser affected region (R_h to R_l) affirmed an annular shape for the distribution of defects.

The correlation of Raman and KPFM data may give new insight in the interpretation of mechanical strains on the graphene structure as normally interpreted by the I_D/I_G ratio. The possibility of better estimating the intensity of the *p* or *n* doping felt by the strained structure may help the interpretation of the I_D/I_G plot, were for example *p* doping has an effect that is diametrically opposed to the one induced by strain. These results showed the effectiveness of the Raman spectrometer for the modifications and functional analysis of graphene layer in a controlled and pre-programmed way, allowing the creation of desired patterns. This method may open new possibilities in graphene based devices to generate localised pseudomagnetic fields [97], localised functionalization of the surface obtaining areas with different adhesion forces and polarities for biosensing applications [138], and bandgap tailoring [139].

Chapter 5
KPFM measurements of the AgNW–graphene interface for transparent electrode applications

5.1 Introduction

In the last decade there has been great effort put into the development of novel thin film materials with high transparency (T) coupled with high conductivity σ. This has been driven by the fact that most transparent electrodes today, for example for smartphone touchscreens, are made from ITO, indium doped tin oxide. This material, as of today, has some of highest values of electrical conductivity, with a sheet resistance (R_s) of less than 100 Ω/sq, combined with transparency (T) around 90% being routinely achievable.

However, ITO has several drawbacks from a modern applications perspective, as it is brittle, expensive and requires high deposition temperatures to achieve maximum performance. In recent years, many candidates have been proposed as potential substitutes for ITO such as carbon nanotubes, metallic nanowires, graphene and hybrids of these materials.

Of the proposed options, metallic nanowires (in particular silver nanowire (AgNWs)) represent the best combination of reliability, and simplicity of synthesis, deposition process, electrical conductivity and optical transmittance of the final functionalized substrate, with properties comparable to ITO [140]. Still, challenges remain in the use of AgNWs, as they are still relatively expensive and in order to achieve high electrical conductivity relatively dense films or otherwise very long nanowires are required.

Moreover, the resulting films are often hazy and require protective coating to prevent eventual oxidation and sulfurization from atmospheric contaminants. In order to reduce the required AgNW density while at the same time keeping the required conductivity, our group has explored in the past hybrids of AgNWs and graphene, successfully obtaining conductive transparent electrodes with excellent electrical properties and minimal decrease of transparency. In these hybrids, graphene flakes play the role of highly conductive parallel pathways for the current to flow and jump from nanowire to nanowire without having to surpass nanowire-to-nanowire junctions. While at the macroscale the improvement has been demonstrated, the nature of the nanoscale interactions between silver nanowires and graphene needs to be further studied to better understand the level of affinity between these two materials. From this understanding methodologies for manipulating the interaction may be developed through choice of specific materials and processing techniques.

This chapter will present original results on KPFM and Raman characterization of this hybrid system, showing how the coupling of these two characterization techniques can be an invaluable tool to explore the electrical coupling between graphene and AgNWs on a functionalized substrate.

5.2 Nanomaterials and AgNWs in transparent electrode technology

Smart devices represents a rapidly expanding area of electronics research and engineering, with transparent electrodes often playing critical functions in devices such as touch sensors [141], solar cells, smart windows and elements of digital displays and flexible lighting [142], [143]. Currently, transparent electrodes are made from doped metallic oxides, mainly indium doped tin oxides (ITO), due to their low sheet resistance and high transparency in the visible range. ITO has been used for applications and its processing has been developed in industry for more than 60 years, setting the gold standard for sheet resistance, $R_s \sim 100\Omega$/sq, coupled with optimal transmittance, T>90% [144]. However, ITO usage presents several problems related to its mechanical properties, being brittle and losing functionality when flexed [145]–[147], and to the high cost of the material itself, due to the high demand and fluctuating supply of pure indium, which is a by-product of mining other metals, in the market [148].

In summary, ITO has limited use in innovative and flexible devices due to high cost, brittleness, and the high temperature required to achieve maximum materials performance [149], [150].

Since the market is quickly moving toward flexible transparent electrodes, it is clear that new materials and solutions need to be found that can be produced at large scale at low temperature and over large areas at low cost. Many possible solutions have been proposed, using carbon nanotubes, graphene, or hybrids of these materials [151]. Carbon nanotubes (CNTs) are theoretically very promising, with possible conductive values far exceeding current transparent electrodes [152], however this material is greatly limited

by the difficulty of the synthesis, purification and separation process. This is very important as a combination of semiconducting and metallic CNTs, which is the form in which they are produced, have high variability of local properties and tend to quickly degrade during use [152].

Graphene is another material that theoretically, if deposited in a single layer form, shows the necessary transparency and outstanding conductivity necessary for these applications, with experimentally-measured values of 97% transmittance and around 60 Ω/sq [146], with individual graphene flakes showing in plane conductivity as low as 30 Ω/sq [153]. Graphene also shows excellent thermal stability with the film remaining intact after heating up to 400°C in air [154].

Still, graphene also presents similar problems to CNTs for the synthesis and orderly deposition process: the process capable of producing the largest single sheets of graphene with precise control of the number of layers, chemical vapour deposition (CVD), produces graphene sheets presenting multiple incorporated defects like grain boundaries, ripples and wrinkles, which increase R_s dramatically [155]. Standard techniques of deposition for liquid processed materials, like drop-casting, spin-coating, spraying, instead tend to lack the necessary lateral size of the sheets and will present a more disordered deposition which increases the resistance due to the presence of sheet-to-sheet which manifest as tunnelling barriers for electron transport. Promising results have been presented in literature using Langmuir-type assembly thanks to the possibility of controlling density and compactness of the film [156]. The primary advantage of this technique is that since the particles of material are all trapped at the air-water interface they form, by necessity, a pseudo-2D layer of particles; careful controls prevents overlap and facilitates the thinnest possible arrangement of sheets to produce highly-conducting network that can be easily transferred to the target substrate..

Random networks of metal nanowires have shown the most promising practical results [146] thanks to their high aspect ratio and relatively simple synthesis and deposition procedures compared with graphene and CNTs. In particular, promising results have been shown for silver nanowire networks, with randomly distributed networks presenting R_s values of less than 100 Ω/sq and >90% transmittance, and even lower values of R_s at the expense of the transparency at higher densities. In the realization of working prototypes, moderate success has been achieved by using AgNWs in many fields where ITO is employed, like solar cells [157], sensors [158] and transparent electrodes [145]. Still, today, AgNWs represent one of the potential better candidates for the industry, showing high electrical and thermal conductivity, as well as excellent optical transmittance depending on the deposited metallic network density [140], [159], [160].

In particular, promising results have been shown on the production of flexible devices, as they maintain properties when bent or stretched up to 50% more than their original size [161]. Prototypes of flexible transparent conductive thin films have been already produced [142], [145], [157], [162], with many different techniques employed to create the deposited network such as vacuum filtration [140], Langmuir-Blodgett [163], drop casting [145], [164], Meyer-rod-coating [143], and spray-deposition [165].

Whatever the preparation method, the key parameters for a successful device were the morphological parameters of the nanowires and the inter-wire junction characteristics, affecting both electrical and optical properties. In particular, inter-wire junctions presents one of the main obstacles of the material, due to the synthesis process leaving polymeric residue that can’t be completely removed without disrupting the overall structure of the nanowires, due to strong coordination bonding of the polymer with the silver surface. The standard procedure to overcome this problem is a heat treatment to fuse the junctions [166], which due to small radius of curvature of the nanowires allows for local surface

sintering at much lower temperatures than the bulk silver melting temperature. Still, this heat treatment may have negative effects on the substrate and overall also represent another expensive step in the procedure [167].

Furthermore, mechanical robustness and flexibility of the AgNW networks need further improvement to be properly employed in flexible devices [168], which also require proper adhesion to the substrate which is still not optimized for many materials as of today. Over time, if networks are not properly protected they are also susceptible of oxidation and sulfurization, which results in a gradual increase of sheet resistance and haze in the transparent electrode over time [169]. Metal nanowires in particular at high densities present a relatively high fabrication cost, high nanowire-to-nanowire resistance and poor adhesion to plastic substrates, limiting the use in industrial applications, as AgNWs are still relatively expensive, with a price of around £2.5/mg.

Our group [170] has proposed a hybrid solution combining an AgNW film and graphene flakes deposited on the substrate through Langmuir-Schaefer deposition, obtaining working prototypes with minimal decrease of transmittance and improved electrical conductivity **fig. 5.1 (A)**, with the resulting R_s comparable or better to ITO substrates. In **fig. 5.1 (B)**, a touch screen device is presented showing the visible differences between the two conditions, pure AgNWs at the bottom and the hybrid on top. In this realisation the hybrid film has a sheet resistance approximately a factor of 50 lower than the pure AgNWs, for a comparable film transmittance (visible in the inset in **fig 5.1 (B)**).

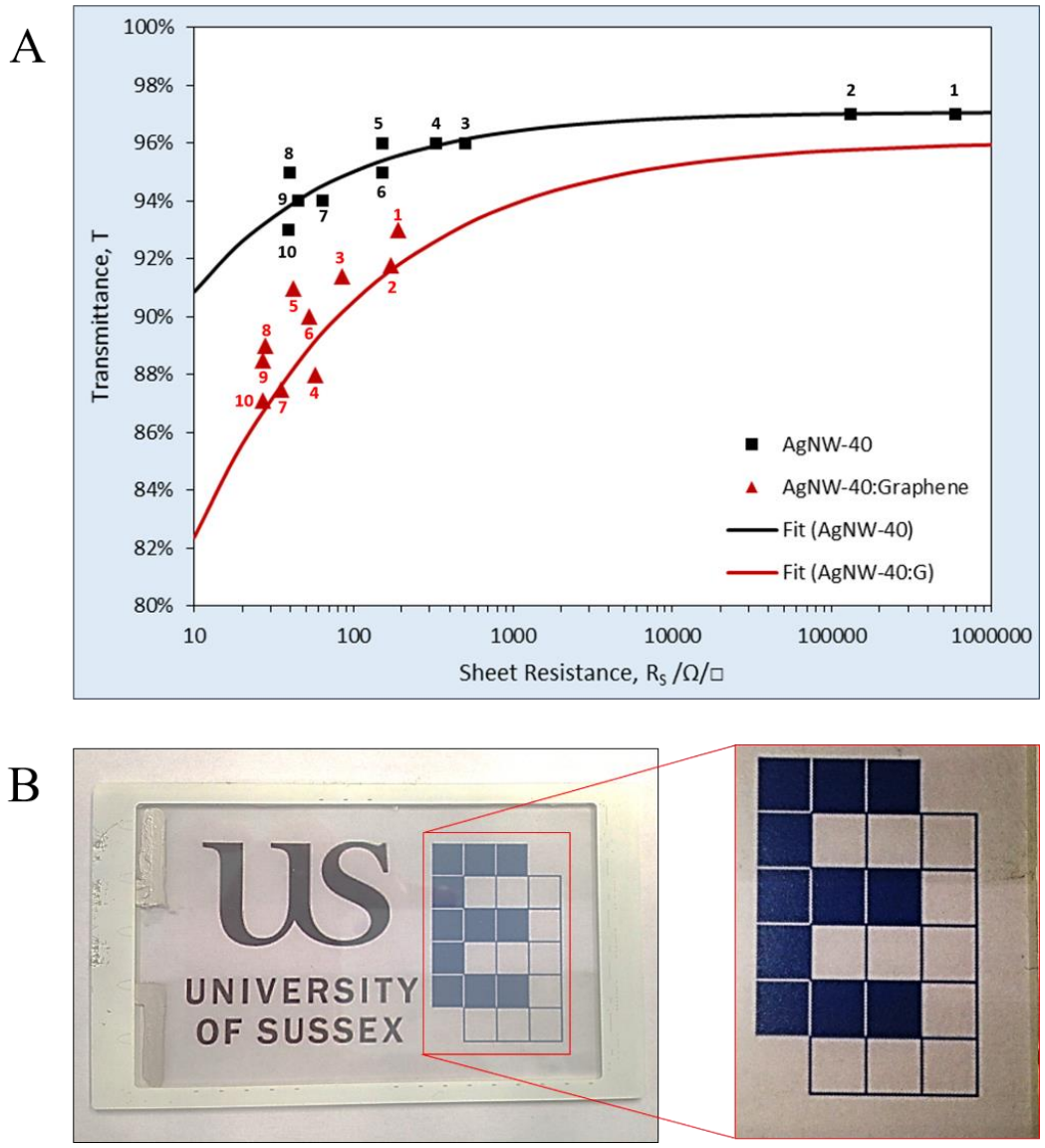

Figure 5.1 T-Rs graph for AgNWs and graphene hybrid systems. *In (A), every numbered point represents a different density of AgNWs on the substrate, with the density increasing with the associated reference number. The Rs value for each of these conditions is plotted for both the pristine AgNW condition and the hybrid condition, showing how even at very low density the addition of graphene greatly improve the conductivity while decreasing T of less than 10%. In (B), this result is shown in a real device condition where the top show the hybrid condition and the bottom the pristine AgNW one, with the hybrid presenting a sheet resistance 50 times lower than the AgNW film for comparable transmittance.*

The proposed principle driving the improvement was the creation of low resistance pathways due to the presence of the flakes, allowing the bridging of different nanowires, hence reducing the total length of the path traversed by the current and, even more importantly, reducing the effect of the nanowire-to-nanowire junction resistance, which

represents one of the main limiting factors of AgNWs films, without the requirement for thermal treatments. Still, the nature of this contact needs to be further explored, as pure silver is not normally known to have great affinity to graphene [171], and the amount of contact area between the two components needs to be as high as possible to decrease the contact resistance, hence requiring the graphene flakes to bend around the nanowire as much as possible. Furthermore, the properties of such electrical connections still need further studies as in their most common synthesis route, the AgNWs are covered by at least a single molecular layer of PVP on their lateral faces, requiring tunnelling from the nanowire to the flake and back from the flake to the connected nanowire for this increase to be justified, hence requiring some local probing of the flake surface on top of the nanowire to confirm this electrical interaction.

In this work, the efficient electrical coupling between the AgNWs and graphene is investigate by virtue of KPFM analyses, showing how the two elements strongly interact and the flow of electrons is permitted, creating distinct change in work function. This property was further tested with different substrates, glass and ITO, to further establish independence of the behaviour from the possible doping effect of the substrate itself. Furthermore, bending of the graphene sheet is analysed using the Raman spectrometer [130] following the same principle applied to the blisters in chapter 4. KPFM can further help this type of characterization by giving some insight on the type of doping that the graphene flake is subjected to, allowing for a better interpretation of the obtained data points.

5.3 Silver Nanowires synthesis, deposition and characterization

As previously stated, AgNWs represent a promising nanomaterial for transparent electrodes and in general conductive substrate, allowing with a minimal amount of material the functionalization of large areas with simple and non-destructive techniques ranging from drop casting to spraying. Spray coating produces relatively uniform films in large-scale substrates, even though it is influenced by many parameters such as spraying pressure, flow rate, scan speed, height and substrate temperature [165].

As previously mentioned, the addition of liquid-exfoliated graphene was suggested as a way to improve the conductivity of the transparent electrode with minimal loss of transparency and minimal cost, using a Langmuir-Schafer deposition process. Liquid-phase exfoliation of graphene tends to create very small flakes, and the Langmuir deposition process does not ensure that flakes are deposited to ensure contact between silver nanowires and graphene flakes. This is particularly problematic at the low AgNW density necessary for proper KPFM characterization. Therefore, for this study a different graphene deposition approach, based on transfer of CVD grown films, was employed to have guaranteed coverage of the AgNW network, allowing the use of a less dense network for the better localization of isolated nanowires during analyses.

The sample used for this characterization was prepared by spraying AgNWs, bought from SigmaAldrich® and with nominal diameter of 25 nm and length of 15 µm, on a glass substrate. These dispersions are stable in IPA (Isopropyl Alcohol) for extended periods without any visible sedimentation over days to weeks. The glass substrate was prepared with two of its lateral margins covered by silver paint to be connected to the ground for

KPFM and electrical measurements, and spraying was continued until conductivity across the whole surface was confirmed with standard multi-meter measurement connected to such silver painted areas during the spraying process, **fig 5.2 (A)**. The sample was then dried in a closed desiccator, electrically measured and characterized with a standard AFM topography measurement, using 5 different areas of 20 μm^2 to average the coverage of nanowires and PVP residual on the substrate, **fig 5.2 (B)**. Average AgNW length was calculated using measurements of around 100 AgNWs from those areas, **fig 5.2 (C)**, to establish that the nanowires were on average sufficiently long to properly create a patterned structure on the substrate for the graphene deposition. The sample was then dipped for 5 seconds with minimal shaking in deionised water to decrease the amount of residue on the substrate and the polymer capping layer, then dried in the desiccator and re-characterized with AFM as previously described.

The process was repeated five times and results plotted together with the Rs measured values after each cleaning step, **fig 5.2 (D)**, demonstrating a slight improvement of resistance after the first washing probably due to the removal of most of the PVP residue. The cleaning process probably reduces the overall density and coverage of PVP and removes silver seed crystals present from the synthesis, allowing for a better contact with the transferred CVD graphene. The Rs value in this case was still very high due to the very low density of the AgNW network, allowing better conditions for KPFM analyses.

The nanowires were also imaged with a TEM before the washing procedure to establish the PVP capping layer thickness of the as received product, showing a starting average thickness of around 10 nm, **fig. 5.2 (E)** and **fig. 5.2 (F)**. The presence of residual encapsulated silver nanoparticles at the edges of the nanowires, as visible in the red square of **fig. 5.2 (E)**, proved the necessity of the cleaning procedure as this would present an obstacle to the proper electrical connection between graphene and the silver nanowires.

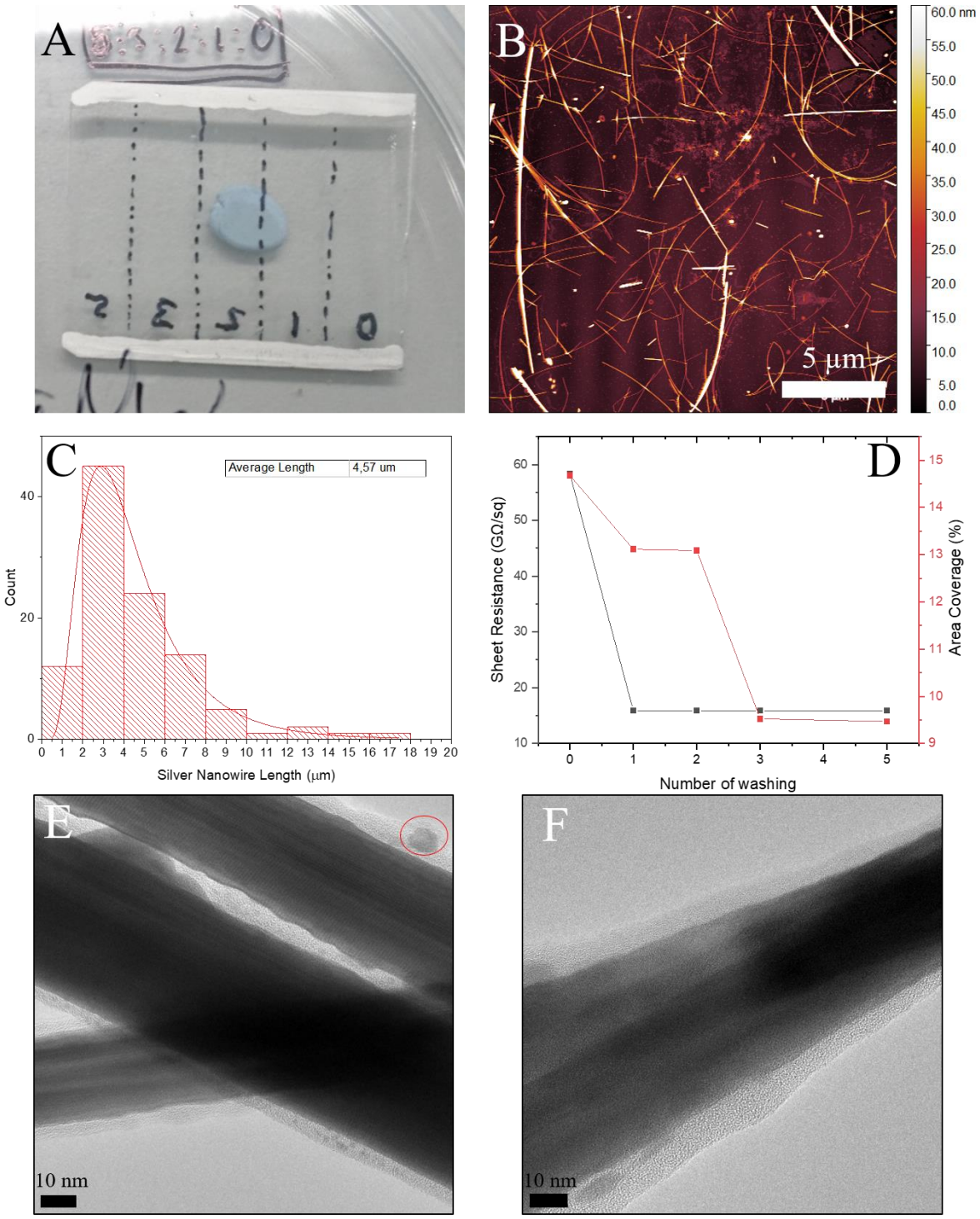

Figure 5.2 Characterization of the AgNWs functionalized glass substrate. *The AgNW functionalized glass slide (A), showing the silver paint at the top and bottom edges used to measure the Rs and operate the KPFM characterization, divided vertically in five areas that will receive different amount of washings. Representative AFM topography of the imaged areas (B) used to average the AgNW length (C) and the area coverage after each washing and drying cycle, showing an improvement of Rs and decrease of area coverage due to the PVP and silver nanocrystal residues being removed during the process (D). The high value of sheet Rs is caused by the low density of the AgNW network necessary for AFM analyses. In (E) and (F), TEM characterization of the AgNW nanowires before washing is presented, showing a PVP capping of around 10 nm, in some case still encapsulating Ag nanoparticles as highlighted in the red circle in (E), which would represent a point of bad contact between nanowire and graphene if not removed.*

Samples were then sent to Graphenea®, a company in Spain specializing in deposition of CVD graphene layers onto arbitrary substrates, to be covered by a monolayer of graphene for the study of the composite metal/graphene hybrid. The resulting sample showed high level of breakage of the AgNW network and wire structure, probably due to the cleaning procedure necessary for the successful transfer of monolayer graphene into the substrate, **fig. 5.3**. The sample showed a great number of silver nanoparticles, arranged in a way that suggests that they still follow the shape of the destroyed nanowires, in a similar way to the observed thermal degradation in literature. The network normally becomes completely disrupted at around 205°C, with minor measurable disruption starting at around 165°C. [172].

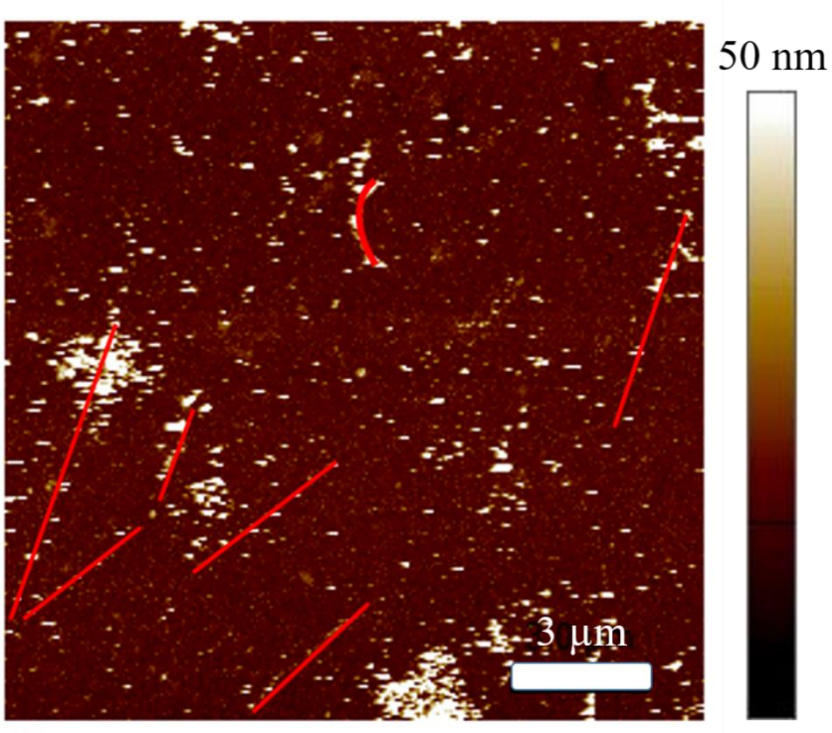

Figure 5.3 Effect of the Graphenea cleaning and transfer procedure on the central part of the sample*. The heating process necessary to remove the polymeric stamp used to transfer the monolayer of CVD graphene seem to have degraded the nanowires structure, creating isolated nanoparticles, particularly in the central area of the substrate where the best contact between AgNWs and graphene was achieved.*

At these temperatures, due to a mix of thermal agitation and degradation of the stabilising PVP layer, the silver atoms at the edges of the lateral (100) surfaces of the silver nanowire tend to diffuse and reconfigure in a more stable (111) arrangement, which is the crystallography typical of the silver seeds and the terminal faces of the nanowire. This process create centres of aggregation all along the nanowire, inducing the breakage of the nanowire and the creation of the nanoparticles. Interestingly, during the cleaning process, the maximum temperature applied was 120°C, per our request (the lowest temperature at which the process can be done), which would not normally be expected to yield observable disruption, although the time may be the key parameter since the heating was applied for a very long interval of time.

The cleaning process performed by Graphenea includes washing with IPA, water and acetone, with the stronger treatment happening after the graphene flake deposition, with a process described as follows:

- PMMA mould with the monolayer of CVD grown graphene is brought to contact with the substrate.
- 10h in an oven at 120°C.
- 30 minutes in an acetone bath.
- 30 minutes in an IPA bath.
- Drying with a N_2 gun.

Since both IPA and water are common solvents used for storage of the AgNWs, those unlikely to be problematic. High concentration of acetone instead could theoretically damage the PVP layer, even though in previous works the minimal thickness after all types of washing was always a single layer of PVP [173]. In addition, the monolayer of graphene should protect the underlying structure from the action of the solvents.

An interesting possibility is that the contact with the monolayer of graphene and the AgNWs, due to the high thermal conductivity of graphene and the compression of the PVP layer from the flake, coupled, increase the local effect of temperature of the PVP layer inducing disruption even at 120°C. This would find some confirmation from the fact that the areas with the highest amount of disruption were found in the central part of the sample, were contact was properly established between the flake and the substrate. Meanwhile, the areas presenting the best AgNWs for KPFM and Raman characterization were found closer to the silver paint, where the surface was rougher due to the presence of the paint, allowing for a better dispersion of heat.

5.4 KPFM and Raman characterization of the AgNW/Graphene system

As mentioned in the previous section, the AgNW network deposited on top of the glass substrate was partially destroyed during the extensive processing during graphene deposition, leaving behind silver nanoparticles. However, where present after deposition, the surviving silver nanowires gave very high contrast on the KPFM, confirming the success of the graphene connection to the AFM electrical ground through the silver paint. In the topography, **fig 5.4 (A)**, we can observe how the nanowire structure has been reorganized due to the probable decaying of the PVP coating stabilising the lateral surfaces of the AgNW, with some big nanoparticles connected by residual nanowire structure. There are also some sparse and smaller nanoparticles, commonly found after the deposition process of nanowires, and some features typical of CVD monolayer graphene like wrinkles appearing as short straight line, highlighted in blue in **fig 5.4 (B)**, while the nanowires are marked in red.

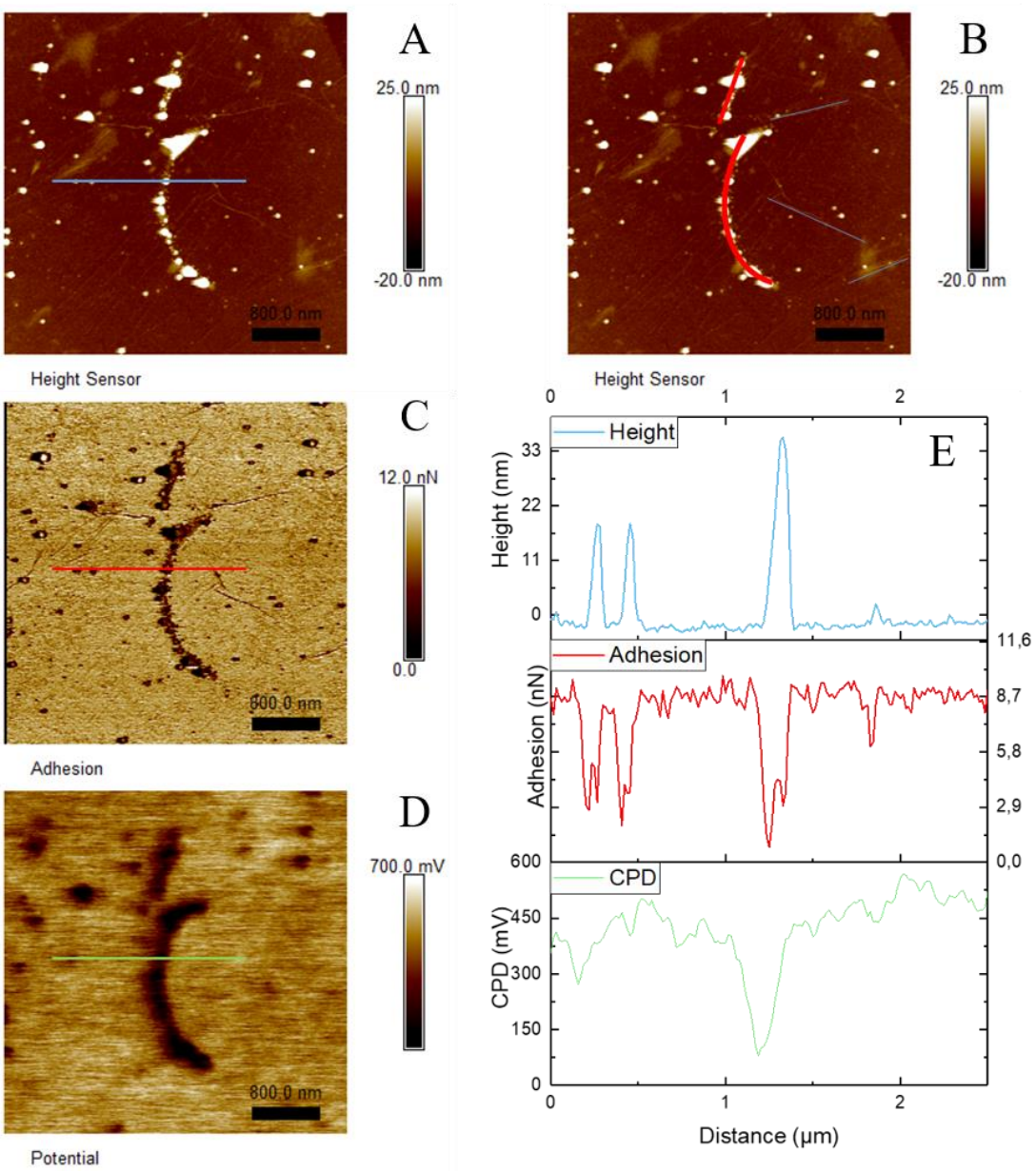

Figure 5.4 KPFM characterization of the partially degraded nanowire covered by CVD grown graphene. *AFM topography (A) of the partially degraded silver nanowire on glass, showing a structure of silver cluster connected by the remains of the nanowire. In red, the original shape of the nanowires has been highlighted, while in blue some wrinkles have been traced (B). These wrinkles are hard to see on the height channel as they are much shorter than the AgNW, but they become clearly visible in the adhesion channel (C), due to their stiff nature compared to the basal plane. KPFM data is shown (D), presenting very high contrast between basal plane and graphene on top of the nanowire, with a CPD difference in the order of 300 mV (E), and equal to a work function difference of almost 0.3 eV. This range of difference can be only justified by a highly conductive interface between the two elements, allowing for the transfer of electrons to balance the work function difference between the two surfaces.*

The wrinkles are less visible in the topography channel due to the height of the nanowires increasing the range of the scale, but then become immediately visible in the adhesion channel, **fig. 5.4 (C)**. The wrinkles and the graphene immediately surrounding the nanowire are strained, hampering the penetration of the tip and hence decreasing adhesion, which can be generally described as the amount of interaction between tip and sample while in the retraction part of the tapping cycle. Finally, in **fig. 5.4 (D)**, the KPFM data is presented, showing a very large decrease in the CPD value between tip and graphene in presence of the silver nanowire underneath, of almost 300 mV in the central part of the nanowire, corresponding to a decrease of almost 0.3 eV in the work function value of the graphene.

The proper deposition of monolayer graphene all around the nanowire is guaranteed, allowing for a clear distinction of the baseline value from the value of the graphene on top of the silver nanowire. In **fig. 5.4 (E)**, the summary of the data corresponding to the same section in the three data channels is presented. This type of decrease in work function suggests a strong electronic interaction between the AgNW and graphene, with the decrease of CPD suggesting that graphene tends to easily attract electrons from the nanowire, effectively being n-doped by it. It can also be noted that the silver nanoparticle at the start of the line section has a similar effect on the work function, suggesting the same mechanism.

While the magnitude of the CPD contrast suggests by itself that the nature of the change is due to a highly efficient electrical connection, further data is needed to confirm that this behaviour is not simply caused by some type of general p-doping of the CVD graphene by the glass substrate, with the apparent n-doping simply caused by the forced separation of the monolayer from the substrate itself by the nanowire.

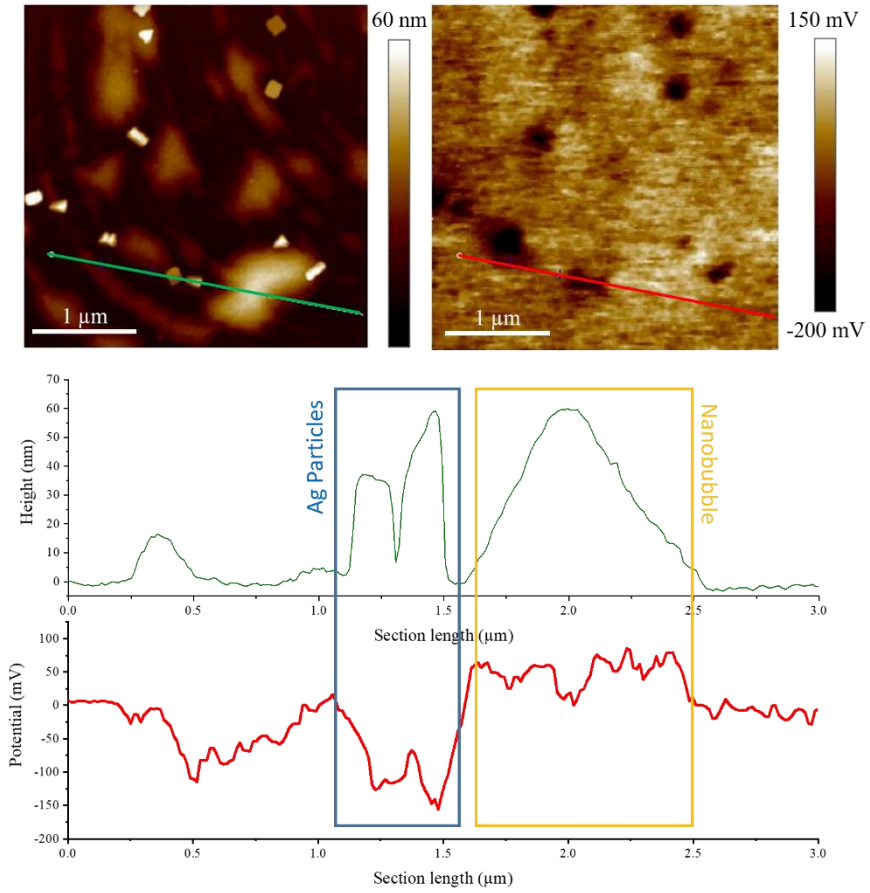

Figure 5.5 Comparison between the effect of the monolayer-substrate separation and the effect of silver nanocrystal on the CPD value*. AFM topography of an area presenting both silver nanocrystals and nanobubbles (A). If the CPD present on top of the silver nanowire and nanocrystal would have been mainly due to the substrate-monolayer separation, the nanoblister should present a similar CPD value compared in both condition, particularly if the height is comparable. Instead in (C) it is shown how not only the CPD value is not comparable, but has even the opposite effect, confirming that the effect on top of the nanocrystals is only due to the electrical coupling between the two components.*

To confirm this, an area with graphene nanobubbles, probably induced during the heating process from the vaporisation of trapped absorbed molecules between the glass substrate and the monolayer, and silver nanocrystal was further characterized with KPFM, as visible in **fig. 5.5 (A)** and **fig. 5.5 (B)**. In single scan area, we can observe how the glass substrate seems to have an opposite effect on the detached monolayer, with the CPD, represented in red, slightly increasing instead of decreasing in the part of the height data, represented in green, corresponding to the bubble, **fig. 5.5 (C)**.

Instead, the areas over the silver nanocrystals presented a very marked decreased in work function, confirming the strong electronic interaction between the two elements and the independence of this property from the distance of the monolayer from the substrate. The two coloured boxes further highlight the correlation between height and CPD data for each feature.

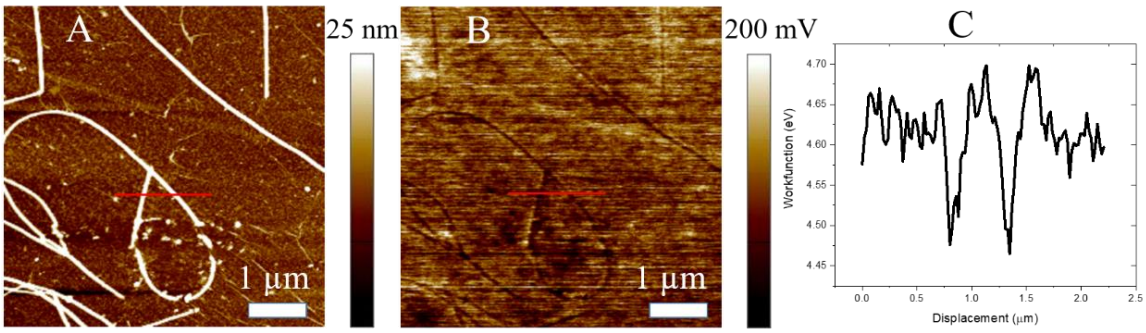

Figure 5.6 Similar deposition and characterization on top of an ITO substrate and analyses of the resulting strain with the Raman spectrometer*. AFM topography of AgNW sprayed on ITO and covered by CVD graphene (A), showing in this case a well preserved nanowire and hence a shorter vertical dimension. The resulting KPFM characterization proves the same type of behaviour, with a decrease in CPD value on top of the nanowire (B), further visualized in the line plot in (C). In this situation, the absolute CPD value is lower due to the different effect of the ITO on the surrounding graphene basal plane.*

Finally, to further test these results, following a similar procedure CVD grown graphene was deposited on top of an ITO substrate functionalized with AgNWs, and again characterized by AFM, **fig. 5.6 (A)**, and by KPFM, **fig. 5.6 (B)**. In this case the decrease is smaller but still very noticeable, of the order of 200 mV, suggesting that a properly formed nanowire will have a less effective electrical contact with the graphene monolayer due to probably a better preserved PVP capping around it, **fig. 5.6 (C)**. Finally, we use these KPFM data to better understand the data from a Raman line mapping of the graphene monolayer on top and around the nanowire.

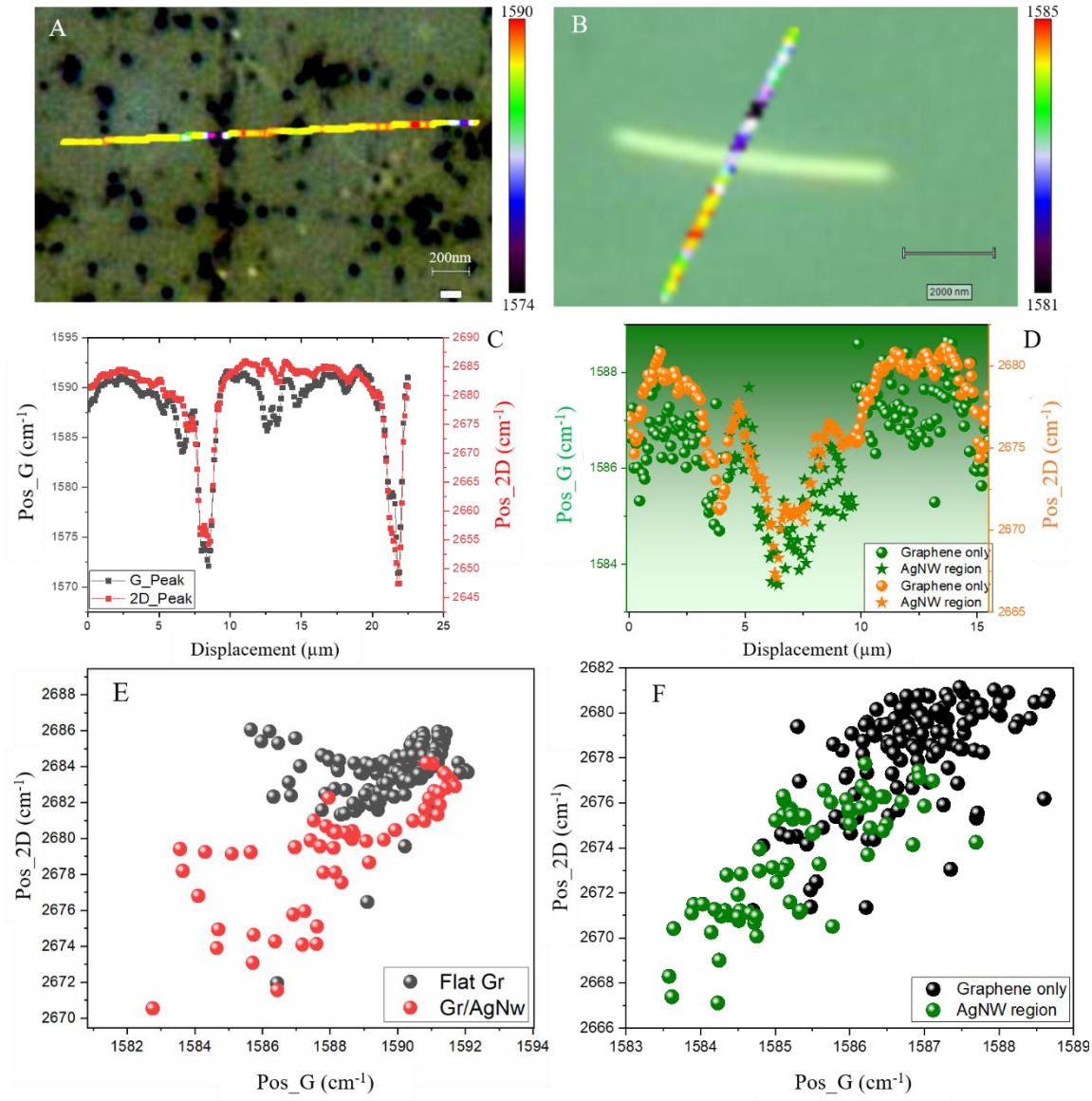

Figure 4.7 Raman characterization of the deposited CVD monolayer graphene on different substrates. *In (A) the microscope pictures of the glass substrate area and in (B) the ITO substrate area used for Raman characterization are presented. Then the resulting G and 2D peak positions are plotted in a single graph for the glass substrate (C) and the ITO substrate (D). Finally, in (F) the corresponding 2D-G scatter plot for different points obtained by the line scan is presented, showing the expected shift in the down-left direction typical of the strained graphene on the area on top and in proximity of the nanowire, represented by the green dots. In (E) the same plot has been done for the glass substrate, which considering the higher height should present higher strain. Instead the points in red, representing the points on top and closer to the nanowire, seems to be nearer to the cluster of the basal plane compared to the ITO case and shifted to the right. This is well in accordance of the underlying theory, which identify n-doping as a rightward shift, and highlights the importance of having KPFM data to properly interpret this kind of data.*

In **fig. 5.7 (A)**, the glass substrate area considered for the Raman line scan is shown, presenting all the underlying silver residue under the graphene monolayer, while in **fig. 5.7 (B)** it is visible how finding and visualizing a full isolated nanowire is much easier. In both cases, the colour scale represents the G peak position. For both line scan, the measured values for the G and 2D peak position along the line scan is plotted, with **fig. 5.7 (C)** representing the glass substrate and **fig. 5.7 (D)** the ITO substrate. This plot made the areas in which the nanowire is present immediately visible, due to the down-shift of both values. Each point was then plotted based on its 2D and G peak position value to observe the differences of distribution between areas of graphene on top of the nanowire and areas of just monolayer graphene.

In the ITO case, **fig. 5.7 (F)**, we can immediately observe the expected strain of the graphene around the nanowire, adding to the case of a good coupling between the two system, since, as established in the previous chapter, based on [130], in the 2D-G plot a shift toward the bottom left of the graph is indicative of strain. Interestingly, compared to the glass case, **fig 5.6 (E)**, we would expect a higher strain as the partially degraded structure of the silver nanowire in that situation would amount to a higher height and hence higher slope for the monolayer to compensate.

It is interesting how in this case the utility of the KPFM may become apparent, as the very strong n-doping from the silver nanowire and partially on the substrate operates in a rightward direction on the 2D-G plot and so it tends to move the reduce partially the effect of the expected shift from the strain. While this type of approach would need a much greater number of points with better-defined features for proper averaging, the results from a KPFM characterization of the substrate seem to be a key for the proper interpretation of this type of Raman data, particularly when the doping effect is that strong.

5.5 Conclusions

Silver nanowires and graphene hybrids have proved to be a very promising candidate for transparent, highly conductive, flexible transparent electrodes. While the group has measured the improvement of the macroscale properties of the hybrid films in previous works, the strength and the nature of the nanoscale interaction between these two components can be further studied. The goal of the study proposed in this chapter is to give tools to better characterize and understand the strength of the electrical coupling between AgNWs and graphene, with the approach extendable directly to other 2D materials.

A glass substrate functionalized with AgNWs has been covered by a monolayer of CVD graphene, showing how the work function of the graphene greatly changes on top of the silver nanowire compared to the surrounding substrate. This change has been demonstrated to be independent of the distance of the monolayer from the substrate, contrary to the results on nanobubbles and blisters in mechanically cleaved graphene monolayers in chapter 4, utilising KPFM characterization of areas presenting both silver nanocrystal and graphene nanobubbles.

Furthermore, the same analyses were performed on a different substrate, in this case ITO, to confirm the same behaviour was independent from the specific environment in which the system was deposited. In this second case, the nature of the doping effect on the graphene was proven to be the same even though the absolute intensity of course different due the different work function of ITO compared to glass.

Finally, the same theory used to determine the strain of monolayer graphene using Raman spectroscopy has been applied to a line section with graphene on top of and around a

AgNW. This approach is sensitive to the type of doping of the analysed graphene, and in cases like this one, where the intensity of the doping is particularly great, it has been shown that a secondary technique like KPFM is fundamental to correctly interpret the data. I believe that the coupling of these two techniques should become the basic approach in future straintronics studies for both theoretical works on the relationship between strained graphene and electrical properties, and for real life applications like this one where the magnitude of the strain on top of the other conductive element could yeld some insight on the affinity between the two elements electrically coupled.

Chapter 6
KPFM characterization of graphene – latex composites

6.1 Introduction

The use of 2D materials in real life applications is generally limited by the difficulty of synthesis, storage, proper characterization and uniformity of the resulting products. Fast and easy to use techniques like the AFM allow the proper checking of both the resulting product of the synthesis process and the final nanomaterial assembly. The final goal is obtaining a conductive graphene composite, using the minimal amount of material possible employing the latex assembly technique. In this technique, a stable emulsion of polymer nanobeads is left to slowly dry at mild temperatures, allowing the beads to arrange in an organized way while there is still enough water solution for them to move around freely, followed up by a step in which strong capillary forces induced by the interstitial water evaporating create strong adhesion forces between the polymer beads, inducing compacting of the film [151].

In this work, AFM was used to observe the properties of different batches of the same starting material, and then characterize the surface and electrical properties of the final composite material to better understand the distribution of the included nanomaterial, and its interaction with the polymer matrix.

The use of pristine graphene in composite applications is hindered by its tendency to re-aggregate in the solution in which it is stored, leading to variability in the final composite properties even starting from the same graphene solution based on the amount of time

passed from its synthesis. Furthermore, even the best process for large scale synthesis of pristine graphene, liquid exfoliation [174], requires the use of surfactant and solvents which may contaminate the final product, while at the same time producing small flakes with generally very low lateral size (of the order of several hundreds of nanometres). In particular, for composites applications, the presence of surfactant molecules may interact with the polymeric species during the matrix formation steps, changing the resulting properties unpredictably through plasticization of the macromolecular chains or by flocculation of residue in liquid suspensions.

The solution was found by utilising graphene oxide (GO), which is obtained from the addiction of oxygen functional groups, like carboxylic, hydroxyl and epoxide groups, in the graphene structure, during the all the steps till the drying process of the composite. The advantages of GO are the possibility of obtaining it in high yield with simple chemical methods starting from cheap graphite, with the most commonly used process called the modified Hummer's method [175]. The highly hydrophilic nature of GO allows the formation of stable dispersions in water or other polar solvents.

The re-aggregation process is hindered by the functional groups as opposed to the need for surfactants to stabilise pristine graphene solutions, removing the necessity of predicting unexpected chemical reactions. This makes GO a very interesting starting material for a large variety of industrial processes that require large quantities of material. In particular, it becomes highly advantageous for applications that require aqueous starting solutions, like for high loading composites materials, coatings and paints.

Still, GO is not a conductive material, and, when the superior electronic properties of graphene are required, it becomes necessary to remove the oxygen-containing functional groups with a reduction process. This may be performed with different techniques, like

thermal annealing [176], [177], chemical reduction [178]–[180], or microwave irradiation [181]. Thermal reduction proceeds passing through mainly two thermal ranges. The decomposition of the oxygenic groups, mainly the epoxy ones occurs between the 150°C and 200°C window [182]. Subsequently, at much higher temperatures, but lower than 1000°C, all the basal plane defects are annealed resulting in near-pristine sp^2 hybridised carbon material [183]. During the first range, the reaction is strongly exothermic [184] and leads to the removal of almost all oxygen, but the basal plane structure still presents defects. This step is also associated with a visible transition of the material from brown to black.

The matrix material that will incorporate the GO is instead chosen to be compatible with a latex assembly procedure [185], which allows the enhancement of the composite properties at lower filler content than standard mixing processes. This process employs emulsion polymerization [186], which is commonly used in industrial processes, to produce a charge stabilised colloidal suspension of polymer spheres. Latex matrices have been used in the past for a wide range of applications, like transparent, flexible and conductive composites with metal powder fillers [187], [188] or carbon black [189].

The process reduces the amount of filler required because it confines it at the interstitial spaces between the spheres during the drying process. Furthermore, the proper choice of the spheres dimension distribution may allow the control of the actual dimension of the pores for further optimization of the total filler quantity. This type of structural organization is commonly known as Apollonian packing [190], which arise by repeatedly filling the interstices between mutually tangent circles with further tangent circles and it has been studied in the fields of mathematics for decades. Experimental evidence has been observed for dispersion of polymer nanospheres in other studies [191]–[193].

Examples of successful use of this technique and control of the process can be found by Grunlan *et al*. already in 2001 [194] for carbon black used as a conductive filler, and Jurewicz *et al*. [195] for the highly ordered distribution of carbon nanotubes, expanding the use also to 1D nanomaterials. A general description of the latex drying and film formation process is given by Keddie [196]. Following these successful examples, this work focused on the proper integration of GO in a latex structure followed by in situ reduction at low temperature (<200°C) to obtain conductive composites.

6.2 Preliminary test on GO and rGO to test KPFM sensitivity

KPFM was performed on a sample containing an interface between GO and rGO to determine the sensitivity of KPFM to these chemical changes. KFM has been already used in different set-ups for the determination of the location of successfully reduced areas in rGO samples [197]. While the GO by itself has low conductivity, with a proper set up it is possible to deposit an area small enough to be sufficiently close to the electric contact leading to the ground, to be measured by the system. In this sample, the electrical pathway to the ground was obtained by carefully contacting the area with silver paint.

Interestingly through close examination of the micrograph of **fig. 6.1 (a)**, we cannot observe any evident difference between the reduced and the not reduced area on the topography map. The oxygenic groups defining the area with only GO are too small to be perceived with the sensitivity of the AFM tip. However, on the KPFM channel the difference is immediately visible, **fig. 6.1 (b)**, with two clearly different areas of measured CPD, here converted to work function values after calibration of the tip on top of freshly

cleaved HOPG. The difference in work function is very limited but very homogeneous on all the basal plane for both areas, giving significance to that step. When the rGO became conductive after the reduction, it also became susceptible to the p-doping from the underlying silica substrate, which may help justifying the lower than expected value of rGO as previously established in literature, at around 5 eV [198]. On **fig. 6.1 (c)** a typical line section of the data has been plotted to show the step between the two different areas, showing also where the expected interface is located, showing an increase of work function value due the local electrical interaction between GO and rGO.

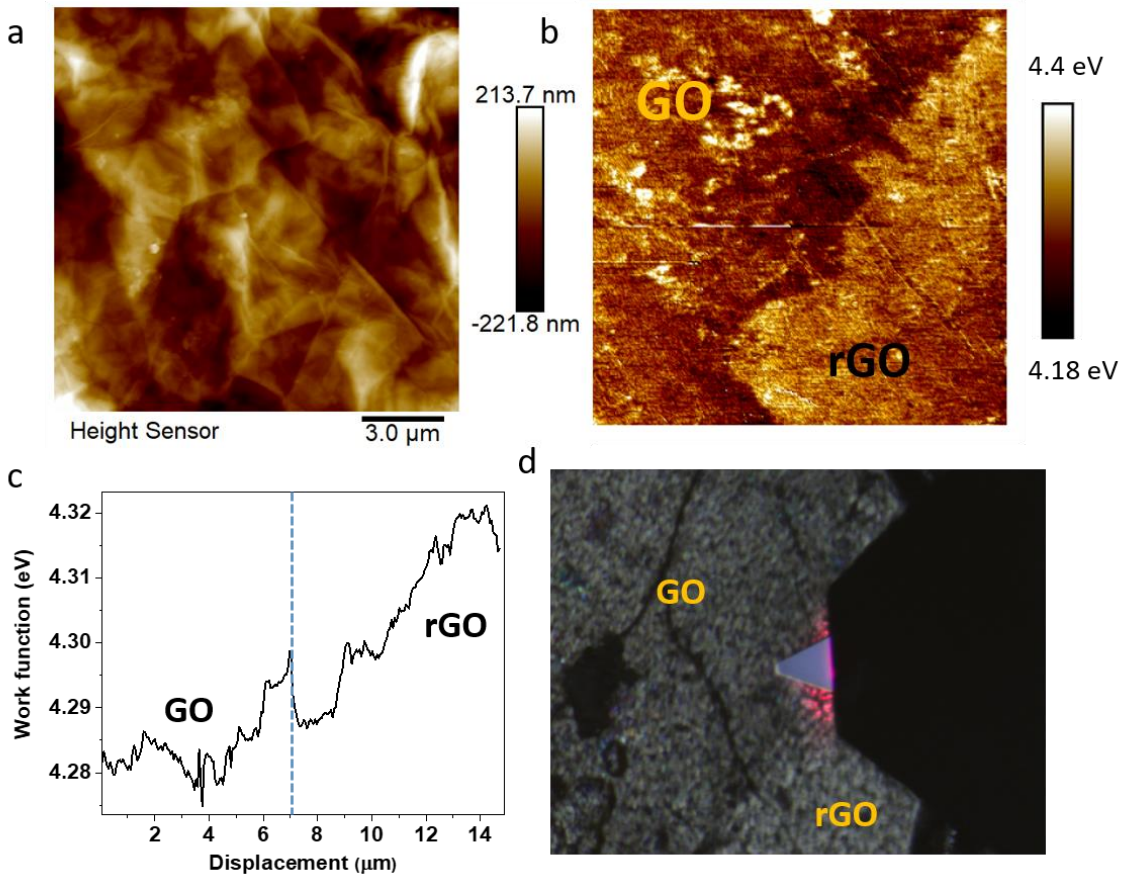

***Figure 6.1 KPFM characterization of GO-rGO interface**. **(a)** Topography data of the interface area, no clear distinction between the two conditions, that instead **(b)** is immediately visible on the KPFM channel. In **(c)** it is represented the average profile line on the KPFM data showing the degree of distinction in the work function values between the two zones. In **(d)** it is shown that the two areas are discernible with the AFM microscope*

Since it was deposited on glass, a non-conductive substrate, the measurement was also influenced by being contacted to the ground only on the sample borders, giving a value that was probably averaged at the interface by the surrounding area, which may help explain the smaller than expected signal difference. The use of glass was chosen to help the localization of the interface, which due to the change in colour after the reduction was visible as shown in **fig. 6.1 (d)**. Based on these results, KPFM cannot be used in complex systems to directly discern between the two states of GO, but it will be shown to be very helpful to localize and verify the presence of conductive elements in the latex matrix.

6.3 Composite analyses and discussion

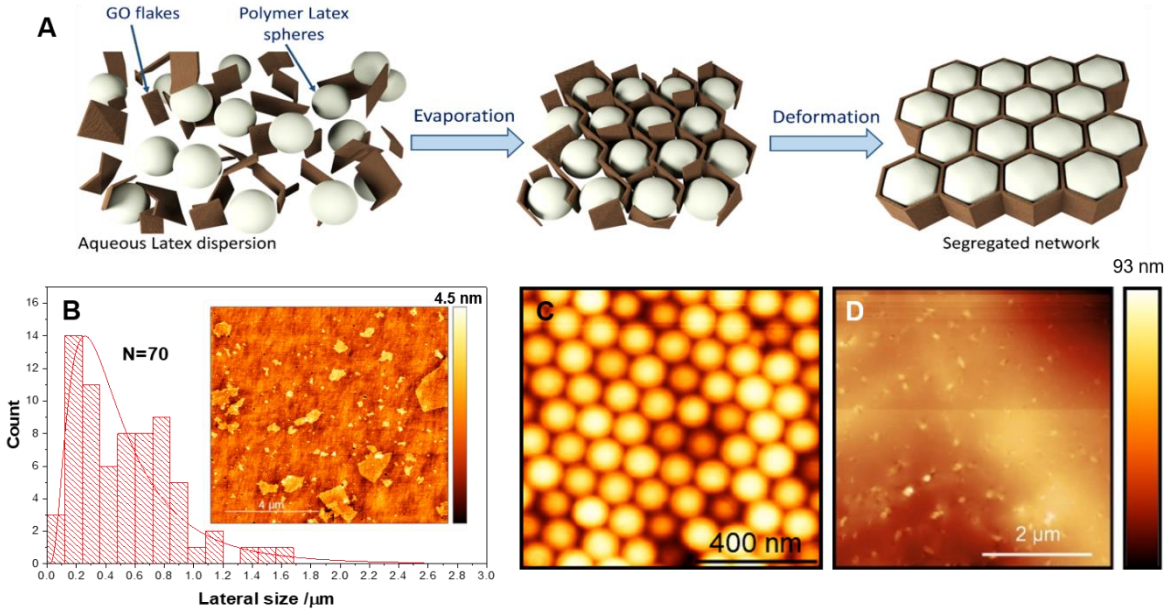

***Figure 6.2 Latex creation and characterization**. **(a)** A schematic illustration of the formation of segregated networks. **(b)** Particle size distribution of GO and AFM image in topography of GO flakes. **(c)** AFM image in topography for the PL/GO at 2 wt%. **(d)** AFM image in topography for PL/rGO at 2 wt%.*

The matrix latex is a random copolymer of methyl methacrylate (MMA), butyl acrylate (BA) and methacrylic acid (MAA), with a fairly low glass transition temperature at 20°C,

but with the spheres stable in their shape up to 200°C. This copolymer is dispersed in an aqueous solution and directly mixed with the GO dispersion, remaining stable for long time for storing purposes. Samples were prepared by depositing a layer of the solution on top of the target substrate, which was either a glass slide or a freestanding mould. Such obtained samples were then left to dry for the necessary time in ambient condition and then treated at different temperatures in the vacuum oven to test the optimal temperature for the GO to rGO in situ reduction.

In **fig. 6.2 (A)** a brief schematic of the process is represented, with the flakes and the beads mixing in the solution when deposited on the substrate, followed by a process of packing of the latex structure due to surface tension and capillary forces. These forces push the GO at the interstitial spaces in between the spheres, allowing the creation of a connected network if the process is slow enough to allow such reorganization, hence the ambient condition maintained during the day long drying process. This slow process is necessary for the polymer spheres to first arrange in an orderly way, so that each polymer bead surrounded in the plane by six others. When the amount of aqueous solution is reduced, strong capillary forces created by the evaporating solution compress the beads, deforming the original round shape into rhombic dodecahedra appearing as a honeycomb structure on the surface.

If this is achieved, the nanomaterial will reach the highest possible packing density and the consequent interconnection between GO particles will form a segregated network. To make this happen, the GO particles need to be sufficiently small and/or flexible enough to occupy the interstitial spaces, but not so small as to increase the contribution of flake-to-flake junction resistance. The GO flakes, as prepared for this study, were deposited on an ultra-smooth silicon substrate for thickness and lateral size AFM characterization. The

thickness was surprisingly uniform, confirming the advantages of using GO as a starting material to guarantee an abundance of monolayers, and measured at around 1.51 nm.

Instead, lateral size had a broader distribution but still distributed between 200 nm and 1 µm, which, considering the nominal diameter scale of the beads at around 100 nm to 200 nm, it is ideal for integration in the latex structure. The distribution is plotted in **fig. 6.2 (B)** and it was obtained by imaging multiple areas of the sample till 70 flakes were counted and measured. Once completely dried, the sample was characterized again with the AFM, and, as visible in **fig. 6.2 (C)**, it is shown the formation of the highly packed structure, with the beads organizing in a honeycomb structure. After the thermal treatment in vacuum oven at 150°C, the structure is completely coalesced and when characterized with the AFM, **fig. 6.2 (D)**, it appears as a uniform surface but for some emerging features emerging from the surface.

These features represent the modified GO flakes, now in this state reduced to rGO flakes that are preserved in a somewhat organized way confirming the presence of the segregated network in the PL/GO structure. The resulting samples were then characterized electrically, measuring the conductivity at different loading levels of relative weight percent between the two starting solutions, to find at what concentration of GO the resulting PL structure started to be conductive. The results are plotted in **fig. 6.3 (A)**, where the minimal amount necessary to obtain a conductive sample was established at around 0.5 wt.%, and then conductivity slightly increased until 2 wt.%, which was then used as an optimal value for subsequent characterizations. In the inset, three pictures represent the changes of colours of sample from immediately deposited, then completely dried and finally completely black once reduced.

Also, a picture of a device connected to the composite show that it is conductive enough at the macroscale to allow the passage of current necessary to keep the LED turned on. This type of trend, with a well-defined threshold, is typical of the percolation theory, which explains how conductivity does not proceed in a linear trend proportional to the amount of material, but jumps immediately to an almost optimal value once the interconnection of all the conductive components inside the structure is guaranteed [199].

The general equation explaining this conductivity scaling is:

$$\sigma = \sigma_{\mathrm{PL}} + \sigma_0 \, (\phi - \phi_{\mathrm{c}})^t \qquad \text{for} \quad \phi > \phi_c \tag{6.1}$$

Where σ is the conductivity of the composite, σ_{PL} is the conductivity of the matrix polymer, σ_0 is a proportionality constant (which scales with the conductivity of the filler), *t* is the critical exponent, ϕ and ϕ_c are the weight percent of the filler and the percolation threshold concentration characteristic of it, respectively.

The high conductivity obtained (>10^3 S/m) shows that the combination of PL/GO is a very good match, allowing the creation of a well-structured and interconnected segregated network with a very small amount of material. Fitting the conductivity data with the previous equation, the value of ϕ_{c} is around 0.4 wt%, which is in good agreement with theoretical value that can be found in literature for particles of similar shape and aspect ratio [200], [201]. The value of the critical exponent $t \approx 0.7$, which represents the rate at which the conductivity saturates above the percolation threshold, is lower than expected from standard percolation theory. This suggests a system where the particles are spatially correlated, like in aggregation-based systems or growing networks, with a resulting composite following what has been defined as explosive percolation [202], [203].

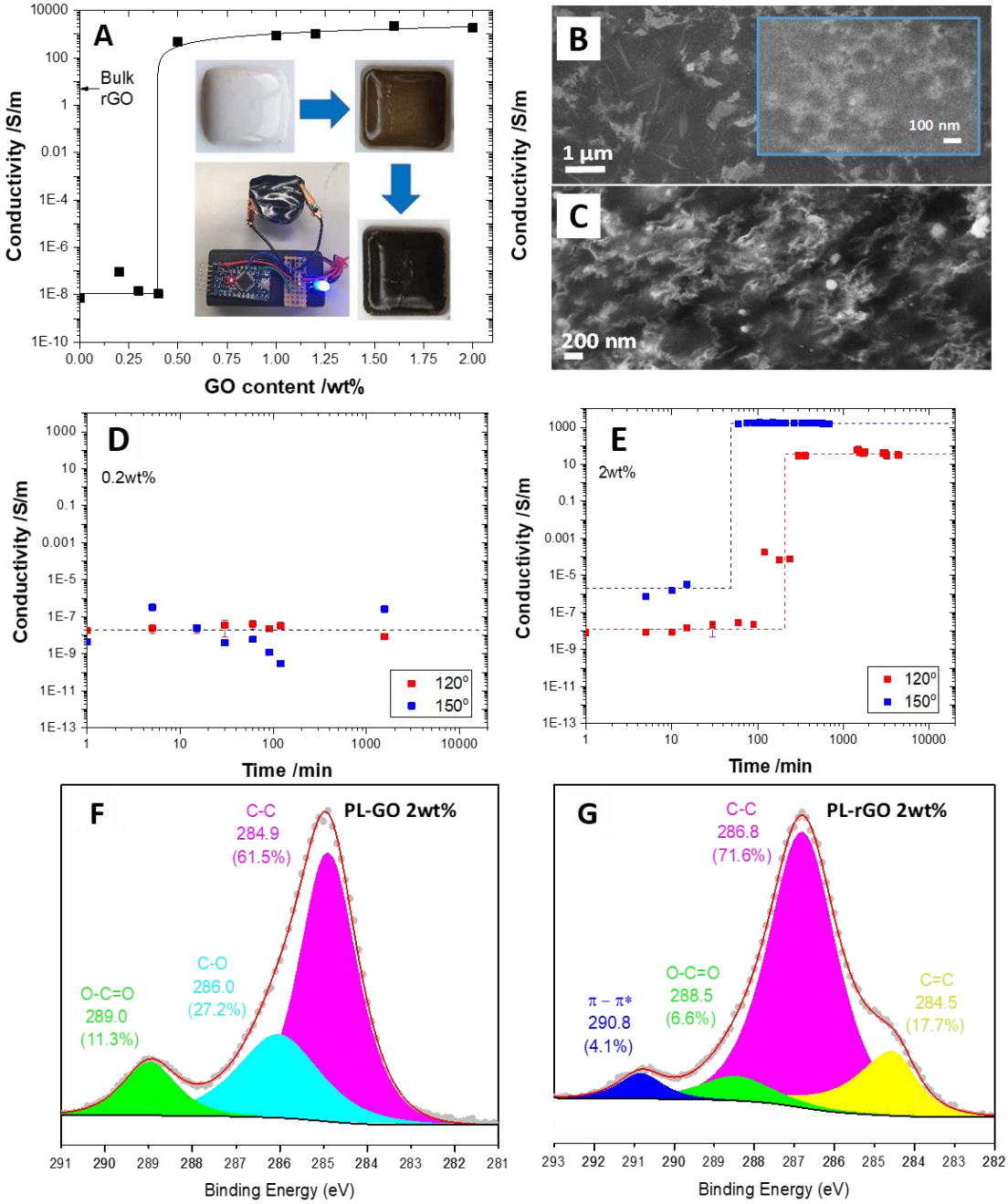

Figure 6.3 Electrical and XPS characterization of the final composite. *(a) Plot of the composite electrical properties based on the weight percent of starting GO, showing the minimal amount necessary to obtain very high conductivity. In the inset, are pictured the very clear colour changes after the deposition, drying and reduction step. A device showing conduction over all the bulk material is also pictured. In (b) and (c) SEM pictures present the distribution of the material at higher magnification, showing locally in the inset of (b) how it may still be centred on the remaining spheres structure, but overall even though not as well organized, still present high density and distribution. In (d) and (e) two examples of the trend of conductivity of the sample over time during the reduction process are shown, showing no conduction under the percolation threshold, and a sharp increase instead when the weight% is sufficiently high. In (f) and (g) pre and post reduction XPS analyses has been plotted, indicating that changes happen probably not only on the GO, but also on the surrounding polymeric structure.*

A possible theory explaining such results may come from the consideration of the nature of the reduction process, that as established in the introduction is a strongly exothermic process, which may locally influence the polymer and help the propagation of the reaction when the necessary threshold is reached. In **fig 6.3 (B)** and **fig 6.3 (C)** different magnification of SEM images from the reduced sample are shown. At a higher magnification, only the larger flakes are visible, and they appear not as organized as one would expect from a latex derived distribution. However an increased magnification, we can find both smaller arrangements that still follow the original honeycomb structure like in the **inset of fig 6.3 (B)**. More generally, **fig. 6.3 (C)** shows that a highly interconnected structure is present at a smaller scale and pervasive in the entire composite, suggesting that while the honeycomb structure is not generally preserved, the confinement of the flakes is still present at very small scale allowing the flow of current. Two examples of how this conductivity emerge are represented in **fig 6.3 (D)** and **fig 6.3 (E)**.

These graphs are obtained by plotting the measured conductivity of the sample throughout the heating process, using two different oven temperature, 120°C and 150°C respectively. In **fig. 6.3 (D)** a condition below the percolation threshold, 0.2 wt%, is represented, showing no increase in the conductivity of the sample compared to the standard and extremely low conductivity of the polymer. In **fig 6.3 (E)** instead the optimal condition, 2wt%, is plotted showing the dependence of the final conductivity based on the temperature used. The interesting factor is the incredibly sharp step from non-conductive to a value that is almost immediately the highest possible one, giving strength to the hypothesis of an explosive percolation behaviour. The position of the percolation threshold seems also to be dependent from the reduction temperature. At higher temperatures, the percolation happens sooner indicating the role of temperature in promoting the reduction and at the same time the role of the reduction process itself in

changing the internal structure of the composite to promote the formation of the segregated network.

To further explore the differences before and after reduction, XPS has been performed before and after reduction, **fig 6.3 (F)** and **fig 6.3 (G)** respectively. A new C=C sp^2 component arises in the reduced sample and another component appears at 290.8 eV ascribable to π–π^* shakeup of aromatic sp^2 carbons. Furthermore, the sp^3 carbon component (now at 1.8 eV higher than its precursor sample), is compatible with aliphatic carbon bonds in benzene-containing polymers. Indeed, the signals are perfectly compatible with the equivalent carbons in polyethylene terephthalate (PET) polymers [204], [205]. This strongly suggests that the reduction of the GO induces an aromatization of the matrix polymer, which could explain the high conductivity of the composites. The formation of this aromatised material is not observed in pristine polymer samples undergoing the same treatment, and rGO produced without the presence of the polymer is not as conductive as the composites, pointing to a strongly synergistic effect between both elements.

6.4 KPFM characterization of the final composite

To better investigate the distribution and behaviour of the conductive elements in the structure, a different preparation technique was employed. The latex and a higher concentration of GO than the one used for the bulk study were spin coated one after the other to obtain a very thin and homogeneously distributed dispersion on top of the glass substrate. Same steps as previously described followed, consisting of a drying step in

ambient conditions and then the thermal treatment at 150°C in the vacuum oven to reduce the GO.

The sample was characterized with KPFM before and after reduction, to see if we could gain any insight of the distribution of the conductive elements and/or if the sample was conductive enough from the exposed face to the bottom to even operate the imaging. The necessity of spin-coating to obtain a thin sample was directly linked to the necessity of limiting the amount of non-conductive material that could hinder the KPFM analyses. The sample was grounded to the metallic base of the AFM with the use of silver paint.

On **fig 6.4 (A)** and **fig**. **6.4 (B)** are represented the topography and the potential map for the untreated but fully dry sample. The topography clearly shows the honeycomb structure that is expected from a fully compressed and organized network, with some particles forced at the interstitial areas in between the spheres. The resulting KPFM map instead show a very noisy and not readable data, with an average value representing the average CPD between generic polymeric materials and the silicon tip. Once the sample has been reduced, some interesting features arise from the AFM characterization: the topography, **fig. 6.4 (C)**, and the potential, **fig. 6.4 (B)**, map for the reduced sample clearly show some point like features of different height and potential from the baseline.

In the topography map, two types of features are easily discernible from the otherwise well coalesced and flat surface: a series of small depression evenly distributed around the sample, and some higher, bigger features breaking through the polymeric surface up to 10-20 nm, highlighted by the red circles. This is consistent with the expected distribution of the flake size of the starting GO particles, with some few micron size particles and the majority much smaller, in particular, the bigger flakes in this sample seem to be vertically oriented, probably trapped in this position during the drying process.

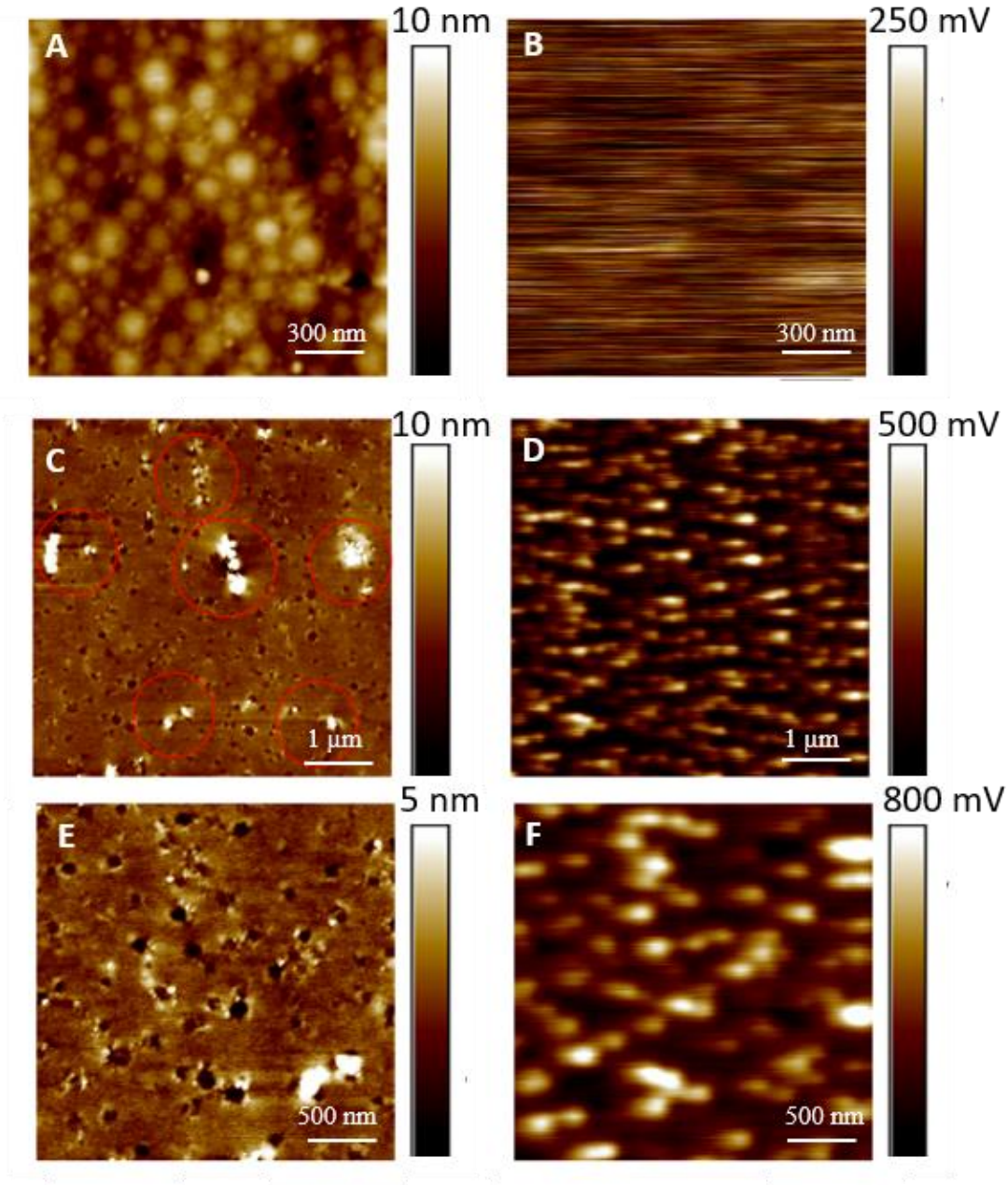

Figure 6.4 KPFM imaging of the starting composite and the reduced one. *(a) and (b) height and CPD data respectively for the not reduced sample, showing the honeycomb structure segregating residuals in the interstitial space in the height channel, and a very noisy signal in the CPS channel due to the lack of conductivity throughout the sample, hindering the collection of KPFM data. In (c) we can observe how the structure is fully coalesced in the reduced sample, showing two type of feature: small depressions and higher structure emerging from the polymer. In (d) we can observe how these features have a very strong signal suggesting they are strongly connected to the conductive segregated network. In (e) and (f) a higher resolution map of this area has been imaged, showing the direct correlation between holes and the strong signal, even higher than the one coming from the bigger emerging flakes, suggesting they are either not fully reduced or less connected to the conductive network.*

In the KPFM map, these two features present a much higher CPD, indicating their conductive nature and connection to the ground through the underlying segregated network. While for the higher features it is immediate, the association to the rGO flakes, for the other point like features, some higher resolution is necessary to be sure that they correlate with the smaller depression of the surface.

In **fig. 6.4 (E)** and **fig. 6.4 (F)** a smaller area featuring both types of elements was further analysed with high resolution KPFM for such purpose. The first thing to note is that the small holes, with an average lateral size of 100 nm or less, don't seem to be randomly distributed, following some general lines or appearing to be distributed around some central areas. This would suggest that they are formed around the area previously occupied by the spheres before the reduction and the resulting homogenisation of the whole polymeric structure. In the CPD map, it is immediately apparent that these small holes are the one either with the stronger signal, suggesting that at the bottom of the depression the rGO nanoparticles are exposed or immediately underneath the surface.

The distribution of values, and the appearance of high CPD point even in areas not presenting clearly visible features, suggests that these values are proportional to the distance from the surface of the rGO clusters with high enough density to generate the signal, as found in previous studies using other nanomaterials like carbon nanotube in composite structures [206]. KPFM is a strictly surface-sensitive characterization technique, which is normally not able to image the effects happening more than few nanometres under the surface. Nevertheless, considering the established modification of the polymer by the exothermal reduction of GO, it is possible that some parts of the latex structure, if close enough to underlying clusters, may have been modified enough to change their work function.

As a last consideration, it is interesting to notice how the bigger and visible flakes, creating the exposed and taller features, appear to have a weaker CPD than the holes, even though they are closer to the scanning tip. This would suggest two things: either that this bigger flakes are not completely reduced at the temperature that instead fully reduced the remaining nanoparticles, or that this bigger flakes are not as well integrated with the rest of segregated network, posing as a less favourable pathway for the electron movements.

Finally, even though values are consistent and high enough in value to suggest otherwise, to verify that these values are not just dependent from cross-channel correlation artefacts during the measuring process, some profile section are represented in **fig. 6.5 (A)**. These type of artefacts arise when the tip, while scanning on the interleave step on top of the surface while following the previously measured topography, has to compensate sharp change in height due to cliffs or taller features to keep the same height difference between sample and tip. These movements introduce some noise due to the rapid movement itself, plus an increase in signal due to the effects of the tips feeling not only the CPD of the point immediately underneath the tip, but also the effect of the lateral tall or deep structures that the system is compensating for. This is a typical limitation of high resolution KPFM, which needs a surface as flat and smooth as possible to be properly operated.

Finally, to have some other confirmation on the possible distribution of the flakes in the structure, SEM images were obtained for the reduced sample, **fig. 6.5 (B)** and **fig. 6.5 (C)**. It is immediately visible how these holes, just few nanometres deep, could not explain such big difference in the CPD value, particularly considering how the measurement was operated at a 40 nm height set point, an order of magnitude higher than their scale.

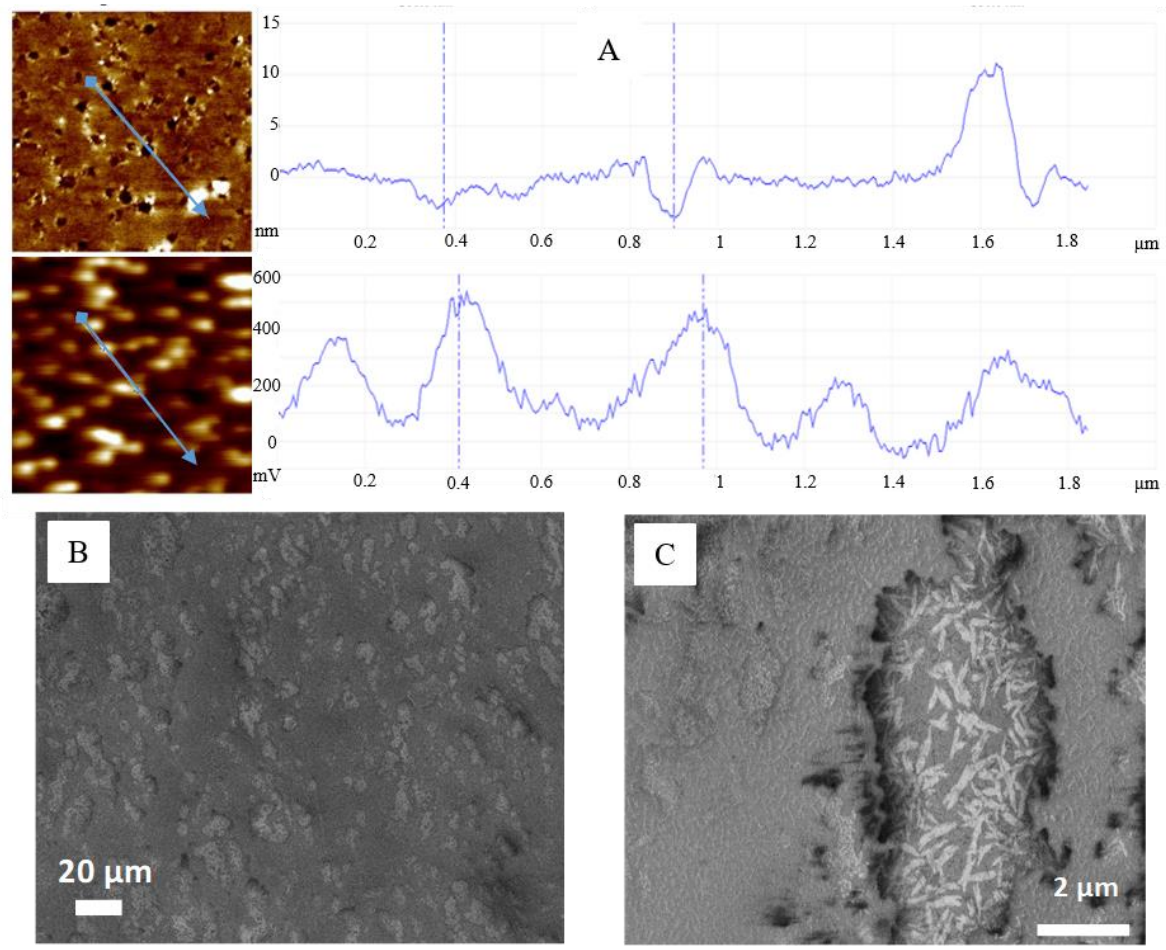

Figure 5 Line profile of the reduced composite and SEM characterization of the reduced composite. *(a) Line profile of the AFM height data on top and CPD data on the bottom for the same line, proving how the strong signal shown on the CPD map cannot be justified by cross correlation with the height channel, which shows just few nm deep holes. In (b) and (c) different magnification of the composite are presented, showing the flakes distribution in the sample, with smaller flakes homogeneously distributed in the surface and a bottom layer where most of the bigger flakes are deposited.*

Furthermore, this line profile confirms that the higher features present a weaker signal, probably for the reasons described before. At a very low magnification, the sample presents itself as clearly formed by two different phases, one homogeneous on top and another rougher immediately underneath. At a higher magnification, closer to the scale which has been probed with the KPFM, some larger holes are created in the first layer, revealing an internal structure formed by a mix of coalesced polymer and the biggest flakes. This is unavoidable since even at very low voltages the structure appears very

susceptible to be destroyed, rendering higher magnification and hence energy densities impossible.

Nonetheless, already at this scale apart from the larger hole it is possible to observe how the surrounding first layer appears very rough and covered by a somewhat organized distribution of all the smaller flakes, which as we expected from the KPFM data are close enough to the surface to become visible at the SEM. The consistency between the apparent scale of these features on the surface of the sample, coupled with the not random distribution as seen in the AFM data, suggest that the KPFM data was actually picking up the electrical effect of the conductive nanoparticles of rGO in the latex structure.

6.5 Conclusions

Bringing the amazing properties of nanomaterials to real world applications requires reliable synthesis, processes, storing solutions that keep the as synthesised material properties for long time, standardized characterization techniques and the possibility of easily combine the nanomaterials with industrial processes and cheap materials. In this study, to overcome the limitation arising from the use of pure graphene, GO has been employed and successfully shown to be easily integrated with cheap polymer latex materials to obtain stable composites. The use of this technique has become more and more popular due to its ability to greatly limit the total amount of nanomaterial necessary to transfer the properties to the whole composite, allowing the creation of a highly interconnected and organized segregate network.

These composites have also been proved to be highly conductive after a simple thermal treatment to reduce in situ the GO. Throughout the process, AFM and KPFM characterization has been employed to gain insight on the properties of the starting GO and how it is distributed in the reduced composite. While more studies will be necessary to fully understand how the polymeric structure reacts to the exothermic reduction reaction, the ending results present a well-integrated conductive material with homogeneous electrical property all over the composite. As shown by the KPFM characterization, conductive conglomerate have a very strong signal suggesting a very good connection to the ground and homogeneous distribution. Future applications requiring flexible conductive material will find this type of composite extremely helpful, thanks to how easy they are to produce and their long-time stability.

Summary and Conclusions

In this work, I have demonstrated three very different applications of the KPFM technique in the field of the characterization of 2D materials and their composites.

As acknowledged in the first chapter, the KPFM technique is greatly limited in its ability to accurately obtain absolute work function values or to quantitatively measure the effect of doping at different interfaces, especially in air conditions, without a proper clean room and vacuum set-up. Therefore, this technique has found use mainly in the electronics field and in highly controlled studies led by theory on basic properties of 2D materials.

In this work, I have shown how, accepting these limitations and always coupling this technique with other characterization tools, it is possible to still use this technique to gain qualitative information on the analysed substrate even in the absence of clean room conditions. In chapter 3, I have shown how even for liquid-exfoliated materials, where edge effect and surrounding environment effects affect the measurement, it is possible to obtain similar trend to that of other studies in literature analysing the height/CPD relationship of 2D materials. In chapter 4, I have presented our published work about the creation of graphene 3D structure by thermal excitation, where my KPFM data has been a valuable tool from the start to identify this structure and to identify qualitatively how they are distinguished from other 3D structures like nanobubbles in the same type of substrate. In chapter 5, following previous published results from our group, I have shown how KPFM can be a fundamental tool to prove the nature of the electrical contact between graphene and silver nanowires, which represent a type of hybrid of great interest for transparent electrode applications like touch screens. Finally, in chapter 6 I have shown how KPFM can be employed even in the analysis of bulk composites, demonstrating how

the successful detection of the signal depending from a well-grounded and conductive sample can be exploited to confirm local surface connection to the segregated conductive network of reduced graphene oxide in a latex structure after thermal treatment, with the results submitted for publication.

Furthermore, KPFM can also give a good representation of how the conductive elements are distributed on and immediately under the surface of the composite. All these applications span from the most basic and theoretical to the closest to real life applications. Considering the constant improvement of the algorithms piloting the KPFM tip, with the results of increased sensitivity and noise removal, coupled with new modules allowing the capture of increased amount of data in a single pass and at higher frequencies, the future of this technique is very promising. With the increasing number of applications using 2D materials, and with the measurement of their work function being a critical property to understand particularly for electronic applications, KPFM will be more and more employed as a generic tool for quality control and as a standardization tool.

The use of KPFM for quantitative, reliable and repeatable characterization of nanomaterials today requires highly controlled environments to reduce to a minimum unwanted amount of contaminant and ambient condition affecting the tip-sample electrical interaction, and further effort will need to be put into fundamental studies to model these parameters affecting CPD measurements. Still, this works has established that even with just a general understanding of the main principles governing this technique, a great amount of useful data for a wide ranging of applications in environmental conditions can be obtained.

Bibliography

[1] M. Nonnenmacher, M. P. O'Boyle, and H. K. Wickramasinghe, "Kelvin probe force microscopy," *Appl. Phys. Lett.*, vol. 58, no. 25, pp. 2921–2923, 1991, doi: 10.1063/1.105227.

[2] N. A. Surplice and R. J. D'Arcy, "A critique of the Kelvin method of measuring work functions," *Journal of Physics E: Scientific Instruments*, vol. 3, no. 7. IOP Publishing, pp. 477–482, Jul-1970, doi: 10.1088/0022-3735/3/7/201.

[3] M. Nonnenmacher, M. O'Boyle, and H. K. Wickramasinghe, "Surface investigations with a Kelvin probe force microscope," *Ultramicroscopy*, vol. 42–44, no. PART 1, pp. 268–273, 1992, doi: 10.1016/0304-3991(92)90278-R.

[4] C. Sommerhalter, T. W. Matthes, T. Glatzel, A. Jäger-Waldau, and M. C. Lux-Steiner, "High-sensitivity quantitative Kelvin probe microscopy by noncontact ultra-high-vacuum atomic force microscopy," *Appl. Phys. Lett.*, vol. 75, no. 2, pp. 286–288, 1999, doi: 10.1063/1.124357.

[5] S. Sadewasser, T. Glatzel, R. Shikler, Y. Rosenwaks, and M. C. Lux-Steiner, "Resolution of Kelvin probe force microscopy in ultrahigh vacuum: Comparison of experiment and simulation," *Appl. Surf. Sci.*, vol. 210, no. 1-2 SPEC., pp. 32–36, 2003, doi: 10.1016/S0169-4332(02)01475-7.

[6] O. Vatel and M. Tanimoto, "Kelvin probe force microscopy for potential distribution measurement of semiconductor devices," *J. Appl. Phys.*, vol. 77, no. 6, pp. 2358–2362, 1995, doi: 10.1063/1.358758.

[7] "AFM Probes | AFM Cantilever | AFM Tips - Bruker AFM Probes," 2019. [Online]. Available: https://www.brukerafmprobes.com/.

[8] A. Kikukawa, S. Hosaka, and R. Imura, "Silicon pn junction imaging and characterizations using sensitivity enhanced Kelvin probe force microscopy," *Appl. Phys. Lett.*, vol. 66, no. April 1995, pp. 3510–3512, 1995, doi: 10.1063/1.113780.

[9] W. Melitz, J. Shen, A. C. Kummel, and S. Lee, "Kelvin probe force microscopy and its application," *Surface Science Reports*, vol. 66, no. 1. Elsevier B.V., pp. 1–27, 2011, doi: 10.1016/j.surfrep.2010.10.001.

[10] K. Okamoto, Y. Sugawara, and S. Morita, "The elimination of the 'artifact' in the electrostatic force measurement using a novel noncontact atomic force microscope/electrostatic force microscope," *Appl. Surf. Sci.*, vol. 188, no. 3–4, pp. 381–385, 2002, doi: 10.1016/S0169-4332(01)00953-9.

[11] T. Glatzel, A. Jäger-Waldau, M. C. Lux-Steiner, C. Sommerhalter, and T. W. Matthes, "Kelvin probe force microscopy in ultra high vacuum using amplitude modulation detection of the electrostatic forces," *Appl. Surf. Sci.*, vol. 157, no. 4, pp. 263–268, 2000, doi: 10.1016/S0169-4332(99)00537-1.

[12] S. Sadewasser *et al.*, "New insights on atomic-Resolution frequency-Modulation kelvin-Probe force-Microscopy imaging of semiconductors," *Phys. Rev. Lett.*, vol. 103, no. 26, pp. 5–8, 2009, doi: 10.1103/PhysRevLett.103.266103.

[13] A. Kikukawa, S. Hosaka, and R. Imura, "Vacuum compatible high-sensitive

Kelvin probe force microscopy," *Rev. Sci. Instrum.*, vol. 67, no. 4, pp. 1463–1467, 1996, doi: 10.1063/1.1146874.

[14] T. Glatzel, S. Sadewasser, and M. C. Lux-Steiner, "Amplitude or frequency modulation-detection in Kelvin probe force microscopy," *Appl. Surf. Sci.*, vol. 210, no. 1-2 SPEC., pp. 84–89, 2003, doi: 10.1016/S0169-4332(02)01484-8.

[15] M. P. O'Boyle, T. T. Hwang, and H. K. Wickramasinghe, "Atomic force microscopy of work functions on the nanometer scale," *Appl. Phys. Lett.*, vol. 74, no. 18, pp. 2641–2642, 1999, doi: 10.1063/1.123923.

[16] G. H. Buh, H. J. Chung, C. K. Kim, J. H. Yi, I. T. Yoon, and Y. Kuk, "Imaging of a silicon pn junction under applied bias with scanning capacitance microscopy and Kelvin probe force microscopy," *Appl. Phys. Lett.*, vol. 77, no. 1, pp. 106–108, 2000, doi: 10.1063/1.126892.

[17] Y. Rosenwaks, R. Shikler, T. Glatzel, and S. Sadewasser, "Kelvin probe force microscopy of semiconductor surface defects," *Phys. Rev. B - Condens. Matter Mater. Phys.*, vol. 70, no. 8, pp. 1–7, 2004, doi: 10.1103/PhysRevB.70.085320.

[18] K. P. Puntambekar, P. V. Pesavento, and C. D. Frisbie, "Surface potential profiling and contact resistance measurements on operating pentacene thin-film transistors by Kelvin probe force microscopy," *Appl. Phys. Lett.*, vol. 83, no. 26, pp. 5539–5541, 2003, doi: 10.1063/1.1637443.

[19] A. Doukkali, S. Ledain, C. Guasch, and J. Bonnet, "Surface potential mapping of biased pn junction with kelvin probe force microscopy: Application to cross-section devices," *Appl. Surf. Sci.*, vol. 235, no. 4, pp. 507–512, 2004, doi: 10.1016/j.apsusc.2004.03.249.

[20] M. Ligowski, D. Moraru, M. Anwar, T. Mizuno, R. Jablonski, and M. Tabe, "Observation of individual dopants in a thin silicon layer by low temperature Kelvin Probe Force Microscope," *Appl. Phys. Lett.*, vol. 93, no. 14, pp. 1–4, 2008, doi: 10.1063/1.2992202.

[21] M. Rohwerder and F. Turcu, "High-resolution Kelvin probe microscopy in corrosion science: Scanning Kelvin probe force microscopy (SKPFM) versus classical scanning Kelvin probe (SKP)," *Electrochim. Acta*, vol. 53, no. 2, pp. 290–299, 2007, doi: 10.1016/j.electacta.2007.03.016.

[22] U. Zerweck, C. Loppacher, T. Otto, S. Grafström, and L. M. Eng, "Accuracy and resolution limits of Kelvin probe force microscopy," *Phys. Rev. B - Condens. Matter Mater. Phys.*, vol. 71, no. 12, pp. 1–9, 2005, doi: 10.1103/PhysRevB.71.125424.

[23] D. Ziegler and A. Stemmer, "Force gradient sensitive detection in lift-mode Kelvin probe force microscopy," *Nanotechnology*, vol. 22, no. 7, 2011, doi: 10.1088/0957-4484/22/7/075501.

[24] H. O. Jacobs, P. Leuchtmann, O. J. Homan, and A. Stemmer, "Resolution and contrast in Kelvin probe force microscopy," *J. Appl. Phys.*, vol. 84, no. 3, pp. 1168–1173, 1998, doi: 10.1063/1.368181.

[25] J. Colchero, A. Gil, and A. M. Baró, "Resolution enhancement and improved data interpretation in electrostatic force microscopy," *Phys. Rev. B - Condens.*

Matter Mater. Phys., vol. 64, no. 24, pp. 1–11, 2001, doi: 10.1103/PhysRevB.64.245403.

[26] A. Gil, J. Colchero, J. Gómez-Herrero, and A. M. Baró, "Electrostatic force gradient signal: Resolution enhancement in electrostatic force microscopy and improved Kelvin probe microscopy," *Nanotechnology*, vol. 14, no. 2, pp. 332–340, 2003, doi: 10.1088/0957-4484/14/2/345.

[27] T. Takahashi and S. Ono, "Tip-to-sample distance dependence of an electrostatic force in KFM measurements," *Ultramicroscopy*, vol. 100, no. 3–4, pp. 287–292, 2004, doi: 10.1016/j.ultramic.2004.01.017.

[28] L. Nony, F. Bocquet, C. Loppacher, and T. Glatzel, "On the relevance of the atomic-scale contact potential difference by amplitude-modulation and frequency-modulation kelvin probe force microscopy," *Nanotechnology*, vol. 20, no. 26, 2009, doi: 10.1088/0957-4484/20/26/264014.

[29] "PFQNE-AL - Bruker AFM Probes," 2019. [Online]. Available: https://www.brukerafmprobes.com/p-3817-pfqne-al.aspx.

[30] "SCM-PIC-V2 - Bruker AFM Probes," 2019. [Online]. Available: https://www.brukerafmprobes.com/Product.aspx?ProductID=3951.

[31] H. O. Jacobs, H. F. Knapp, and A. Stemmer, "Practical aspects of Kelvin probe force microscopy," *Rev. Sci. Instrum.*, vol. 70, no. 3, pp. 1756–1760, 1999, doi: 10.1063/1.1149664.

[32] H. Sugimura, Y. Ishida, K. Hayashi, O. Takai, and N. Nakagiri, "Potential shielding by the surface water layer in Kelvin probe force microscopy," *Appl. Phys. Lett.*, vol. 80, no. 8, pp. 1459–1461, 2002, doi: 10.1063/1.1455145.

[33] V. Palermo, K. Müllen, and P. Samorì, "Tip− Sample Interactions in Kelvin Probe Force Microscopy: Quantitative …," *J. Phys. …*, pp. 17368–17377, 2008.

[34] V. Palermo, M. Palma, and P. Samori, "Electronic characterization of organic thin films by Kelvin probe force microscopy," *Adv. Mater.*, vol. 18, no. 2, pp. 145–164, 2006, doi: 10.1002/adma.200501394.

[35] A. Liscio, V. Palermo, and P. Samorì, "Nanoscale quantitative measurement of the potential of charged nanostructures by electrostatic and Kelvin probe force microscopy: Unraveling electronic processes in complex materials," *Acc. Chem. Res.*, vol. 43, no. 4, pp. 541–550, 2010, doi: 10.1021/ar900247p.

[36] C. Barth *et al.*, "AFM tip characterization by Kelvin probe force microscopy," *New J. Phys.*, vol. 12, 2010, doi: 10.1088/1367-2630/12/9/093024.

[37] F. Krok, K. Sajewicz, J. Konior, M. Goryl, P. Piatkowski, and M. Szymonski, "Lateral resolution and potential sensitivity in Kelvin probe force microscopy: Towards understanding of the sub-nanometer resolution," *Phys. Rev. B - Condens. Matter Mater. Phys.*, vol. 77, no. 23, pp. 1–9, 2008, doi: 10.1103/PhysRevB.77.235427.

[38] A. B. Cook, Z. Barrett, S. B. Lyon, H. N. McMurray, J. Walton, and G. Williams, "Calibration of the scanning Kelvin probe force microscope under controlled environmental conditions," *Electrochim. Acta*, vol. 66, pp. 100–105, 2012, doi: 10.1016/j.electacta.2012.01.054.

[39] G. Cohen *et al.*, “Reconstruction of surface potential from Kelvin probe force microscopy images,” *Nanotechnology*, vol. 24, no. 29, 2013, doi: 10.1088/0957-4484/24/29/295702.

[40] M. Mohr, J. Maultzsch, and C. Thomsen, “Splitting of the Raman 2D band of graphene subjected to strain,” *Phys. Rev. B - Condens. Matter Mater. Phys.*, vol. 82, no. 20, p. 201409, Nov. 2010, doi: 10.1103/PhysRevB.82.201409.

[41] E. Smith and G. Dent, *Modern Raman spectroscopy : a practical approach*. .

[42] M. (Michael J. . O’Connell, *Carbon nanotubes : properties and applications*. CRC/Taylor & Francis, 2006.

[43] L. M. Malard, M. A. Pimenta, G. Dresselhaus, and M. S. Dresselhaus, “Raman spectroscopy in graphene,” *Physics Reports*, vol. 473, no. 5–6. North-Holland, pp. 51–87, 01-Apr-2009, doi: 10.1016/j.physrep.2009.02.003.

[44] L. Reimer, *Scanning electron microscopy : physics of image formation and microanalysis*. Springer-Verlag, 1985.

[45] J. J. Bozzola and L. D. Russell, *Electron microscopy : principles and techniques for biologists*. Jones and Bartlett, 1999.

[46] N. Yao and Z. L. Wang, *Handbook of microscopy for nanotechnology*. Kluwer Academic Publishers, 2005.

[47] N. Sahu, B. Parija, S. P.-I. J. of Physics, and undefined 2009, “Fundamental understanding and modeling of spin coating process: A review,” *Springer*.

[48] M. Petty, “Langmuir-Blodgett films: an introduction,” 1996.

[49] K. GmbH, “Rings are for Fingers – Plates are for Surface Tension.”

[50] J. Brodovitch, “Chem 366-3 Page I-1 LAB MANUAL Langmuir-Blodgett Film.”

[51] A. Ulman, “An Introduction to Ultrathin Organic Films: From Langmuir--Blodgett to Self--Assembly,” 2013.

[52] M. J. Large, S. P. Ogilvie, A. A. K. King, and A. B. Dalton, “Understanding solvent spreading for langmuir deposition of nanomaterial films: A hansen solubility parameter approach,” *Langmuir*, vol. 33, no. 51, pp. 14766–14771, Dec. 2017, doi: 10.1021/acs.langmuir.7b03867.

[53] A. K. Greim, “Graphene : Status and Prospects,” *Science*, vol. 324, no. 2009, p. 1530.1534, 2014, doi: 10.1126/science.1158877.

[54] M. Ohtsu, *Progress in nano-electro-optics*. Springer, 2003.

[55] A. H. Castro Neto, F. Guinea, N. M. R. Peres, K. S. Novoselov, and A. K. Geim, “The electronic properties of graphene,” *Rev. Mod. Phys.*, vol. 81, no. 1, pp. 109–162, 2009, doi: 10.1103/RevModPhys.81.109.

[56] K. S. Novoselov, V. I. Fal’Ko, L. Colombo, P. R. Gellert, M. G. Schwab, and K. Kim, “A roadmap for graphene,” *Nature*, vol. 490, no. 7419. Nature Publishing Group, pp. 192–200, 11-Oct-2012, doi: 10.1038/nature11458.

[57] D. S. L. Abergel, V. Apalkov, J. Berashevich, K. Ziegler, and T. Chakraborty, “Properties of graphene: a theoretical perspective,” *Adv. Phys.*, vol. 59, no. 4, pp.

261–482, Jul. 2010, doi: 10.1080/00018732.2010.487978.

[58] A. K. Geim and K. S. Novoselov, “The rise of graphene.,” *Nat. Mater.*, vol. 6, no. 3, pp. 183–91, Aug. 2007, doi: 10.1038/nmat1849.

[59] X. Dong *et al.*, “One-step growth of graphene–carbon nanotube hybrid materials by chemical vapor deposition,” *Elsevier*.

[60] K. Kim *et al.*, “Large-scale pattern growth of graphene films for stretchable transparent electrodes,” *nature.com*.

[61] Y. Hernandez, V. Nicolosi, M. Lotya, … F. B.-N., and undefined 2008, “High-yield production of graphene by liquid-phase exfoliation of graphite,” *nature.com*.

[62] X. Cui, M. Freitag, R. Martel, L. Brus, and P. Avouris, “Controlling energy-level alignments at carbon nanotube/Au contacts,” *Nano Lett.*, vol. 3, no. 6, pp. 783–787, 2003, doi: 10.1021/nl034193a.

[63] V. Palermo *et al.*, “Influence of molecular order on the local work function of nanographene architectures: A Kelvin-probe force microscopy study,” *ChemPhysChem*, vol. 6, no. 11, pp. 2371–2375, 2005, doi: 10.1002/cphc.200500181.

[64] P. A. Anderson, “Work function of gold,” *Phys. Rev.*, vol. 115, no. 3, pp. 553–554, Aug. 1959, doi: 10.1103/PhysRev.115.553.

[65] T. Filleter, K. V. Emtsev, T. Seyller, and R. Bennewitz, “Local work function measurements of epitaxial graphene,” *Appl. Phys. Lett.*, vol. 93, no. 13, 2008, doi: 10.1063/1.2993341.

[66] L. Nony, A. S. Foster, F. Bocquet, and C. Loppacher, “Understanding the Atomic-Scale Contrast in Kelvin Probe Force Microscopy,” *Phys. Rev. Lett.*, vol. 103, no. 3, pp. 1–4, 2009, doi: 10.1103/PhysRevLett.103.036802.

[67] K. M. Burson *et al.*, “Direct imaging of charged impurity density in common graphene substrates,” *Nano Lett.*, vol. 13, no. 8, pp. 3576–3580, 2013, doi: 10.1021/nl4012529.

[68] N. J. Lee *et al.*, “The interlayer screening effect of graphene sheets investigated by Kelvin probe force microscopy,” *Appl. Phys. Lett.*, vol. 95, no. 22, p. 222107, Nov. 2009, doi: 10.1063/1.3269597.

[69] R. Wang, Y. Fang, X. Qiu, S. Wang, D. Zhang, and Z. Li, “Control of Carrier Type and Density in Exfoliated Graphene by Interface Engineering,” *ACS Nano*, vol. 5, no. 1, pp. 408–412, 2010, doi: 10.1021/nn102236x.

[70] X. Wang, J. Bin Xu, W. Xie, and J. Du, “Quantitative analysis of graphene doping by organic molecular charge transfer,” *J. Phys. Chem. C*, vol. 115, no. 15, pp. 7596–7602, 2011, doi: 10.1021/jp200386z.

[71] L. Yan, C. Punckt, I. A. Aksay, W. Mertin, and G. Bacher, “Local voltage drop in a single functionalized graphene sheet characterized by Kelvin probe force microscopy,” *Nano Lett.*, vol. 11, no. 9, pp. 3543–3549, 2011, doi: 10.1021/nl201070c.

[72] D. Ziegler *et al.*, “Variations in the work function of doped single- and few-layer

graphene assessed by Kelvin probe force microscopy and density functional theory," *Phys. Rev. B - Condens. Matter Mater. Phys.*, vol. 83, no. 23, pp. 1–7, 2011, doi: 10.1103/PhysRevB.83.235434.

[73] A. Liscio *et al.*, "Charge transport in graphene-polythiophene blends as studied by Kelvin Probe Force Microscopy and transistor characterization," *J. Mater. Chem.*, vol. 21, no. 9, pp. 2924–2931, 2011, doi: 10.1039/c0jm02940h.

[74] V. Panchal, R. Pearce, R. Yakimova, A. Tzalenchuk, and O. Kazakova, "Standardization of surface potential measurements of graphene domains," *Sci. Rep.*, vol. 3, no. 2, pp. 1–8, 2013, doi: 10.1038/srep02597.

[75] Y. Li, C. Y. Xu, and L. Zhen, "Surface potential and interlayer screening effects of few-layer MoS 2 nanoflakes," *Appl. Phys. Lett.*, vol. 102, no. 14, pp. 3–7, 2013, doi: 10.1063/1.4801844.

[76] J. H. Kim *et al.*, "Work function engineering of single layer graphene by irradiation-induced defects," *Appl. Phys. Lett.*, vol. 103, no. 17, 2013, doi: 10.1063/1.4826642.

[77] Q. H. Wang, K. Kalantar-Zadeh, A. Kis, J. N. Coleman, and M. S. Strano, "Electronics and optoelectronics of two-dimensional transition metal dichalcogenides," *Nature Nanotechnology*, vol. 7, no. 11. pp. 699–712, 2012, doi: 10.1038/nnano.2012.193.

[78] Z. Li and S. L. Wong, "Functionalization of 2D transition metal dichalcogenides for biomedical applications," *Mater. Sci. Eng. C*, vol. 70, pp. 1095–1106, Jan. 2017, doi: 10.1016/j.msec.2016.03.039.

[79] G. Hao *et al.*, "Electrostatic properties of few-layer MoS2 films," *AIP Adv.*, vol. 3, no. 4, 2013, doi: 10.1063/1.4802921.

[80] S. Choi, Z. Shaolin, and W. Yang, "Layer-number-dependent work function of MoS2 nanoflakes," *J. Korean Phys. Soc.*, vol. 64, no. 10, pp. 1550–1555, 2014, doi: 10.3938/jkps.64.1550.

[81] J. H. Kim, J. Lee, J. H. Kim, C. C. Hwang, C. Lee, and J. Y. Park, "Work function variation of MoS 2 atomic layers grown with chemical vapor deposition: The effects of thickness and the adsorption of water/oxygen molecules," *Appl. Phys. Lett.*, vol. 106, no. 25, 2015, doi: 10.1063/1.4923202.

[82] M. Tosun *et al.*, "MoS2 Heterojunctions by Thickness Modulation," *Sci. Rep.*, vol. 5, no. 1, pp. 1–8, 2015, doi: 10.1038/srep10990.

[83] D. Vikraman *et al.*, "Facile Synthesis of Molybdenum Diselenide Layers for High-Performance Hydrogen Evolution Electrocatalysts," *ACS Omega*, vol. 3, no. 5, pp. 5799–5807, May 2018, doi: 10.1021/acsomega.8b00459.

[84] C. Lee, X. Wei, J. W. Kysar, and J. Hone, "Measurement of the elastic properties and intrinsic strength of monolayer graphene," *Science (80-.).*, vol. 321, no. 5887, pp. 385–388, 2008, doi: 10.1126/science.1157996.

[85] A. K. Geim, "GRAPHENE: STATUS AND PROSPECTS A. K. Geim Manchester Centre for Mesoscience and Nanotechnology, University of Manchester, Oxford Road M13 9PL, Manchester, UK," *Science (80-.).*, no. 6, pp. 1–8.

[86] A. H. Castro Neto *et al.*, “Substrate-induced bandgap opening in epitaxial graphene.,” *Nat. Mater.*, vol. 6, no. 10, pp. 770–5, 2007, doi: 10.1038/nmat2003.

[87] R. J. Stöhr, R. Kolesov, K. Xia, and J. Wrachtrup, “All-Optical High-Resolution Nanopatterning and 3D Suspending of Graphene,” *ACS Nano*, vol. 5, no. 6, pp. 5141–5150, Jun. 2011, doi: 10.1021/nn201226f.

[88] B. Y. A. K. Geim and P. Kim, “Materials Carbon Wonderland,” *Scientific American*, vol. 298, no. April, Scientific American, a division of Nature America, Inc., pp. 91–97, 2008.

[89] V. Barone, O. Hod, and G. E. Scuseria, “Electronic structure and stability of semiconducting graphene nanoribbons,” *Nano Lett.*, vol. 6, no. 12, pp. 2748–2754, Dec. 2006, doi: 10.1021/nl0617033.

[90] E. O. Hall *et al.*, “Control of graphene’s properties by reversible hydrogenation,” *Science (80-.).*, no. January, pp. 610–613, 2009, doi: 10.1126/science.1167130.

[91] L. Liu *et al.*, “Graphene oxidation: Thickness-dependent etching and strong chemical doping,” *Nano Lett.*, vol. 8, no. 7, pp. 1965–1970, Jul. 2008, doi: 10.1021/nl0808684.

[92] Z. Qi, “Strain engineering of graphene,” 2015.

[93] D. B. Zhang, E. Akatyeva, and T. Dumitric, “Bending ultrathin graphene at the margins of continuum mechanics,” *Phys. Rev. Lett.*, vol. 106, no. 25, p. 255503, Jun. 2011, doi: 10.1103/PhysRevLett.106.255503.

[94] C. Metzger *et al.*, “Biaxial strain in graphene adhered to shallow depressions,” *Nano Lett.*, vol. 10, no. 1, pp. 6–10, Jan. 2010, doi: 10.1021/nl901625v.

[95] J. Zabel *et al.*, “Raman spectroscopy of graphene and bilayer under biaxial strain: Bubbles and balloons,” *Nano Lett.*, vol. 12, no. 2, pp. 617–621, Feb. 2012, doi: 10.1021/nl203359n.

[96] S. T. Gill, J. H. Hinnefeld, S. Zhu, W. J. Swanson, T. Li, and N. Mason, “Mechanical Control of Graphene on Engineered Pyramidal Strain Arrays,” *ACS Nano*, vol. 9, no. 6, pp. 5799–5806, Jun. 2015, doi: 10.1021/acsnano.5b00335.

[97] N. Levy *et al.*, “Strain-Induced Pseudo–Magnetic Fields Greater Than 300 Tesla in Graphene Nanobubbles (supporting online material),” *Science (80-.).*, vol. 329, no. 584, p. 544, 2010, doi: 10.1126/science.1191700.

[98] F. Guinea, M. I. Katsnelson, and A. K. Geim, “Energy gaps, topological insulator state and zero-field quantum Hall effect in graphene by strain engineering,” *Nat. Phys.*, vol. 6, no. 1, pp. 30–33, 2009, doi: 10.1038/nphys1420.

[99] C. Si, Z. Liu, W. Duan, and F. Liu, “First-principles calculations on the effect of doping and biaxial tensile strain on electron-phonon coupling in graphene,” *Phys. Rev. Lett.*, vol. 111, no. 19, p. 196802, Nov. 2013, doi: 10.1103/PhysRevLett.111.196802.

[100] V. Abdelsayed, S. Moussa, H. M. Hassan, H. S. Aluri, M. M. Collinson, and M. S. El-Shall, “Photothermal deoxygenation of graphite oxide with laser excitation in solution and graphene-aided increase in water temperature,” *J. Phys. Chem. Lett.*, vol. 1, no. 19, pp. 2804–2809, Oct. 2010, doi: 10.1021/jz1011143.

[101] G. Kalita, L. Qi, Y. Namba, K. Wakita, and M. Umeno, “Femtosecond laser induced micropatterning of graphene film,” *Mater. Lett.*, vol. 65, no. 11, pp. 1569–1572, 2011, doi: 10.1016/j.matlet.2011.02.057.

[102] F. Herziger, R. Mirzayev, E. Poliani, and J. Maultzsch, “In-situ Raman study of laser-induced graphene oxidation,” *Phys. Status Solidi Basic Res.*, vol. 252, no. 11, pp. 2451–2455, Nov. 2015, doi: 10.1002/pssb.201552411.

[103] B. Krauss, T. Lohmann, D. H. Chae, M. Haluska, K. Von Klitzing, and J. H. Smet, “Laser-induced disassembly of a graphene single crystal into a nanocrystalline network,” *Phys. Rev. B - Condens. Matter Mater. Phys.*, vol. 79, no. 16, p. 165428, Apr. 2009, doi: 10.1103/PhysRevB.79.165428.

[104] V. Kiisk, T. Kahro, J. Kozlova, L. Matisen, and H. Alles, “Nanosecond laser treatment of graphene,” *Appl. Surf. Sci.*, vol. 276, pp. 133–137, 2013, doi: 10.1016/j.apsusc.2013.03.047.

[105] C. Pittenger, B.; Erina, N.; Su, “Bruker Application Note No. 128.” 2011.

[106] B. Pittenger, N. Erina, and C. Su, *Mechanical Property Mapping at the Nanoscale Using PeakForce QNM Scanning Probe Technique BT - Nanomechanical Analysis of High Performance Materials*. 2014.

[107] A. Johansson *et al.*, “Optical Forging of Graphene into Three-Dimensional Shapes,” *Nano Lett.*, vol. 17, no. 10, pp. 6469–6474, Oct. 2017, doi: 10.1021/acs.nanolett.7b03530.

[108] J. Aumanen, A. Johansson, J. Koivistoinen, P. Myllyperkiö, and M. Pettersson, “Patterning and tuning of electrical and optical properties of graphene by laser induced two-photon oxidation,” *Nanoscale*, vol. 7, no. 7, pp. 2851–2855, 2015, doi: 10.1039/c4nr05207b.

[109] A. C. Ferrari *et al.*, “Raman spectrum of graphene and graphene layers.,” *Phys. Rev. Lett.*, vol. 97, no. 18, p. 187401, Oct. 2006, doi: 10.1103/PhysRevLett.97.187401.

[110] J. U. Lee, D. Yoon, and H. Cheong, “Estimation of young’s modulus of graphene by Raman spectroscopy,” *Nano Lett.*, vol. 12, no. 9, pp. 4444–4448, Sep. 2012, doi: 10.1021/nl301073q.

[111] J. E. Lee, G. Ahn, J. Shim, Y. S. Lee, and S. Ryu, “Optical separation of mechanical strain from charge doping in graphene.,” *Nat. Commun.*, vol. 3, p. 1024, 2012, doi: 10.1038/ncomms2022.

[112] R. Meier and B. Kip, “Determination of the Local Temperature at a Sample during Raman Experiments Using Stokes and Anti-Stokes Raman Bands,” *Appl. Spectrosc.*, vol. 44, no. 4, pp. 707–711, 2000.

[113] N. A. Marigheto, E. K. Kemsley, J. Potter, P. S. Belton, and R. H. Wilson, “Effects of sample heating in FT-Raman spectra of biological materials,” *Spectrochim. Acta - Part A Mol. Spectrosc.*, vol. 52, no. 12 PART A, pp. 1571–1579, 1996, doi: 10.1016/0584-8539(96)01732-1.

[114] M. Lanzi, F. P. Di-Nicola, M. Livi, L. Paganin, F. Cappelli, and F. Pierini, “Synthesis and characterization of conjugated polymers for the obtainment of conductive patterns through laser tracing,” *J. Mater. Sci.*, vol. 48, no. 11, pp.

3877–3893, Jun. 2013, doi: 10.1007/s10853-013-7204-1.

[115] J. H. Lee *et al.*, "Nanometer thick elastic graphene engine," *Nano Lett.*, vol. 14, no. 5, pp. 2677–2680, May 2014, doi: 10.1021/nl500568d.

[116] B. Zhao *et al.*, "Mechanical mapping of nanobubbles by PeakForce atomic force microscopy," *Soft Matter*, vol. 9, no. 37, pp. 8837–8843, 2013, doi: 10.1039/c3sm50942g.

[117] D. Singh, J. Y. Murthy, and T. S. Fisher, "Mechanism of thermal conductivity reduction in few-layer graphene," *J. Appl. Phys.*, vol. 110, no. 4, p. 44317, 2011, doi: 10.1063/1.3622300.

[118] Z. Deng, N. N. Klimov, S. D. Solares, T. Li, H. Xu, and R. J. Cannara, "Nanoscale interfacial friction and adhesion on supported versus suspended monolayer and multilayer graphene," *Langmuir*, vol. 29, no. 1, pp. 235–243, Jan. 2013, doi: 10.1021/la304079a.

[119] S. Ryu *et al.*, "Atmospheric oxygen binding and hole doping in deformed graphene on a SiO2 substrate," *Nano Lett.*, vol. 10, no. 12, pp. 4944–4951, Dec. 2010, doi: 10.1021/nl1029607.

[120] O. Kazakova, V. Panchal, and T. Burnett, "Epitaxial Graphene and Graphene–Based Devices Studied by Electrical Scanning Probe Microscopy," *Crystals*, vol. 3, no. 1, pp. 191–233, 2013, doi: 10.3390/cryst3010191.

[121] C. Melios *et al.*, "Effects of humidity on the electronic properties of graphene prepared by chemical vapour deposition," *Carbon N. Y.*, vol. 103, pp. 273–280, 2016, doi: 10.1016/j.carbon.2016.03.018.

[122] M. M. Salary, S. Inampudi, K. Zhang, E. B. Tadmor, and H. Mosallaei, "Mechanical actuation of graphene sheets via optically induced forces," *Phys. Rev. B*, vol. 94, no. 23, p. 235403, Dec. 2016, doi: 10.1103/PhysRevB.94.235403.

[123] Y. Zhang, H. Son, J. Zhang, J. Kong, and Z. Liu, "Laser-heating effect on Raman spectra of individual suspended single-walled carbon nanotubes," *J. Phys. Chem. C*, vol. 111, no. 5, pp. 1988–1992, Feb. 2007, doi: 10.1021/jp066016e.

[124] M. Lazzeri and F. Mauri, "Nonadiabatic Kohn anomaly in a doped graphene monolayer," *Phys. Rev. Lett.*, vol. 97, no. 26, p. 266407, Dec. 2006, doi: 10.1103/PhysRevLett.97.266407.

[125] S. Piscanec, M. Lazzeri, F. Mauri, A. C. Ferrari, and J. Robertson, "Kohn Anomalies and Electron-Phonon Interaction in Graphite," *Phys. Rev. Lett.*, vol. 93, no. 18, p. 185503, Oct. 2004, doi: 10.1103/PhysRevLett.93.185503.

[126] R. Beams, L. Gustavo Cançado, and L. Novotny, "Raman characterization of defects and dopants in graphene," *Journal of Physics Condensed Matter*, vol. 27, no. 8. p. 083002, 04-Mar-2015, doi: 10.1088/0953-8984/27/8/083002.

[127] L. G. Cançado *et al.*, "Quantifying defects in graphene via Raman spectroscopy at different excitation energies," *Nano Lett.*, vol. 11, no. 8, pp. 3190–3196, Aug. 2011, doi: 10.1021/nl201432g.

[128] L. Martins, M. Matos, … A. P.-N., and U. 2017, "Raman evidence for pressure-

induced formation of diamondene," *nature.com*.

[129] I. Calizo, I. Bejenari, M. Rahman, G. Liu, and A. A. Balandin, "Ultraviolet Raman microscopy of single and multilayer graphene," *J. Appl. Phys.*, vol. 106, no. 4, p. 043509, Aug. 2009, doi: 10.1063/1.3197065.

[130] M. Kalbáč *et al.*, "Evaluating arbitrary strain configurations and doping in graphene with Raman spectroscopy," *2D Mater.*, vol. 5, no. 1, p. 015016, 2017, doi: 10.1088/2053-1583/aa90b3.

[131] J. S. Bunch *et al.*, "Impermeable atomic membranes from graphene sheets," *Nano Lett.*, vol. 8, no. 8, pp. 2458–2462, Aug. 2008, doi: 10.1021/nl801457b.

[132] S. P. Koenig, N. G. Boddeti, M. L. Dunn, and J. S. Bunch, "Ultrastrong adhesion of graphene membranes - Supplement Material," *Nat. Nanotechnol.*, vol. 6, no. 9, pp. 543–546, 2011, doi: 10.1038/nnano.2011.123.

[133] D. M. A. Mackenzie *et al.*, "Fabrication of CVD graphene-based devices via laser ablation for wafer-scale characterization," *2D Mater.*, vol. 2, no. 4, p. 045003, Oct. 2015, doi: 10.1088/2053-1583/2/4/045003.

[134] G. Xing, H. Guo, X. Zhang, T. C. Sum, and C. H. A. Huan, "The Physics of ultrafast saturable absorption in graphene," *Opt. Express*, vol. 18, no. 5, p. 4564, 2010, doi: 10.1364/oe.18.004564.

[135] M. Currie *et al.*, "Quantifying pulsed laser induced damage to graphene," *Appl. Phys. Lett.*, vol. 99, no. 21, p. 211909, Nov. 2011, doi: 10.1063/1.3663875.

[136] M. M. Lucchese *et al.*, "Quantifying ion-induced defects and Raman relaxation length in graphene," *Carbon N. Y.*, vol. 48, no. 5, pp. 1592–1597, 2010, doi: 10.1016/j.carbon.2009.12.057.

[137] G. Eda and M. Chhowalla, "Chemically derived graphene oxide: Towards large-area thin-film electronics and optoelectronics," *Advanced Materials*, vol. 22, no. 22. pp. 2392–2415, 02-Jun-2010, doi: 10.1002/adma.200903689.

[138] M. Oliverio, S. Perotto, G. C. Messina, L. Lovato, and F. De Angelis, "Chemical Functionalization of Plasmonic Surface Biosensors: A Tutorial Review on Issues, Strategies, and Costs," *ACS Appl. Mater. Interfaces*, vol. 9, no. 35, pp. 29394–29411, Sep. 2017, doi: 10.1021/acsami.7b01583.

[139] J. Lu *et al.*, "Bandgap Engineering of Phosphorene by Laser Oxidation toward Functional 2D Materials," *ACS Nano*, vol. 9, no. 10, pp. 10411–10421, Oct. 2015, doi: 10.1021/acsnano.5b04623.

[140] Y. Sun, "Silver nanowires - Unique templates for functional nanostructures," *Nanoscale*, vol. 2, no. 9, pp. 1626–1642, 2010, doi: 10.1039/c0nr00258e.

[141] D. S. Hecht, L. Hu, and G. Irvin, "Emerging transparent electrodes based on thin films of carbon nanotubes, graphene, and metallic nanostructures," *Advanced Materials*, vol. 23, no. 13. pp. 1482–1513, 05-Apr-2011, doi: 10.1002/adma.201003188.

[142] S. De *et al.*, "Silver Nanowire Networks as Flexible, Transparent, Conducting Films: Extremely High DC to Optical Conductivity Ratios," *ACS Nano*, vol. 3, no. 7, pp. 1767–1774, Jul. 2009, doi: 10.1021/nn900348c.

[143] L. Hu, H. Kim, J. Lee, and P. Peumans, “Scalable coating and properties of transparent, flexible, silver nanowire electrodes,” *ACS Publ.*, vol. 4, no. 5, pp. 2955–2963, 2010.

[144] S. Ishibashi, Y. Higuchi, Y. Ota, and K. Nakamura, “Low resistivity indium–tin oxide transparent conductive films. II. Effect of sputtering voltage on electrical property of films,” *J. Vac. Sci. Technol. A Vacuum, Surfaces, Film.*, vol. 8, no. 3, pp. 1403–1406, May 1990, doi: 10.1116/1.576890.

[145] C. H. Liu and X. Yu, “Silver nanowire-based transparent, flexible, and conductive thin film,” *Nanoscale Res. Lett.*, vol. 6, no. 1, p. 75, Dec. 2011, doi: 10.1186/1556-276X-6-75.

[146] Y. Leterrier *et al.*, “Mechanical integrity of transparent conductive oxide films for flexible polymer-based displays,” *Thin Solid Films*, vol. 460, no. 1–2, pp. 156–166, Jul. 2004, doi: 10.1016/j.tsf.2004.01.052.

[147] S. Sorel, P. E. Lyons, S. De, J. C. Dickerson, and J. N. Coleman, “The dependence of the optoelectrical properties of silver nanowire networks on nanowire length and diameter,” *Nanotechnology*, vol. 23, no. 18, p. 185201, May 2012, doi: 10.1088/0957-4484/23/18/185201.

[148] A. M. Alfantazi and R. R. Moskalyk, “Processing of indium: A review,” *Minerals Engineering*, vol. 16, no. 8. Pergamon, pp. 687–694, 01-Aug-2003, doi: 10.1016/S0892-6875(03)00168-7.

[149] A. R. Madaria, A. Kumar, and C. Zhou, “Large scale , highly conductive and patterned transparent films of silver nanowires on arbitrary substrates and,” *Nature*, vol. 245201, 2011, doi: 10.1088/0957-4484/22/24/245201.

[150] B. G. Lewis and D. C. Paine, “Applications and processing of transparent conducting oxides,” *MRS Bull.*, no. August, pp. 22–27, 2000.

[151] A. Herzog Cardoso, C. A. P. Leite, M. E. D. Zaniquelli, and F. Galembeck, “Easy polymer latex self-assembly and colloidal crystal formation: The case of poly[styrene-co-(2-hydroxyethyl methacrylate)],” *Colloids Surfaces A Physicochem. Eng. Asp.*, vol. 144, no. 1–3, pp. 207–217, Dec. 1998, doi: 10.1016/S0927-7757(98)00645-1.

[152] G. Kavitha, S. R. C. Vivek, A. Govindaraj, and C. Narayana, “A low-cost Raman spectrometer design used to study Raman scattering from a single-walled carbon nanotube,” *J. Chem. Sci.*, vol. 115, no. 5–6, pp. 689–694, Oct. 2003, doi: 10.1007/bf02708258.

[153] T. Fang, A. Konar, H. Xing, and D. Jena, “Carrier statistics and quantum capacitance of graphene sheets and ribbons,” *Appl. Phys. Lett.*, vol. 91, no. 9, p. 092109, Aug. 2007, doi: 10.1063/1.2776887.

[154] X. Wang, L. Zhi, and K. Müllen, “Transparent, conductive graphene electrodes for dye-sensitized solar cells.,” *Nano Lett.*, vol. 8, no. 1, pp. 323–7, Jan. 2008, doi: 10.1021/nl072838r.

[155] M.-S. Lee *et al.*, “High-Performance, Transparent, and Stretchable Electrodes Using Graphene–Metal Nanowire Hybrid Structures,” *Nano Lett.*, vol. 13, no. 6, pp. 2814–2821, Jun. 2013, doi: 10.1021/nl401070p.

[156] A. Fahimi *et al.*, “Density controlled conductivity of pristine graphene films,” *Carbon N. Y.*, vol. 64, no. Cvd, pp. 435–443, 2013, doi: 10.1016/j.carbon.2013.07.096.

[157] S. Xie, Z. Ouyang, B. Jia, and M. Gu, “Large-size, high-uniformity, random silver nanowire networks as transparent electrodes for crystalline silicon wafer solar cells,” *Opt. Express*, vol. 21, no. S3, p. A355, 2013, doi: 10.1364/OE.21.00A355.

[158] N. Azmoodeh, N. Chivu, R. B. Sadeghian, and M. Kahrizi, “A silver nanowire based gas ionization sensor eurocon2009,” in *IEEE EUROCON 2009, EUROCON 2009*, 2009, pp. 1231–1235, doi: 10.1109/EURCON.2009.5167793.

[159] E. C. Garnett *et al.*, “Self-limited plasmonic welding of silver nanowire junctions,” *Nat. Mater.*, vol. 11, no. 3, pp. 241–249, Mar. 2012, doi: 10.1038/nmat3238.

[160] S. Coskun, E. Selen Ates, and H. Emrah Unalan, “Optimization of silver nanowire networks for polymer light emitting diode electrodes,” *Nanotechnology*, vol. 24, no. 12, 2013, doi: 10.1088/0957-4484/24/12/125202.

[161] L. Yang, T. Zhang, H. Zhou, S. C. Price, B. J. Wiley, and W. You, “Solution-Processed Flexible Polymer Solar Cells with Silver Nanowire Electrodes,” *ACS Appl. Mater. Interfaces*, vol. 3, no. 10, pp. 4075–4084, Oct. 2011, doi: 10.1021/am2009585.

[162] J. Van De Groep, P. Spinelli, and A. Polman, “Transparent conducting silver nanowire networks,” *Nano Lett.*, vol. 12, no. 6, pp. 3138–3144, 2012, doi: 10.1021/nl301045a.

[163] Tao, F. Kim, C. Hess, and J. Goldberger, “Langmuir− Blodgett silver nanowire monolayers for molecular sensing using surface-enhanced Raman spectroscopy,” *ACS Publ.*, vol. 3, no. 9, pp. 1229–1233, 2003.

[164] P. Peumans, J. Y. Lee, S. T. Connor, and Y. Cui, “Solution-processed metal nanowire mesh transparent electrodes,” *Nano Lett.*, vol. 8, no. 2, pp. 689–692, 2008.

[165] V. Scardaci, R. Coull, and J. N. Coleman, “Spray deposition of Silver Nanowire transparent conductive networks,” in *Proceedings of the IEEE Conference on Nanotechnology*, 2012, doi: 10.1109/NANO.2012.6321936.

[166] X. Zhang, W. N. M. Wong, and M. M. F. Yuen, “Conductive, transparent, flexible electrode from silver nanowire thin film with double layer structure,” in *Proceedings of the IEEE Conference on Nanotechnology*, 2012, doi: 10.1109/NANO.2012.6322001.

[167] T. Tokuno, M. Nogi, J. Jiu, and K. Suganuma, “Hybrid transparent electrodes of silver nanowires and carbon nanotubes: A low-temperature solution process,” *Nanoscale Res. Lett.*, vol. 7, no. 1, p. 281, Dec. 2012, doi: 10.1186/1556-276X-7-281.

[168] C. H. Chung, T. Bin Song, B. Bob, R. Zhu, and Y. Yang, “Solution-processed flexible transparent conductors composed of silver nanowire networks embedded in indium tin oxide nanoparticle matrices,” *Nano Res.*, vol. 5, no. 11, pp. 805–

814, 2012, doi: 10.1007/s12274-012-0264-8.

[169] Y. Ahn, Y. Jeong, and Y. Lee, “Improved Thermal Oxidation Stability of Solution-Processable Silver Nanowire Transparent Electrode by Reduced Graphene Oxide,” *ACS Appl. Mater. Interfaces*, vol. 4, no. 12, pp. 6410–6414, Dec. 2012, doi: 10.1021/am301913w.

[170] I. Jurewicz *et al.*, “Insulator-conductor type transitions in graphene-modified silver nanowire networks: A route to inexpensive transparent conductors,” *Adv. Funct. Mater.*, vol. 24, no. 48, pp. 7580–7587, 2014, doi: 10.1002/adfm.201402547.

[171] J. Tesch *et al.*, “Structural and electronic properties of graphene nanoflakes on Au(111) and Ag(111),” *Sci. Rep.*, vol. 6, no. 1, pp. 1–9, Mar. 2016, doi: 10.1038/srep23439.

[172] D. C. Choo and T. W. Kim, “Degradation mechanisms of silver nanowire electrodes under ultraviolet irradiation and heat treatment,” *Sci. Rep.*, vol. 7, no. 1, p. 1696, Dec. 2017, doi: 10.1038/s41598-017-01843-9.

[173] S. Coskun, B. Aksoy, and H. E. Unalan, “Polyol Synthesis of Silver Nanowires: An Extensive Parametric Study,” *Cryst. Growth Des.*, vol. 11, no. 11, pp. 4963–4969, Nov. 2011, doi: 10.1021/cg200874g.

[174] J. N. Coleman, “Liquid exfoliation of defect-free graphene,” *Acc. Chem. Res.*, vol. 46, no. 1, pp. 14–22, 2013, doi: 10.1021/ar300009f.

[175] D. C. Marcano *et al.*, “Improved synthesis of graphene oxide,” *ACS Nano*, vol. 4, no. 8, pp. 4806–4814, 2010, doi: 10.1021/nn1006368.

[176] Z. S. Wu *et al.*, “Synthesis of graphene sheets with high electrical conductivity and good thermal stability by hydrogen arc discharge exfoliation,” *ACS Nano*, vol. 3, no. 2, pp. 411–417, 2009, doi: 10.1021/nn900020u.

[177] M. J. McAllister *et al.*, “Single sheet functionalized graphene by oxidation and thermal expansion of graphite,” *Chem. Mater.*, vol. 19, no. 18, pp. 4396–4404, 2007, doi: 10.1021/cm0630800.

[178] S. Stankovich *et al.*, “Synthesis of graphene-based nanosheets via chemical reduction of exfoliated graphite oxide,” *Carbon N. Y.*, vol. 45, no. 7, pp. 1558–1565, 2007, doi: 10.1016/j.carbon.2007.02.034.

[179] H. J. Shin *et al.*, “Efficient reduction of graphite oxide by sodium borohydride and its effect on electrical conductance,” *Adv. Funct. Mater.*, vol. 19, no. 12, pp. 1987–1992, 2009, doi: 10.1002/adfm.200900167.

[180] W. Gao, L. B. Alemany, L. Ci, and P. M. Ajayan, “New insights into the structure and reduction of graphite oxide,” *Nat. Chem.*, vol. 1, no. 5, pp. 403–408, 2009, doi: 10.1038/nchem.281.

[181] D. Voiry *et al.*, “High-quality graphene via microwave reduction of solution-exfoliated graphene oxide,” *Science (80-.).*, vol. 353, no. 6306, pp. 1413–1416, 2016, doi: 10.1126/science.aah3398.

[182] Y. Qiu, F. Collin, R. H. Hurt, and I. Külaots, “Thermochemistry and kinetics of graphite oxide exothermic decomposition for safety in large-scale storage and

processing," *Carbon N. Y.*, vol. 96, pp. 20–28, 2016, doi: 10.1016/j.carbon.2015.09.040.

[183] H. A. Becerril, J. Mao, Z. Liu, R. M. Stoltenberg, Z. Bao, and Y. Chen, "Evaluation of solution-processed reduced graphene oxide films as transparent conductors," *ACS Nano*, vol. 2, no. 3, pp. 463–470, 2008, doi: 10.1021/nn700375n.

[184] L. Liu, J. Zhang, and F. Liu, "Mechanical properties of graphene oxides," *Nanoscale*, vol. 4, pp. 5910–5916, 2012, doi: 10.1039/c2nr31164j.

[185] J. L. Keddie, "Reports : A Review Journal Film formation of latex," *Mater. Sci. Eng.*, vol. 21, no. 97, pp. 101–170, 1997.

[186] Y. Liu *et al.*, "Explanations for water whitening in secondary dispersion and emulsion polymer films," *J. Polym. Sci. Part B Polym. Phys.*, vol. 54, no. 16, pp. 1658–1674, 2016, doi: 10.1002/polb.24070.

[187] A. Boudenne, L. Ibos, M. Fois, J. C. Majesté, and E. Géhin, "Electrical and thermal behavior of polypropylene filled with copper particles," *Compos. Part A Appl. Sci. Manuf.*, vol. 36, no. 11, pp. 1545–1554, 2005, doi: 10.1016/j.compositesa.2005.02.005.

[188] Y. P. Mamunya, V. V. Davydenko, P. Pissis, and E. V. Lebedev, "Electrical and thermal conductivity of polymers filled with metal powders," *Eur. Polym. J.*, vol. 38, no. 9, pp. 1887–1897, 2002, doi: 10.1016/S0014-3057(02)00064-2.

[189] E. K. Sichel and J. I. Gittleman, "Electrical Properties of Carbon - Polymer Composites," *J. Electron. Mater.*, vol. 11, no. 4, pp. 699–747, 1982, doi: 10.1007/BF02672392.

[190] M. BORKOVEC, W. DE PARIS, and R. PEIKERT, "THE FRACTAL DIMENSION OF THE APOLLONIAN SPHERE PACKING," *Fractals*, vol. 02, no. 04, pp. 521–526, Dec. 1994, doi: 10.1142/S0218348X94000739.

[191] M. Antonietti, J. Hartmann, M. Neese, and U. Seifert, "Highly ordered size-dispersive packings of polydisperse microgel spheres," *Langmuir*, vol. 16, no. 20, pp. 7634–7639, 2000, doi: 10.1021/la000508f.

[192] E. S. McLamore *et al.*, "Bio-inspired patterned networks (BIPS) for development of wearable/disposable biosensors," 2016, vol. 9863, p. 986309, doi: 10.1117/12.2223345.

[193] H. B. Bohidar, "Kinetics of self-organization of polyampholyte nanopartieles in solutions," in *Bulletin of Materials Science*, 2008, vol. 31, no. 3, pp. 391–395, doi: 10.1007/s12034-008-0061-x.

[194] J. C. Grunlan, W. W. Gerberich, and L. F. Francis, "Lowering the percolation threshold of conductive composites using particulate polymer microstructure," *J. Appl. Polym. Sci.*, vol. 80, no. 4, pp. 692–705, 2001, doi: 10.1002/1097-4628(20010425)80:4<692::AID-APP1146>3.0.CO;2-W.

[195] I. Jurewicz *et al.*, "Colloid-assisted self-assembly of robust, three-dimensional networks of carbon nanotubes over large areasa," *Macromol. Rapid Commun.*, vol. 31, no. 7, pp. 609–615, 2010, doi: 10.1002/marc.200900799.

[196] A. F. Keddie, Joseph, Routh, *Fundamentals of Latex Film Formation: Processes and Properties*. Dordrecht: Springer Netherlands, 2010.

[197] F. Li, M. Xue, X. Ma, M. Zhang, and T. Cao, “Facile patterning of reduced graphene oxide film into microelectrode array for highly sensitive sensing,” *Anal. Chem.*, vol. 83, no. 16, pp. 6426–6430, 2011, doi: 10.1021/ac200939g.

[198] L. Sygellou, G. Paterakis, C. Galiotis, and D. Tasis, “Work Function Tuning of Reduced Graphene Oxide Thin Films,” *J. Phys. Chem. C*, vol. 120, no. 1, pp. 281–290, 2016, doi: 10.1021/acs.jpcc.5b09234.

[199] W. Bauhofer, J. Z. Kovacs, T. Swan, T. Swan, and T. Swan, “A review and analysis of electrical percolation in carbon nanotube polymer composites,” *Compos. Sci. Technol.*, vol. 69, no. 10, pp. 1486–1498, 2008, doi: 10.1016/j.compscitech.2008.06.018.

[200] D. Stauffer and A. Aharony, “Introduction to percolation theory,” 2018.

[201] J. F. Douglas and F. Thorpe, “Geometrical percolation threshold ofoverlapping ellipsoids,” *Phys. Rev. E*, vol. 52, no. 1, pp. 819–828, 1995.

[202] Dimitris Achlioptas and Joel Spencer, “Explosive Percolation in Random Networks,” *Science (80-.).*, vol. 323, no. 5920, pp. 1453–1456, 2009, doi: 10.1126/science.1167782.

[203] R. A. Da Costa, S. N. Dorogovtsev, A. V. Goltsev, and J. F. F. Mendes, “Explosive percolation transition is actually continuous,” *Phys. Rev. Lett.*, vol. 105, no. 25, 2010, doi: 10.1103/PhysRevLett.105.255701.

[204] B. Mutel, P. Goudmand, L. Gengembre, and J. Grimblot, “Energy Consumption and Kinetic Evolution of Nitrogen Fixation on Polyethylene Terephthalate by Remote Nitrogen Plasma : XPS Study,” *Surf. Interface Anal.*, vol. 20, pp. 283–289, 1993.

[205] H. M. D. and M. J. F.Bodino, G. Baud, M. Benmalek, J.P. Besse, “Alumina coating on polyethylene terephthalate,” *Thin Solid Films*, vol. 241, pp. 21–24, 1994.

[206] M. J. Cadena *et al.*, “Sub-surface imaging of carbon nanotube-polymer composites using dynamic AFM methods,” *Nanotechnology*, vol. 24, no. 13, 2013, doi: 10.1088/0957-4484/24/13/135706.